

A Finite Element Model for the Simulation of Micro-Cutting

Dem Fachbereich Maschinenbau und Verfahrenstechnik
der Technischen Universität Kaiserslautern
zur Verleihung des akademischen Grades
Doktor-Ingenieur (Dr.-Ing.)
genehmigte Dissertation

von
Dipl.-Ing. Robert Bischof
aus Saarbrücken

Hauptreferent: Prof. Dr.-Ing. Ralf Müller
Korreferent: Prof. Dr.-Ing. Wolfgang Dornisch
Vorsitzende: Prof. Dr.-Ing. Kristin de Payrebrune
Dekan: Prof. Dr.-Ing. Tilmann Beck

Tag der Einreichung: 28.10.2020
Tag der mündlichen Prüfung: 22.01.2021

Kaiserslautern, 2021

D 386

Herausgeber

Lehrstuhl für Technische Mechanik
Technische Universität Kaiserslautern
Gottlieb-Daimler-Straße
Postfach 3049
67653 Kaiserslautern

© Robert Bischof

Ich danke der “Prof. Dr. Hans Georg und Liselotte Hahn Stiftung” für die finanzielle Unterstützung bei der Drucklegung.

Druck

Technische Universität Kaiserslautern
Hauptabteilung 5 / Bau-Technik-Energie
Abteilung 5.6 Foto-Repro-Druck

Alle Rechte vorbehalten, auch das des auszugsweisen Nachdrucks, der auszugsweisen oder vollständigen Wiedergabe (Fotographie, Mikroskopie), der Speicherung in Datenverarbeitungsanlagen und das der Übersetzung.

ISBN 978-3-942695-21-3

Vorwort

Als ich im Jahr 2015 meine Tätigkeit als wissenschaftlicher Mitarbeiter an der Technischen Universität Kaiserslautern begann, war es noch ein weiter Weg bis zur fertigen Dissertation. Als Projektarbeiter im Sonderforschungsbereich 926 fand ich zum Thema der vorliegenden Arbeit und nun, knapp 6 Jahre später, liegt die gedruckte Dissertation vor.

Dies wäre ohne die viele Hilfe und Unterstützung, die ich von allen Seiten erfahren habe, nicht möglich gewesen. Ich danke meinem Doktorvater Prof. Dr.-Ing. Ralf Müller für die Unterstützung während meiner wissenschaftlichen Tätigkeit am Lehrstuhl für Technische Mechanik, sowie während des anschließenden Promotionsverfahrens. Außerdem danke ich Prof. Dr.-Ing. Wolfgang Dornisch für die Übernahme des Korreferats und Prof. Dr.-Ing. Kristin de Payrebrune für die Übernahme des Vorsitzes. Auch bedanken möchte ich mich bei Dr.-Ing. Charlotte Kuhn, die mir als Projektleiterin immer mit fachlichem Rat zur Seite gestanden hat.

Die Zeit am Lehrstuhl war eine Zeit voller positiver Erfahrungen, sowohl in fachlicher als auch in persönlicher Hinsicht. So denke ich gerne an die vergangene Zeit zurück, für die ich mich recht herzlich bei allen ehemaligen Kollegen bedanke. Insbesondere bei Prof. Dr.-Ing. Wolfgang Dornisch, der als ehemaliger Lehrstuhlkollege immer gerne am fachlichen Austausch teilgenommen hat und somit einen essentiellen Beitrag zur gesamten Arbeit geleistet hat. Bedanken möchte ich mich auch bei Paul Breuninger, Fabian Krull und Simon Schmidt für die gerne gefundene Abwechslung zum Forschungsalltag. Mein Dank gehört auch Prof. Dr.-Ing. Christian Linder für die Gastfreundschaft während meines Auslandsaufenthalts an der Stanford University.

Da sich die Anfertigung dieser Arbeit über meine Beschäftigungszeit an der TU hinauszog, gehörte auch ein Jobwechsel zu den Hürden, die ich während der Fertigstellung nehmen musste. Hier gilt mein ganz besonderer Dank Thomas Bauer und Christian Schmeißer, die mich während meiner neuen Tätigkeit mit allen Mitteln unterstützt haben um die Dissertation neben dem neuen Job fertigzustellen.

Schließlich danke ich meinen Eltern und meiner Schwester, die mich in meiner gesamten Berufsausbildung bedingungslos unterstützt und immer Verständniss gezeigt haben, sowie für die Unterstützung all meiner Freunde.

Mandelbachtal, im Februar 2021

Robert Bischof

Zusammenfassung

Titan gehört mit seinen vorteilhaften mechanischen und chemischen Eigenschaften zu den wichtigen Metallen, die für technische Anwendungen genutzt werden. Eine hohe Festigkeit bei, verglichen zu anderen Metallen, geringer Dichte und eine gute Korrosionsbeständigkeit sind nur zwei dieser Eigenschaften. In der Luftfahrtindustrie wird Titan wegen seiner hohen Kriechfestigkeit eingesetzt, die Biomedizin und die chemische Industrie verwenden Titan aufgrund der guten Korrosionsbeständigkeit. Eine Verbreitung des Werkstoffs in weitere Industriezweige wird jedoch aufgrund der hohen Kosten von Titan verhindert. Dies macht es um so wichtiger, die Herstellungs- und Verarbeitungskosten zu senken. Dazu ist ein fundiertes Wissen über die technischen Eigenschaften, wie z.B. das Deformationsverhalten, von Titan nötig. Die Bauteiloberfläche, ihre Zusammensetzung auf der Mikroskala und ihre Beschaffenheit rücken dabei immer mehr in den Fokus aktueller Forschung. Zur Untersuchung von Metallen werden neben experimentellen Versuchen auch numerische Simulationsmethoden verwendet. Molekulardynamische Simulationen werden eingesetzt um auf molekularer Ebene Wechselwirkungen zu untersuchen und sind für größere Längen- und Zeitskalen nicht geeignet, da die Rechenzeit für große Systeme stark ansteigt. Um komplexes Materialverhalten auf diesen Längen- und Zeitskalen zu simulieren ist die Finite Element Methode (FEM) geeignet.

Die vorliegende Arbeit beschäftigt sich mit der Simulation des Micro-Cutting-Verfahrens von commercially-pure (cp) Titan mit Hilfe der FEM. Da in diesem Zerspanprozess große Verzerrungen und große Deformationen auftreten wird als Grundlage zur Beschreibung dieser Verzerrungen und Deformationen eine Einführung in die nicht-lineare Kontinuumsmechanik gegeben. Dazu gehören die kinematischen Grundlagen, wie der Deformationsgradient und unterschiedliche Verzerrungsmaße, die Theorie der Spannung, die Bilanzsätze und die thermodynamischen Grundlagen. Da bei dem Micro-Cutting-Verfahren die kristalline Mikrostruktur einen wesentlichen Einfluss auf das Deformationsverhalten hat, wird in diesem Kapitel ein kristall-plastisches Materialmodell vorgestellt. Dieses Materialmodell beachtet sowohl die großen Deformationen und Verzerrungen als auch die hexagonale-dichtestgepackte (hcp) Kristallstruktur von cp-Titan. Für den elastischen Teil wird dabei ein neo-Hooke Materialmodell verwendet. Abgeschlossen wird das Kapitel durch die Erläuterung der schwachen Form der Gleichgewichtsbedingung, sowie die Linearisierung der schwachen Form. Beides bildet die Grundlage für die FEM.

Das darauffolgende Kapitel beinhaltet die Grundlagen der numerischen Diskretisierung. Dazu werden zunächst die Grundlagen der FEM und die F-Bar Erweiterung zur Vermeidung von volumetrischem Locking für die Simulation inkompressibler Materialien vorgestellt. Das kristall-plastische Materialmodell enthält zeitabhängige, konstitutive Gleichungen. Das benötigte Zeitintegrationsverfahren und der Return-Mapping Lösungsalgorithmus zur Behandlung des elastisch-plastischen Materialmodells wird im weiteren Verlauf des Kapitels vorgestellt. Dabei handelt es sich um einen Update-Algorithmus, der aus zwei Schritten besteht: Dem elastischen Versuchsschritt und dem plastischen Korrektorschritt. Es wird herausgestellt, dass die Auswahl der aktiven Gleitsysteme einen kritischen Bestandteil dieses Algorithmus darstellt.

Zur Implementierung sind noch weitere Details von Bedeutung. Um zu zeigen, dass das Auswahlverfahren der aktiven Gleitsysteme ein essentieller Teil ist werden zwei unterschiedliche Algorithmen vorgestellt und miteinander verglichen. Der erste Algorithmus basiert auf den Karush-Kuhn-Tucker Bedingungen und ist in der Standardliteratur weit verbreitet. Jedoch hat dieser Algorithmus bekannte Schwächen. Aus diesem Grund wird ein weiterer Auswahlalgorithmus vorgestellt, der auf der Fischer-Burmeister-Funktion basiert. Des Weiteren werden die Eigenschaften der hcp-Kristallstruktur genannt. Zunächst werden die Gleitsysteme eingeführt, welche in zwei verschiedene Gruppen unterteilt werden. Darauffolgend werden drei verschiedene Verfestigungsmechanismen vorgestellt. Zur Modellierung der Materialauftrennung zwischen Span und Werkstück gibt es viele Ansätze, wovon in dieser Arbeit zwei miteinander verglichen werden. Grundlage ist, dass die entsprechenden Elemente im Trennbereich von Werkstück und Span anhand von entsprechenden Kriterien gelöscht werden und somit keinen weiteren Beitrag zur Gesamtsteifigkeit mehr leisten. Der erste Ansatz basiert dabei auf rein geometrischen Kriterien, während sich der zweite Ansatz auf Kriterien aus der Schädigungsmechanik stützt. Das nichtlineare Materialmodell stellt hohe Anforderungen an die Rechenleistung und die dreidimensionalen Simulationen resultieren in einer hohen Anzahl von Freiheitsgraden. Um die Rechenzeit zu reduzieren werden numerische Parallelisierungen verwendet. Zum einen wird der Algorithmus zur Assemblierung der Steifigkeitsmatrix mit OpenMP[®] parallelisiert und zum anderen wird zur Lösung des Gleichungssystems der parallele Intel[®] MKL PARDISO Löser verwendet.

Auf den theoretischen Teil der Arbeit folgt der simulative Teil. Zunächst wird an einem einfachen Beispiel mit zwei Gleitsystemen das Materialmodell validiert. Dazu wird ein Zugversuch an einer rechteckigen Probe mit einer symmetrischen und un-symmetrischen Ausrichtung der Gleitsysteme durchgeführt. Dazu werden drei unterschiedlich feine Rechnetze verwendet. Zum Vergleich der beiden Algorithmen zur Auswahl der aktiven Gleitsysteme werden alle Hauptgleitsysteme von cp-Titan zum Materialmodell hinzugefügt und ein Zugversuch an einer Lochscheibe durchgeführt. Ziel des Vergleichs ist die Auswahl eines geeigneten Algorithmus, um die Implementierung des Materialmodells so robust wie möglich zu gestalten. Im weiteren Verlauf wird die F-Bar Methode zur Vermeidung von volumetrischem Locking validiert und die drei verschiedenen Verfestigungsmechanismen werden mithilfe eines Zugversuchs an einer gekerbten Probe hinsichtlich Deformationsverhalten, Kraft-Weg-Diagramm und Rechenzeit miteinander verglichen. Der Vergleich der beiden Ansätze zur Netzauftrennung bildet den Abschluss der Validierungsbeispiele. Dazu wird eine vereinfachtes Beispiel der Micro-Cutting-Simulation verwendet.

Zum Abschluss der Arbeit wird das Micro-Cutting-Verfahren untersucht. Dieser Teil ist grundsätzlich in zwei Abschnitte unterteilt. Zunächst wird das Simulationssetup für das Verfahren vorgestellt und die allgemeinen Herausforderungen bei der Durchführung der Simulation aufgezeigt. Vor allem der initiale Kontakt zwischen Werkzeug und Werkstück wird betrachtet. Der Einfluss verschiedener Parameter auf den Micro-Cutting-Prozess wird anhand unterschiedlicher Beispiele untersucht. Zur Untersuchung des Einflusses unterschiedlicher Kristallorientierungen werden drei Simulationen durchgeführt, wobei das Werkstück jeweils aus vier Körnern mit unterschiedlicher Orientierung besteht, bei welchen die Kristallorientierungen zufällig gewählt werden. Der Einfluss der Schnitttiefe wird anhand einer Variation der Schnitttiefe von $2\ \mu\text{m}$ bis $10\ \mu\text{m}$ untersucht. Auch der Einfluss des Spanwinkels wird anhand einer Variation betrachtet. Dabei wird der Spanwinkel schrittweise von 0° bis 10° erhöht. Den Abschluss dieses Teils bildet die Variation des Verfestigungsmechanismus. Alle Simulationen in diesem Teil werden an einfachen Beispielen durchgeführt. Verglichen wird jeweils der Einfluss auf die Verformung und die plastische Deformation des Spans und der resultierenden Werkstücksoberfläche, sowie der Einfluss auf die Schnittkraft. Im zweiten Teil wird eine reale Mikrostruktur für das Werkstück verwendet. Zunächst wird gezeigt, wie ein Simulationsnetz auf Grundlage einer realen Probe erstellt wird und welche Schritte dazu nötig sind. Im Anschluss wird das Micro-Cutting-Verfahren an dieser Probe durchgeführt. Dabei wird auch betrachtet, welchen Einfluss die Elementgröße auf die plastische Deformation und die Schnittkraft hat. Außerdem wird der Einfluss der sogenannten $\langle c + a \rangle$ Gleitsysteme der hcp-Elementarzelle an der realen Probe ermittelt. Dazu werden drei Simulationen durchgeführt und miteinander verglichen. Die erste Simulation betrachtet nur die Hauptgleitsysteme, für die anderen beiden Simulationen werden die $\langle c + a \rangle$ Gleitsysteme miteinbezogen, wobei unterschiedliche Anfangsfließspannungen verwendet werden.

Kurzfassung

Die vorliegende Arbeit befasst sich mit der Simulation des Micro-Cutting-Verfahrens von Titan. Dazu wird ein geeignetes kristall-plastisches Materialmodell mitsamt geeigneter Implementierungen entwickelt, um die Simulation des Micro-Cutting-Verfahrens durchzuführen. Für das Materialmodell ergeben sich mehrere Herausforderungen. Zum einen muss die niedrigsymmetrische hexagonal-dichtestgepackte Kristallstruktur von Titan berücksichtigt werden, zum anderen treten bei der Zerspanung große Deformationen und Verzerrungen auf. Ein weiterer wichtiger Teil bildet der Algorithmus zur Auswahl der aktiven Gleitsysteme, welcher einen erheblichen Einfluss auf die Stabilität der gesamten Simulation hat. Um eine robuste Implementierung zu erhalten, werden verschiedene Aspekte, wie z.B. der Algorithmus zur Auswahl der aktiven Gleitsysteme, das Verfahren zur Netzauftrennung zwischen Span und Werkstück als auch das Verfestigungsverfahren untersucht und unterschiedliche Ansätze miteinander verglichen. Das entwickelte kristall-plastische Materialmodell und die gewählten Implementierungen werden zunächst an einfachen Beispielen validiert und untersucht. Die dargestellten Beispiele zum Micro-Cutting-Verfahren zeigen sowohl die Herausforderungen bei der Durchführung der Simulation, als auch den Einfluss von unterschiedlichen Prozessparametern auf das Verfahren. Schließlich wird der Einfluss einer realen Mikrostruktur auf die plastische Deformation und die Schnittkraft bei dem Prozess gezeigt.

Abstract

This work deals with the simulation of the micro-cutting process of titanium. For this purpose, a suitable crystal-plastic material model is developed and efficient implementations are investigated to simulate the micro-cutting process. Several challenges arise for the material model. On the one hand, the low symmetry hexagonal close-packed crystal structure of titanium has to be considered. On the other hand, large deformations and strains occur during the machining process. Another important part is the algorithm for the determination of the active slip systems, which has a significant influence on the stability of the simulation. In order to obtain a robust implementation, different aspects, such as the algorithm for the determination of the active slip systems, the method for mesh separation between chip and workpiece as well as the hardening process are investigated, and different approaches are compared. The developed crystal-plastic material model and the selected implementations are first validated and investigated using illustrative examples. The presented simulations of the micro-cutting process show the influence of different machining parameters on the process. Finally, the influence of a real microstructure on the plastic deformation and the cutting force during the process is shown.

Contents

1	Introduction	1
1.1	Motivation and Background	1
1.2	Objectives and Overview	3
2	Continuum Mechanics	5
2.1	Kinematics	5
2.1.1	Deformation Gradient	6
2.1.2	Isochoric/Volumetric Split of the Deformation Gradient	7
2.1.3	Strain Measures	8
2.2	Stress Measures	8
2.3	Balance Laws and Thermodynamics	10
2.3.1	Conservation of Mass	10
2.3.2	Balance of Linear Momentum and Angular Momentum	10
2.3.3	First Law of Thermodynamics	11
2.3.4	Second Law of Thermodynamics and Dissipation	12
2.4	Constitutive Model	14
2.4.1	Hyperelasticity	14
2.4.2	Crystal Plasticity for Finite Deformations	15
2.5	Weak Form and Linearization	20
2.5.1	Weak Form of Equilibrium	21
2.5.2	Linearization	21
3	Numerical Discretization	25
3.1	Fundamentals of the Finite Element Method	25
3.2	Extension for Incompressible Material	29
3.3	Integration Algorithm for Crystal Plastic Material	30
4	Implementation Details	35
4.1	Determination of Active Slip Systems	35
4.2	Properties of the Hexagonal Close-Packed Crystal Structure and Hardening Mechanisms	37
4.3	Material Separation	39
5	Validation Examples	41
5.1	Validation of the Material Model	41
5.2	Determination of Active Slip Systems	43
5.3	F-Bar Implementation	45
5.4	Hardening	47
5.5	Material Separation	48

6	Micro-Cutting Simulations	51
6.1	Simulation Setup for Micro-Cutting Simulations	51
6.2	Variation of the Crystal Orientation	56
6.3	Variation of the Cutting Depth	60
6.4	Variation of the Rake Angle	63
6.5	Variation of the Hardening Mechanism	67
6.6	Micro-Cutting Simulations of Real Material	69
6.6.1	Microstructure and Corresponding FEM Mesh	69
6.6.2	The Micro-Cutting Simulation of Real Material	73
6.6.3	Influence of All Slip Systems	76
7	Conclusion and Outlook	81

Chapter 1

Introduction

1.1 Motivation and Background

Titanium is an essential material for technical applications because of its excellent technical properties. The material shows a high strength with, compared to other materials, low density. Titanium also provides very good corrosion resistance. Due to these properties and the high creep resistance, titanium is preferred in the aeronautics industry. The biomedical and the chemical industry take advantage of the very good corrosion resistance. Further application of the material in other industries, such as the automotive industry, is hindered by its high costs. Lowering the costs in the production of titanium requires a complete understanding of the technical properties on the one hand, and the physical deformation behavior, on the other hand. The investigation of the material behavior and the interaction of the component surface is also increasingly the subject of current research, see Leyens and Peters (2006) or Lütjering and Williams (2013). The deformation behavior of micro samples of commercially pure titanium is the subject of the work of Godard (2015).

In general, metallic materials show a crystalline structure on the microscale. In contrast to the investigation on the macroscale, where metallic materials can be assumed as homogeneous materials, the crystalline structure has to be considered on the microscale. Figure 1.1 shows the typical microstructure of titanium with different grains. The sample is investigated with the Electron BackScatter Diffraction (EBSD) method.



FIGURE 1.1: EBSD picture of the micro structure of a cp-titanium sample (Bischof et al. (2018)).

The microstructure plays an important role in the description of the plastic deformation behavior. Investigations have shown that plastic deformation on the microstructure is a plastic sliding along slip planes of the specific crystals. These slip planes coincide with the close-packed layers in the atomic structure. Here titanium has a special role. While steel consists of a face-centered or body-centered structure, which shows a high symmetry orientation, titanium instead has a low symmetry hexagonal crystal structure. Experiments also show poorer malleability compared to cubic structured metals such as steel, copper, or aluminum.

For a better understanding of the material behavior and the manufacturing process on the microscale, often methods of physical material modeling and numerical simulations are used for the investigation in addition to the physical experiment. The modeling of those manufacturing processes, such as the cutting process, is highly challenging. The large deformations and large geometrical changes during the manufacturing process and the material separation between workpiece and chip are only two complicated phenomena within such simulations. Investigations of macroscopic cutting can be found in Shih (1996) and Özel and Zeren (2005). Micro-cutting processes are the topic of the work of Woon et al. (2008) and Li et al. (2017). Each of these works uses a two-dimensional model. The first three do not use a special mesh separation criterion method but use the arbitrary Lagrangian-Eulerian method with re-meshing for the chip forming. Li et al. (2017) use a separation criterion based on the fracture model of Johnson and Cook (1985). A different approach to simulate the cutting process is used in Sabel (2017), where mesh separation is an *ab initio* available process within the employed Particle Finite Element Method. Discussions about different approaches for the mesh separation can be found in the work of Komvopoulos and Erpenbeck (1991), Shet and Deng (2000), Mamalis et al. (2001) and Li et al. (2002). Furthermore, complex material models are needed, which describe the deformations, including plastic deformation of crystals on the microstructure. Thereby, the occurring large deformations need to be considered. For the simulation of engineering components and surfaces, the Finite Element Method (FEM) is well known and offers many advantages. Based on a continuum mechanics approach, the FEM allows the description of large elastic and plastic deformation at finite strains for sufficiently large time and length scales. Furthermore, the formulation of the node to surface contact, which is needed to model the contact between workpiece and tool, is already known and is used productively, compare to Wriggers (2006) or Laursen (2013).

The physical and continuum mechanical principles of the plasticity theory are explained by Lubliner (2013), both for the linearized theory and in the context of finite deformation. A very well-known comprehensive study of the plasticity subject is summarized in Simo and Hughes (1998). It covers both the continuum mechanics theory and numerical treatment with the Finite Element Method for the plasticity, viscoplasticity, and multisurface plasticity theory with mathematical accuracy, but only in the context of small strains. Thereby, the Return-Mapping algorithm is used for the integration of the elastoplastic equations. The crystal plasticity material model used in this work is mainly based on the slip theory of crystals. This theory is well established and part of many publications, see, for example, the fundamental work of Asaro (1983) and Havner (1992) or the publications of Asaro and Needleman (1985) and Miehe (1996a,b). Within the material model employed in this thesis, the elastic part is described by the neo-Hooke hyperelastic material, see Holzapfel (2000). The plastic part describes plastic slip in the slip systems of a crystal unit cell following the work of Miehe (1996a,b) and de Souza Neto et al. (2011). As described in Simo

and Hughes (1998), a crucial part of the whole material model is the determination of active slip systems. In general, a problem arises from the mathematical subfield of optimization and is solved in the standard literature using Lagrange multipliers. However, Simo and Hughes stated that this approach could lead to unphysical solutions or solutions that do not fulfill the underlying Karush-Kuhn-Tucker conditions. There are several solutions to circumvent these problems. One is to use the Fischer-Burmeister function, proposed by Fischer (1992).

1.2 Objectives and Overview

This thesis aims to investigate the crystal plasticity material model for large deformations and to adapt current approaches to a robust large deformation crystal plasticity material model, which is suitable for the simulation of the micro-cutting process. Since the investigation is focused on commercially pure titanium, the hexagonal close-packed crystal unit cell will be dealt with in particular. Besides, important factors influencing the micro-cutting process of commercially pure titanium will be investigated, and finally, the process will be transferred to real structures.

In chapter 2, at first, the basics of continuum mechanics are explained, including the kinematical fundamentals, the theory of stress, the balance laws, and the basics of thermodynamics. The second part of this chapter covers the description of the crystal plasticity material model. As described, the basis for this large strain crystal plasticity model is the multiplicative decomposition of the deformation gradient. The chapter concludes with the weak form of the equilibrium equation and the linearization of the fundamental equations, which is also the basis for the Finite Element Method used for the solution.

Chapter 3 provides details about the numerical discretization. After starting with the basics of the finite element method, some aspects are discussed to avoid overly stiff results due to so-called volumetric locking, which can occur in plastic material models. Finally, the time integration and the return mapping algorithm for solving the elastoplastic problem is discussed.

Additional aspects of implementation are introduced in chapter 4. First, two approaches for the determination of active slip systems are shown, which are an essential part of the overall solution algorithm. Furthermore, the details of the hexagonal close-packed crystal unit cell and the physical phenomenon of hardening are discussed. The chapter is concluded with two different methods to implement mesh separation.

In chapter 5, the implementations are validated, and the different implementation details are investigated. First, it is shown on a simplified model with two slip systems that the introduced crystal plasticity material model basically yields the expected results. In the second part of the chapter, the main slip systems of the hexagonal close-packed crystal unit cell are involved in the material model, and the two introduced methods for the determination of the active slip systems are compared, and their advantages and disadvantages are mentioned. Subsequently, the F-Bar method to avoid volumetric locking, which is mentioned in chapter 3, is examined. Finally, different hardening mechanisms and mesh separation methods are compared. All this is done in simple validation examples.

According to the comparison in chapter 5, the implementation details are chosen based on their advantages, and in chapter 6, together with the material model, they are applied to the micro-cutting process. The chapter is divided into two parts. In the first part, the challenges on the micro-cutting simulations are shown, and the influence of different process parameters on the micro-cutting process indicated. For this purpose, simulations with varying crystal orientation, cutting depth, and rake angle are executed. Furthermore, the micro-cutting simulation is performed with the introduced hardening mechanisms. In the second part, the exemplary microstructure of the workpiece is replaced by a real structure. A way is shown how this real structure can be determined. Then the influence of the real structure and the size of the mesh elements in the separation and chip area on the process is studied. Finally, it is investigated whether the additional so-called $\langle c + a \rangle$ slip systems can be neglected for the micro-cutting process by adding them to the material model and execute the simulation again with the real structure.

Chapter 7 covers the conclusion of the work and provides an outlook to further research.

Chapter 2

Continuum Mechanics

In this work, the crystal plastic behavior of commercially pure (cp-)titanium is investigated. To this end, the crystal plastic material behavior, which is mainly characterized by the crystalline slip systems, is described by a continuum theory. This chapter outlines the basic principles of continuum mechanics and introduces the crystal plastic material model that is the main topic of this work. The chapter concludes with a description of the so-called weak form of the equilibrium equation and its linearization with respect to the displacement field. The linearization forms the basis for the numerical solution strategy that is described in the next chapter.

In the continuum theory for the introduction of the basic formulas, the undeformed body \mathcal{B} in the reference configuration, respectively, its deformed, spatial shape \mathcal{R} in the current configuration is observed.

The fundamentals that are outlined, generally follow the standard literature, for example, Wriggers (2008), Holzapfel (2000), and de Souza Neto et al. (2011). The interested reader will find further literature in the bibliography.

2.1 Kinematics

In continuum mechanics, a body \mathcal{B} is considered as a continuous composition of particles or material points, denoted by $\mathcal{P} \in \mathcal{B}$, and can be identified with a region Ω in the three-dimensional Euclidean space \mathbb{E}^3 with a regular boundary $\partial\Omega$. The motion and deformation of \mathcal{B} is described through a function φ , which maps every particle from a reference configuration Ω_0 at $t = 0$ to a deformed, current configuration Ω_t at time t . The particles in the reference configuration are identified by \mathbf{X} and for the position \mathbf{x} of a particle in the current configuration at time t applies

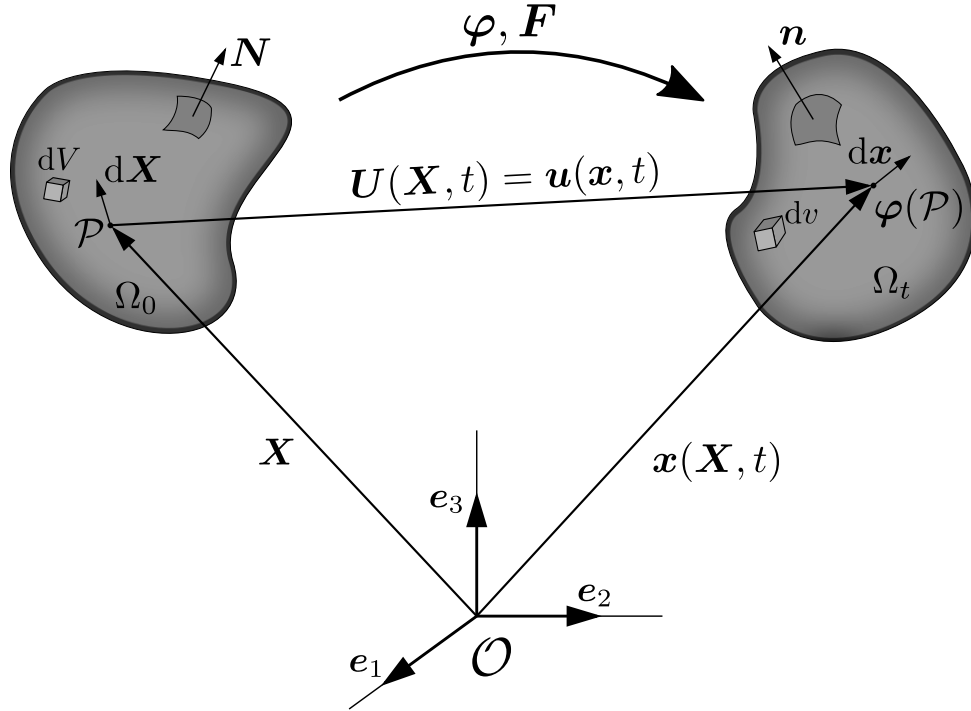
$$\mathbf{x} = \varphi(\mathbf{X}, t). \quad (2.1)$$

The coordinates \mathbf{X} of the material points in the reference configuration are also called reference (Lagrangian) coordinates. The coordinates \mathbf{x} of the material points in the current configuration are called spatial (Eulerian) coordinates. The deformation φ is assumed to be uniquely invertible

$$\mathbf{X} = \varphi^{-1}(\mathbf{x}, t). \quad (2.2)$$

For convenience, in the following, quantities in capital letters indicate quantities defined in the reference configuration, whereas small letters refer to quantities of the current configuration. As an example, the displacement of a point \mathcal{P} can be expressed as a field of the reference coordinates $\mathbf{U}(\mathbf{X}, t)$ or as a field of the spatial coordinates $\mathbf{u}(\mathbf{x}, t)$, i.e.

$$\mathbf{U}(\mathbf{X}, t) = \mathbf{x}(\mathbf{X}, t) - \mathbf{X} = \mathbf{x} - \mathbf{X}(\mathbf{x}, t) = \mathbf{u}(\mathbf{x}, t). \quad (2.3)$$

FIGURE 2.1: Reference and current configuration of body \mathcal{B} .

2.1.1 Deformation Gradient

To describe the local deformation, the deformation gradient \mathbf{F} is introduced. The deformation gradient maps infinitesimal small line elements $d\mathbf{X}$ in the reference configuration to the respective small line elements $d\mathbf{x}$ in the current configuration, i.e.

$$d\mathbf{x} = \mathbf{F} d\mathbf{X}. \quad (2.4)$$

Consequently, the deformation gradient is defined as

$$\mathbf{F}(\mathbf{X}, t) = \frac{\partial \varphi(\mathbf{X}, t)}{\partial \mathbf{X}} = \frac{\partial \mathbf{x}}{\partial \mathbf{X}} = \text{Grad } \mathbf{x}. \quad (2.5)$$

In Equation (2.5) “Grad” denotes the gradient with respect to \mathbf{X} . To preserve a continuous structure of \mathcal{B} and prevent self-penetration the following condition for the Jacobian determinant J applies

$$J = \det \mathbf{F} > 0. \quad (2.6)$$

Thus, the inverse of the deformation gradient exists and satisfies

$$d\mathbf{X} = \mathbf{F}^{-1} d\mathbf{x}, \quad \mathbf{F}^{-1} = \frac{\partial \varphi^{-1}(\mathbf{x}, t)}{\partial \mathbf{x}} = \frac{\partial \mathbf{X}}{\partial \mathbf{x}}. \quad (2.7)$$

Figure 2.1 illustrates the deformation of a body \mathcal{B} . With Equation (2.3) the deformation gradient can alternatively be expressed in terms of the displacement \mathbf{u}

$$\mathbf{F} = \text{Grad}(\mathbf{X} + \mathbf{u}) = \mathbf{I} + \text{Grad } \mathbf{u} = \mathbf{I} + \mathbf{H}, \quad (2.8)$$

where $\mathbf{H} = \text{Grad } \mathbf{u}$ is the displacement gradient and \mathbf{I} is the second-order identity tensor. Since the deformation gradient is known for a given motion, the transformation

of area elements is determined by the formula of Nanson

$$d\mathbf{a} = \mathbf{n} da = J\mathbf{F}^{-T}\mathbf{N}dA = J\mathbf{F}^{-T}d\mathbf{A}. \quad (2.9)$$

Furthermore, the relation

$$dv = J dV \quad (2.10)$$

holds for the transformation of volume elements between configurations. Besides, the deformation gradient can be decomposed by the polar decomposition theorem into a proper orthogonal rotation tensor \mathbf{R} and the symmetric positive definite tensors \mathbf{U} and \mathbf{V} , respectively, as

$$\mathbf{F} = \mathbf{R}\mathbf{U} = \mathbf{V}\mathbf{R}. \quad (2.11)$$

The dependence of the deformation $\varphi(\mathbf{X}, t)$ on time has to be considered for nonlinear problems like plastic material, which is also subject of this work. For this reason, some aspects of the derivative of the deformation gradient with respect to time are discussed here. By the introduction of the spatial velocity field

$$\mathbf{v}(\mathbf{X}, t) = \frac{\partial\varphi(\mathbf{X}, t)}{\partial t} = \dot{\varphi}(\mathbf{X}, t), \quad (2.12)$$

the spatial velocity gradient \mathbf{l} is obtained by the equation

$$\mathbf{l}(\mathbf{x}, t) = \frac{\partial\mathbf{v}(\mathbf{x}, t)}{\partial\mathbf{x}} = \text{grad } \mathbf{v}(\mathbf{x}, t). \quad (2.13)$$

The material time derivative of the deformation gradient has the form

$$\dot{\mathbf{F}}(\mathbf{X}, t) = \frac{\partial}{\partial t} \left(\frac{\partial\varphi(\mathbf{X}, t)}{\partial\mathbf{X}} \right) = \frac{\partial}{\partial\mathbf{X}} \left(\frac{\partial\varphi(\mathbf{X}, t)}{\partial t} \right) = \frac{\partial\mathbf{v}(\mathbf{X}, t)}{\partial\mathbf{X}} = \text{Grad } \mathbf{v}(\mathbf{X}, t). \quad (2.14)$$

Thus, the spatial velocity gradient \mathbf{l} can be expressed by means of $\dot{\mathbf{F}}$ and the chain rule as

$$\mathbf{l} = \frac{\partial\mathbf{v}}{\partial\mathbf{x}} = \frac{\partial\dot{\varphi}(\mathbf{X}, t)}{\partial\mathbf{X}} \frac{\partial\mathbf{X}}{\partial\mathbf{x}} = \frac{\partial}{\partial t} \left(\frac{\partial\varphi(\mathbf{X}, t)}{\partial\mathbf{X}} \right) \mathbf{F}^{-1} = \dot{\mathbf{F}}\mathbf{F}^{-1} \quad (2.15)$$

and can be decomposed into a symmetric part \mathbf{d} and an antisymmetric part \mathbf{w} according to

$$\mathbf{d} = \frac{1}{2}(\mathbf{l} + \mathbf{l}^T) = \frac{1}{2}(\text{grad } \mathbf{v} + \text{grad}^T \mathbf{v}), \quad \mathbf{w} = \frac{1}{2}(\mathbf{l} - \mathbf{l}^T) = \frac{1}{2}(\text{grad } \mathbf{v} - \text{grad}^T \mathbf{v}). \quad (2.16)$$

In (2.16) \mathbf{d} and \mathbf{w} denote the rate of deformation tensor and the spin tensor, respectively. The superscript $(*)^T$ denotes the transpose of the tensor.

2.1.2 Isochoric/Volumetric Split of the Deformation Gradient

In some cases, the deformation underlies specific constraint conditions. For example the plastic deformation of metals or the deformation of rubber materials is considered as incompressible and the condition $(\det \mathbf{F}) = J = 1$ has to be fulfilled. In those cases, it is convenient to incorporate these constraint conditions directly into the kinematical relations. The deformation can be decomposed in a purely volumetric and a purely isochoric deformation by a multiplicative split

$$\mathbf{F} = \mathbf{F}_{\text{iso}}\mathbf{F}_{\text{v}} = \mathbf{F}_{\text{v}}\mathbf{F}_{\text{iso}}, \quad (2.17)$$

where \mathbf{F}_{iso} is the isochoric or volume-preserving and \mathbf{F}_v is the volumetric part of \mathbf{F} . The two parts of \mathbf{F} are defined as

$$\mathbf{F}_{\text{iso}} = (\det \mathbf{F})^{-\frac{1}{3}} \mathbf{F}, \quad \mathbf{F}_v = (\det \mathbf{F})^{\frac{1}{3}} \mathbf{I} \quad (2.18)$$

and it can be shown, that, by construction, the isochoric component produces a volume-preserving deformation

$$\det \mathbf{F}_{\text{iso}} = [(\det \mathbf{F})^{-\frac{1}{3}}]^3 \det \mathbf{F} = 1, \quad (2.19)$$

while the volumetric part produce to the same volume change as \mathbf{F}

$$\det \mathbf{F}_v = [(\det \mathbf{F})^{\frac{1}{3}}]^3 \det \mathbf{I} = \det \mathbf{F}. \quad (2.20)$$

2.1.3 Strain Measures

Strain measures are required to quantify the deformation of a certain material point in order to express constitutive laws. The rotational part \mathbf{R} included in the deformation gradient \mathbf{F} , compare section (2.1.1), leads to a pure rotation, which does not change the distance between material particles. In contrast, the tensors \mathbf{U} and \mathbf{V} , by means of the polar decomposition, measure local stretching of material points. Thus \mathbf{U} and \mathbf{V} are suited to define strain measures. The computation of \mathbf{U} and \mathbf{V} is rather cumbersome, because the square root of $\mathbf{F}^T \mathbf{F}$ and $\mathbf{F} \mathbf{F}^T$ is needed, we introduce the right and left Cauchy-Green Tensor, \mathbf{C} and \mathbf{B} , defined by

$$\mathbf{C} = \mathbf{U}^2 = \mathbf{F}^T \mathbf{F}, \quad \mathbf{B} = \mathbf{V}^2 = \mathbf{F} \mathbf{F}^T. \quad (2.21)$$

Since, these strain measures are not zero for a rigid body motion without any strain, where $\mathbf{F} = \mathbf{I} \rightarrow \mathbf{C} = \mathbf{B} = \mathbf{I}$, it is convenient to define a further strain measure, the Green-Lagrange strain tensor

$$\mathbf{E} = \frac{1}{2}(\mathbf{C} - \mathbf{I}) = \frac{1}{2}(\mathbf{F}^T \mathbf{F} - \mathbf{I}), \quad (2.22)$$

which is defined in the reference configuration. The Euler-Almansi Strain tensor \mathbf{e} , the counterpart of \mathbf{E} in the spatial configuration, is defined as

$$\mathbf{e} = \frac{1}{2}(\mathbf{I} - \mathbf{B}^{-1}) = \frac{1}{2}(\mathbf{I} - \mathbf{F}^{-T} \mathbf{F}^{-1}). \quad (2.23)$$

Note, that all strain tensors mentioned in this section are symmetric tensors. For an interpretation of \mathbf{E} and \mathbf{e} it is helpful to consider the change of the squared length of line elements $dS^2 = d\mathbf{X} \cdot d\mathbf{X}$ and $ds^2 = d\mathbf{x} \cdot d\mathbf{x}$ which can be expressed as

$$ds^2 - dS^2 = d\mathbf{x} \cdot d\mathbf{x} - d\mathbf{X} \cdot d\mathbf{X} = 2 d\mathbf{X} \cdot (\mathbf{E} d\mathbf{X}), \quad (2.24)$$

$$ds^2 - dS^2 = d\mathbf{x} \cdot d\mathbf{x} - d\mathbf{X} \cdot d\mathbf{X} = 2 d\mathbf{x} \cdot (\mathbf{e} d\mathbf{x}). \quad (2.25)$$

2.2 Stress Measures

In the previous sections the description has been limited to the kinematics of the deformation of a solid body. No statements about forces and their influence on the material points of the body are made. The forces, that are applied to a body can be classified into body forces, exerted inside the body, and boundary forces. Due to applied external forces, an internal stress state results inside the body. By an

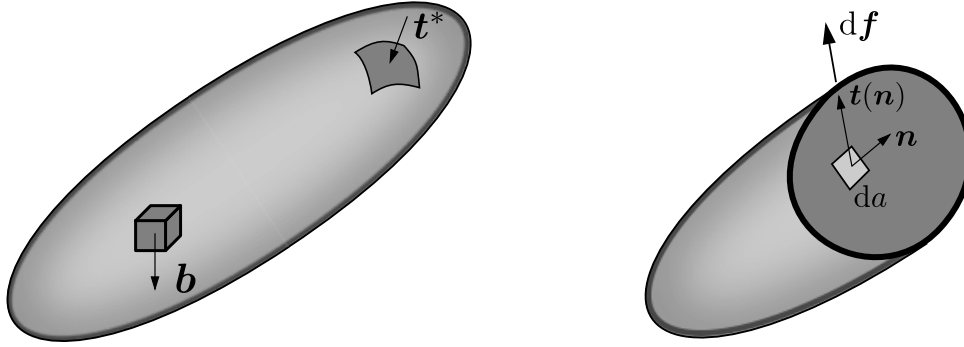


FIGURE 2.2: External forces and stress vector.

imaginary cut of the body into two pieces, see Figure 2.2, with the surface normal \mathbf{n} , we can define the infinitesimal force $d\mathbf{f}$, acting on the infinitesimal surface element da of the interface. The traction vector $\mathbf{t} = \mathbf{t}(\mathbf{x}, \mathbf{n}, t)$ is defined as the force $d\mathbf{f}$ related to the surface element da

$$\mathbf{t}(\mathbf{x}, \mathbf{n}, t) = \frac{d\mathbf{f}}{da}, \quad (2.26)$$

and can be decomposed in a part normal to the surface, which is called the normal stress $\sigma = \mathbf{t} \cdot \mathbf{n}$, and a tangential part, the shear stress

$$\tau = \sqrt{\mathbf{t} \cdot \mathbf{t} - \sigma^2}. \quad (2.27)$$

The relation of the traction vector and the surface normal is given by Cauchy's theorem

$$\mathbf{t} = \boldsymbol{\sigma}^T \mathbf{n}. \quad (2.28)$$

In Equation (2.28), the second-order tensor $\boldsymbol{\sigma}$ is defined as the Cauchy stress tensor

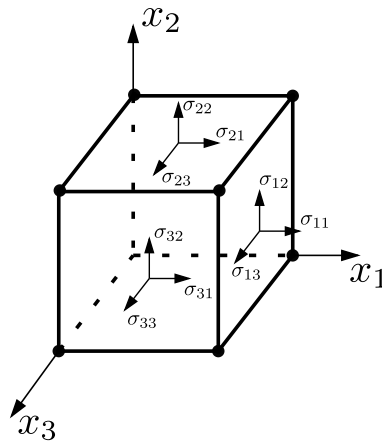


FIGURE 2.3: Components of the Cauchy stress tensor.

and describes a unique stress state of a material point. The components of $\boldsymbol{\sigma}$ can be obtained by three traction vectors related to three non-coplanar cutting planes, see Figure 2.3,

$$\boldsymbol{\sigma} = \begin{bmatrix} \mathbf{t}_1 \\ \mathbf{t}_2 \\ \mathbf{t}_3 \end{bmatrix} = \begin{bmatrix} \sigma_{11} & \sigma_{12} & \sigma_{13} \\ \sigma_{21} & \sigma_{22} & \sigma_{23} \\ \sigma_{31} & \sigma_{32} & \sigma_{33} \end{bmatrix} = \begin{bmatrix} \sigma_{11} & \tau_{12} & \tau_{13} \\ \tau_{21} & \sigma_{22} & \tau_{23} \\ \tau_{31} & \tau_{32} & \sigma_{33} \end{bmatrix}. \quad (2.29)$$

The Cauchy stress tensor is a symmetric tensor, see Section 2.3.2, and describes the actual stress of the current configuration. In this work, three other important stress tensors are used, which can be obtained by certain transformations of $\boldsymbol{\sigma}$. The first Piola-Kirchhoff stress tensor \mathbf{P} describes the actual internal forces per surface element dA of the reference configuration and can be transformed by

$$\mathbf{P} = J\boldsymbol{\sigma}\mathbf{F}^{-T}. \quad (2.30)$$

In contrast to the first Piola-Kirchhoff stress tensor, which is in general non-symmetric, the second Piola-Kirchhoff stress tensor \mathbf{S} is a symmetric tensor and is defined with regard to the reference configuration

$$\mathbf{S} = \mathbf{F}^{-1}\mathbf{P} = J\mathbf{F}^{-1}\boldsymbol{\sigma}\mathbf{F}^{-T}. \quad (2.31)$$

Besides the Cauchy stress tensor, the Kirchhoff stress tensor $\boldsymbol{\tau}$ is another stress measure, which is defined in the current configuration and can be obtained by

$$\boldsymbol{\tau} = \mathbf{F}\mathbf{S}\mathbf{F}^T = J\boldsymbol{\sigma}. \quad (2.32)$$

2.3 Balance Laws and Thermodynamics

In continuum mechanics, certain physical postulates are expressed by balance laws that need to be fulfilled. As an example, the first and second principle of thermodynamics must not be violated for the formulation of the constitutive equations, which is explained for the material model utilized in this work in the following.

2.3.1 Conservation of Mass

The mass m is a fundamental physical property of a body \mathcal{B} and cannot be produced or destroyed. Consequently, the mass of a body is a conserved quantity, which is described by the relation

$$m = \int_{\mathcal{B}} \rho_0 \, dV = \int_{\mathcal{R}} \rho \, dv = \text{const.}, \quad (2.33)$$

where ρ_0 is the density in the reference configuration and ρ the density in the current configuration.

2.3.2 Balance of Linear Momentum and Angular Momentum

The linear momentum of a body \mathcal{B} is a global quantity that describes the kinetic state of a body and it is defined by

$$\mathbf{L}(t) = \int_{\mathcal{R}} \rho \mathbf{v} \, dv. \quad (2.34)$$

The postulation of the balance of linear momentum states that the temporal change of the linear momentum is equal to the external traction and body loads of a body and is equivalent to Newton's second principle of motion. For a continuous body, it can be expressed as

$$\frac{d}{dt} \int_{\mathcal{R}} \rho \mathbf{v} \, dv = \int_{\partial\mathcal{R}} \mathbf{t} \, da + \int_{\mathcal{R}} \rho \mathbf{b} \, dv. \quad (2.35)$$

By means of Cauchy's stress theorem (2.28) and by using the conservation of mass and the divergence theorem, the local balance of linear momentum is derived from Equation (2.35) as

$$\rho \dot{\mathbf{v}} = \operatorname{div} \boldsymbol{\sigma}^T + \rho \mathbf{b}, \quad (2.36)$$

which is also known as the equation of motion. The derivation of the balance of the angular momentum is similar to the derivation of the balance of the linear momentum. Starting with the angular momentum

$$\mathbf{J}(t) = \int_{\mathcal{R}} \mathbf{r}(\mathbf{x}) \times (\rho \mathbf{v}) \, dv, \quad (2.37)$$

where the vector $\mathbf{r}(\mathbf{x}) = \mathbf{x} - \mathbf{x}_0$, \mathbf{x}_0 is a fixed reference position and \times denotes the cross product of two vectors. The balance of the angular momentum is postulated as the equality of the temporal change of the angular momentum and the total moment of the external loads

$$\frac{d}{dt} \int_{\mathcal{R}} \mathbf{r} \times (\rho \mathbf{v}) \, dv = \int_{\partial \mathcal{R}} \mathbf{r} \times \mathbf{t} \, da + \int_{\mathcal{R}} \mathbf{r} \times \rho \mathbf{b} \, dv. \quad (2.38)$$

The balance of angular momentum (2.38) can be rewritten, using the divergence theorem, Cauchy's theorem (2.28) and the balance of mass (2.33), as

$$\boldsymbol{\sigma} = \boldsymbol{\sigma}^T. \quad (2.39)$$

Thus, $\boldsymbol{\sigma}$ is symmetric. As long as inertial effects can be neglected, Equation (2.35) and Equation (2.36), together with Equation (2.39), result in

$$\int_{\partial \mathcal{R}} \boldsymbol{\sigma} \mathbf{n} \, da + \int_{\mathcal{R}} \rho \mathbf{b} \, dv = \int_{\mathcal{R}} (\operatorname{div} \boldsymbol{\sigma} + \rho \mathbf{b}) \, dv = \mathbf{0} \quad \text{and} \quad \operatorname{div} \boldsymbol{\sigma} + \rho \mathbf{b} = \mathbf{0}, \quad (2.40)$$

which denote the global and the local equilibrium equation in the current configuration, respectively. In Equation (2.40) the divergence is defined with respect to the current configuration. The local equilibrium equation can be rewritten in the reference configuration as

$$\operatorname{Div} \mathbf{P} + \rho_0 \mathbf{b} = \mathbf{0}, \quad (2.41)$$

where the divergence operator is defined with respect to the reference configuration, which can be recognized by the capitalization.

2.3.3 First Law of Thermodynamics

The first law of thermodynamics postulates the conservation of energy in a body and can be expressed as

$$\frac{d}{dt} \mathcal{W} = \mathcal{P} + \mathcal{Q}, \quad (2.42)$$

where \mathcal{W} is the total energy, \mathcal{P} is the power of the external loads or the external mechanical power

$$\mathcal{P} = \int_{\partial \mathcal{R}} \mathbf{t} \cdot \mathbf{v} \, da + \int_{\mathcal{R}} \mathbf{b} \cdot \mathbf{v} \, dv, \quad (2.43)$$

and \mathcal{Q} is the thermal power. Furthermore, the total energy is the sum of the internal energy \mathcal{U} and the kinetic energy \mathcal{K} , i.e.

$$\mathcal{W} = \mathcal{U} + \mathcal{K} \quad (2.44)$$

where

$$\mathcal{U} = \int_{\mathcal{R}} \rho u \, dv \quad \text{and} \quad \mathcal{K} = \frac{1}{2} \int_{\mathcal{R}} \rho \mathbf{v} \cdot \mathbf{v} \, dv. \quad (2.45)$$

In Equation (2.45) u represents the internal energy density per unit mass. The thermal power \mathcal{Q} is composed of heat supply due to a heat source r and heat supply due to heat flux \mathbf{h} across the boundary, i.e.

$$\mathcal{Q} = \int_{\mathcal{R}} \rho r \, dv - \int_{\partial\mathcal{R}} \mathbf{h} \cdot \mathbf{n} \, da. \quad (2.46)$$

Thus, Equation (2.42) becomes

$$\frac{d}{dt} \int_{\mathcal{R}} \left(u + \frac{1}{2} \mathbf{v} \cdot \mathbf{v} \right) \rho \, dv = \int_{\partial\mathcal{R}} \mathbf{t} \cdot \mathbf{v} \, da + \int_{\mathcal{R}} \mathbf{b} \cdot \mathbf{v} \, dv + \int_{\mathcal{R}} \rho r \, dv - \int_{\partial\mathcal{R}} \mathbf{h} \cdot \mathbf{n} \, da. \quad (2.47)$$

Furthermore, the balance of energy can be rewritten by means of the balance of linear momentum, the conservation of mass, and the divergence theorem as

$$\int_{\mathcal{R}} (\rho \dot{u} - \boldsymbol{\sigma} : \mathbf{d} - \rho r + \operatorname{div} \mathbf{h}) \, dv = 0, \quad (2.48)$$

where \mathbf{d} is the symmetric part of the spatial velocity gradient, see Equation (2.16), and is received from the velocity terms of Equation (2.47). The local form leads to

$$\rho \dot{u} = \boldsymbol{\sigma} : \mathbf{d} + \rho r - \operatorname{div} \mathbf{h}. \quad (2.49)$$

The term $\boldsymbol{\sigma} : \mathbf{d}$ denotes the stress power.

2.3.4 Second Law of Thermodynamics and Dissipation

The main statement of the first law of thermodynamics is that energy can neither be created nor destroyed. Energy can only be transformed into another form of energy. However, a real process underlies always a specific direction, e.g., heat always flows from a warmer to a colder region. The second law of thermodynamics postulates this irreversibility of processes and the direction of energy transfer processes. It is based on the concept of entropy. The entropy, denoted by $\mathcal{S}(t)$, is defined as

$$\mathcal{S}(t) = \int_{\mathcal{R}} \rho s(\mathbf{x}, t) \, dv, \quad (2.50)$$

with s as specific internal entropy per unit mass. The second law of thermodynamics in global form states that

$$\frac{d}{dt} \int_{\mathcal{R}} \rho s \, dv \geq \int_{\mathcal{R}} \frac{\rho r}{\theta} \, dv - \int_{\partial\mathcal{R}} \frac{\mathbf{h} \cdot \mathbf{n}}{\theta} \, da, \quad (2.51)$$

which is also called the Clausius-Duhem-Inequality. In Equation (2.51) θ is the absolute temperature usually measured in Kelvin. Equation (2.51) can be rewritten, by means of the balance of mass and the divergence theorem, to the local form

$$\rho\theta\dot{s} \geq \rho r - \operatorname{div}\mathbf{h} + \frac{1}{\theta}\mathbf{h} \cdot \operatorname{grad}\theta. \quad (2.52)$$

Introducing the specific free energy, also known as Helmholtz free energy, as

$$\psi = u - \theta s \quad (2.53)$$

and using Equation (2.49), the second law can be reformulated as

$$\boldsymbol{\sigma} : \mathbf{d} - \rho\dot{\psi} - \rho s\dot{\theta} - \frac{1}{\theta}\mathbf{h} \cdot \operatorname{grad}\theta \geq 0. \quad (2.54)$$

Neglecting the influence of the temperature, the equation

$$\boldsymbol{\sigma} : \mathbf{d} - \rho\dot{\psi} = \phi \geq 0, \quad (2.55)$$

defines the specific dissipation function ϕ per unit volume of the current configuration. In this work, the Helmholtz free energy is postulated as a function of the form

$$\psi = \psi(\mathbf{F}, \theta, \boldsymbol{\alpha}). \quad (2.56)$$

The internal variable $\boldsymbol{\alpha}$ with components $\{\alpha_k\}$, which is, in general, of scalar, vectorial or tensorial nature, is associated with dissipative mechanisms. With Equation (2.56) the rate of ψ is given by

$$\dot{\psi} = \frac{\partial\psi}{\partial\mathbf{F}} : \dot{\mathbf{F}} + \frac{\partial\psi}{\partial\theta}\dot{\theta} + \frac{\partial\psi}{\partial\alpha_k}\dot{\alpha}_k, \quad (2.57)$$

where Einstein's summation convention is applied in the last term. The stress power can be transformed to

$$\boldsymbol{\sigma} : \mathbf{d} = \boldsymbol{\sigma}\mathbf{F}^{-T} : \dot{\mathbf{F}} \quad (2.58)$$

which can be substituted into the Clausius-Duhem inequality, alongside Equation (2.57), i.e.

$$\left(\boldsymbol{\sigma}\mathbf{F}^{-T} - \rho\frac{\partial\psi}{\partial\mathbf{F}}\right) : \dot{\mathbf{F}} - \rho\left(s + \frac{\partial\psi}{\partial\theta}\right)\dot{\theta} - \rho\frac{\partial\psi}{\partial\alpha_k}\dot{\alpha}_k - \frac{1}{\theta}\mathbf{h} \cdot \operatorname{grad}\theta \geq 0. \quad (2.59)$$

The Clausius-Duhem inequality has to be fulfilled for any thermokinetic process, which implies Equation (2.59) must remain valid for any pair of functions $\{\dot{\mathbf{F}}(t), \dot{\theta}(t)\}$. From this the constitutive equations

$$\boldsymbol{\sigma} = \rho\frac{\partial\psi}{\partial\mathbf{F}}\mathbf{F}^T \quad \text{and} \quad s = -\frac{\partial\psi}{\partial\theta} \quad (2.60)$$

follow. For the internal variables α_k , a conjugate thermodynamical force can be defined as

$$A_k = \rho\frac{\partial\psi}{\partial\alpha_k}. \quad (2.61)$$

With this definition and the constitutive equations (2.60), the Clausius-Duhem inequality is obtained in the form

$$-A_k \dot{\alpha}_k - \frac{1}{\theta} \mathbf{h} \cdot \text{grad} \theta \geq 0. \quad (2.62)$$

To complete the constitutive description, complementary laws for the variables $\dot{\alpha}$ and $\frac{1}{\theta} \mathbf{h}$ must be postulated. In general, it is assumed, that the variables are functions of the form

$$\dot{\alpha} = f(\mathbf{F}, \theta, \text{grad} \theta, \alpha), \quad (2.63)$$

$$\frac{1}{\theta} \mathbf{h} = g(\mathbf{F}, \theta, \text{grad} \theta, \alpha). \quad (2.64)$$

For each process, the Clausius-Duhem inequality must hold, resulting in constraints on the general functions f and g .

2.4 Constitutive Model

In the previous sections, the kinematical relations, the concept of stress, and the balance laws are described. However, in order to be able to solve a problem in continuum mechanics, the description of the material behavior is needed. In Section 2.3.4, the constitutive assumptions for the Helmholtz free energy and the consequence of the Clausius-Duhem inequality are described. In this section, the relevant aspects of crystal elastoplastic material behavior, that are fundamental to this work, will be discussed. The influence of the temperature is neglected for the material model so that any term with a contribution of θ vanishes.

2.4.1 Hyperelasticity

Hyperelastic models are non-dissipative, and thus the consideration of internal variables is not needed. Hyperelastic material laws are suitable to describe the elastic deformation of a body, which undergoes large deformation, e.g., rubber materials. Such materials are characterized by a specific Helmholtz free energy of the form

$$\psi = \psi(\mathbf{F}), \quad (2.65)$$

which is a particular case of the general form, see Equation (2.56). For isotropic material, the free energy has to satisfy

$$\psi(\mathbf{F}\mathbf{Q}) = \psi(\mathbf{F}), \quad (2.66)$$

for any orthogonal rotation tensor \mathbf{Q} , e.g. $\mathbf{Q} = \mathbf{R}^T$. The free energy (2.65) can also be expressed as a function of the right or left Cauchy-Green strain tensor as the reduced form $\bar{\psi}$. With Equation (2.11) and (2.66), one obtains

$$\psi(\mathbf{F}) = \psi(\mathbf{U}) = \psi(\mathbf{V}) = \bar{\psi}(\mathbf{C}) = \bar{\psi}(\mathbf{B}) \quad (2.67)$$

for an isotropic hyperelastic material. In this case, the constitutive equation for the Kirchhoff stress $\boldsymbol{\tau}$ and the Cauchy stress $\boldsymbol{\sigma}$ are

$$\boldsymbol{\tau} = \bar{\boldsymbol{\tau}}(\mathbf{B}) = 2\rho_0 \frac{\partial \bar{\psi}}{\partial \mathbf{B}} \mathbf{B} \quad \text{and} \quad \boldsymbol{\sigma} = \bar{\boldsymbol{\sigma}}(\mathbf{B}) = 2\rho \frac{\partial \bar{\psi}}{\partial \mathbf{B}} \mathbf{B}. \quad (2.68)$$

The isotropy requirement also implies, that $\bar{\psi}$ can be formulated as a function of the principal invariants of \mathbf{C} or \mathbf{B} , such that

$$\bar{\psi}(\mathbf{C}) = \bar{\psi}(I_{\mathbf{C}}, \mathbb{I}_{\mathbf{C}}, \mathbb{III}_{\mathbf{C}}) = \bar{\psi}(I_{\mathbf{B}}, \mathbb{I}_{\mathbf{B}}, \mathbb{III}_{\mathbf{B}}) = \bar{\psi}(\mathbf{B}) \quad (2.69)$$

with the invariants

$$\begin{aligned} I_{\mathbf{C}} &= \text{tr } \mathbf{C}, & I_{\mathbf{B}} &= \text{tr } \mathbf{B}, \\ \mathbb{I}_{\mathbf{C}} &= \frac{1}{2} \left[(\text{tr } \mathbf{C})^2 - \text{tr } (\mathbf{C}^2) \right], & \mathbb{I}_{\mathbf{B}} &= \frac{1}{2} \left[(\text{tr } \mathbf{B})^2 - \text{tr } (\mathbf{B}^2) \right], \\ \mathbb{III}_{\mathbf{C}} &= \det \mathbf{C}, & \mathbb{III}_{\mathbf{B}} &= \det \mathbf{B}, \end{aligned} \quad (2.70)$$

where $\text{tr}(\mathbf{A})$ denotes the trace of an arbitrary tensor \mathbf{A} . In this work, a compressible neo-Hookean material is used. Therefore, the free energy is defined as a function of the first invariant of the left Cauchy-Green strain tensor and the determinant of the deformation gradient J

$$\rho_0 \bar{\psi}(I_{\mathbf{B}}, J) = \frac{1}{2} G (I_{\mathbf{B}} - 3) + \frac{1}{2} K [\ln(J)]^2, \quad (2.71)$$

where the material constants G and K denote the shear and bulk modulus. The first term of Equation (2.71) is related to the isochoric part of the deformation, while the second term represents the Helmholtz free energy due to volumetric deformation.

2.4.2 Crystal Plasticity for Finite Deformations

In this section, a crystal plasticity model for finite strains that uses a hyperelastic model for the elastic part of the deformation is introduced. The underlying assumption of the material model is that the deformation gradient can be decomposed multiplicatively into an elastic and plastic part. This is explained in more detail in the following section. The elastic contribution is modeled by the hyperelastic neo-Hookean material model, introduced in the previous section.

Decomposition of the deformation gradient

As described before, the main hypothesis that allows to model plasticity for large deformation is the multiplicative decomposition of the deformation gradient in elastic and plastic contribution. This split is based on the work of Lee and Liu (1967) and Lee (1969), which shows that the deformation can be represented as a sequence of configurations, starting from the initial reference configuration. In order to describe plasticity, a local unstressed intermediate plastic configuration, described by \mathbf{F}^p is introduced, see Figure 2.4. The decomposition is defined by

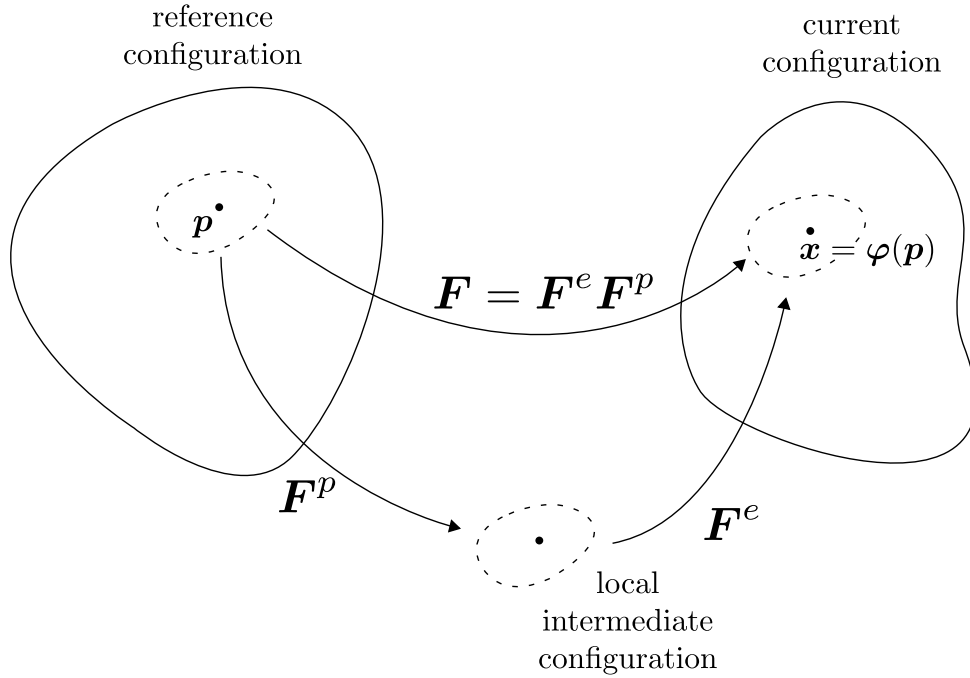
$$\mathbf{F} = \mathbf{F}^e \mathbf{F}^p. \quad (2.72)$$

The polar decomposition, see Equation (2.11), can also be applied to the elastic and plastic deformation gradient, i.e.

$$\mathbf{F}^e = \mathbf{R}^e \mathbf{U}^e = \mathbf{V}^e \mathbf{R}^e \quad (2.73)$$

and

$$\mathbf{F}^p = \mathbf{R}^p \mathbf{U}^p = \mathbf{V}^p \mathbf{R}^p. \quad (2.74)$$

FIGURE 2.4: Multiplicative decomposition of \mathbf{F} .

The interpretation of these tensors is similar to the interpretation of \mathbf{U} , \mathbf{V} and \mathbf{R} obtained from the polar decomposition of the total deformation gradient. By substituting Equation (2.72) in Equation (2.15), the velocity gradient can be computed as

$$\mathbf{l} = \mathbf{l}^e + \mathbf{F}^e \mathbf{l}^p (\mathbf{F}^e)^{-1}, \quad (2.75)$$

where the elastic and plastic velocity gradient are defined as

$$\mathbf{l}^e = \dot{\mathbf{F}}^e (\mathbf{F}^e)^{-1} \quad \text{and} \quad \mathbf{l}^p = \dot{\mathbf{F}}^p (\mathbf{F}^p)^{-1}. \quad (2.76)$$

Furthermore, strain tensors for the elastic part of the deformation can be specified similar to Section 2.1.3 as the right and left elastic Cauchy-Green Tensor, i.e.

$$\mathbf{C}^e = (\mathbf{F}^e)^T \mathbf{F}^e \quad \text{and} \quad \mathbf{B}^e = \mathbf{F}^e (\mathbf{F}^e)^T, \quad (2.77)$$

respectively. Note, that the plastic velocity gradient \mathbf{l}^p and the right elastic Cauchy-Green tensor \mathbf{C}^e are quantities of the intermediate configuration.

Finite strain elastoplastic model of single crystals

The decomposition of \mathbf{F} in elastic and plastic parts is the basis of the elastoplastic model of a single crystal at finite strains. Considering the deformation of a crystal lattice, the plastic deformation is the result of microscopic sliding along crystallographic slip systems, while the elastic contribution represents a reverse rotation and distortion of the lattice. This difference between elastic and plastic deformation is illustrated in Figure 2.5. The plastic deformation gradient describes a deviation from the initial state, $\mathbf{F}^p = \mathbf{I}$, by the plastic slip along the slip system $\{\mathbf{s}, \mathbf{n}\}$ defined by slip plane normal \mathbf{n} and slip direction \mathbf{s} with the magnitude γ , also known as the plastic slip or plastic multiplier, i.e.

$$\mathbf{F}^p = \mathbf{I} + \gamma \mathbf{s} \otimes \mathbf{n}. \quad (2.78)$$

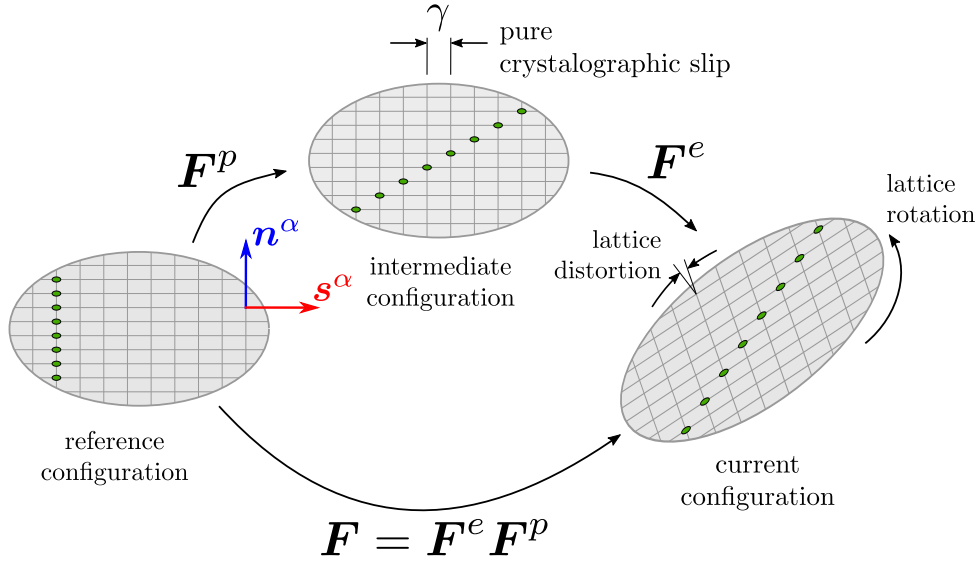


FIGURE 2.5: Elastic and plastic deformation of crystal lattice.
(Own figure based on de Souza Neto et al. (2011))

In Equation (2.78) the symbol ' \otimes ' denotes the dyadic product between two vectors. In general, a crystal lattice has more than one slip system. This is the reason why all quantities which belong to a certain slip system are marked by a superscript. In addition it is convenient to mirror each physical slip system to recognize plastic slip in the opposite direction of \mathbf{s} . For each

$$\{\mathbf{s}^\alpha, \mathbf{n}^\alpha\} \quad \text{a mirrored system} \quad \{\mathbf{s}^\beta, \mathbf{n}^\beta\} = \{-\mathbf{s}^\alpha, \mathbf{n}^\alpha\} \quad (2.79)$$

is introduced. Hence, for a crystal unit cell with N_{sls} slip systems, one obtains a total number of $2 \cdot N_{\text{sls}}$. For the case of multiple slip system, i.e. the multislip case, plastic yielding along the slip systems of a crystal is described by the plastic flow equation, i.e.

$$\mathbf{l}^p = \sum_{\alpha}^{2N_{\text{sls}}} \dot{\gamma}^\alpha \mathbf{s}^\alpha \otimes \mathbf{n}^\alpha. \quad (2.80)$$

Recall that the rate of the plastic deformation can be expressed by means of the plastic velocity gradient

$$\mathbf{l}^p = \dot{\mathbf{F}}^p (\mathbf{F}^p)^{-1}. \quad (2.81)$$

Substituting Equation (2.80) into (2.81), one obtains a evolution equation for the plastic deformation gradient as

$$\dot{\mathbf{F}}^p = \left[\sum_{\alpha}^{2N_{\text{sls}}} \dot{\gamma}^\alpha \mathbf{s}^\alpha \otimes \mathbf{n}^\alpha \right] \mathbf{F}^p. \quad (2.82)$$

Plastic slip in a slip system occurs if the resolved shear stress reaches a critical limit. For convenience, the resolved shear stress τ^α of slip system α is expressed in terms of the Kirchhoff stress $\boldsymbol{\tau}$. The slip plane normal vector and the slip direction vector are defined on the intermediate configuration, while the Kirchhoff stress is defined in the current configuration. Therefore, the Kirchhoff stress has to be rotated back to the intermediate configuration, i.e.

$$\tau^\alpha = ((\mathbf{R}^e)^T \boldsymbol{\tau} \mathbf{R}^e) : (\mathbf{s}^\alpha \otimes \mathbf{n}^\alpha). \quad (2.83)$$

Furthermore, yield functions are introduced as a criterion that defines at which stress plastic slip occurs

$$f^\alpha(\tau^\alpha, \tau_y^\alpha) = \tau^\alpha - \tau_y^\alpha, \quad \alpha = 1, \dots, 2N_{\text{sls}}. \quad (2.84)$$

Herein τ_y^α specifies the critical shear stress of system α , i.e., the resistance of the crystal lattice against plastic sliding. By means of the yield function f the yield surface is given for every slip system α as

$$f^\alpha(\tau^\alpha, \tau_y^\alpha) = 0. \quad (2.85)$$

Plastic slip occurs if the stress state is on the yield surface. It is important to note, that the plastic multipliers $\dot{\gamma}^\alpha$ have to satisfy the Karush-Kuhn-Tucker (KKT) or complementary conditions

$$f^\alpha \leq 0, \quad \dot{\gamma}^\alpha \geq 0, \quad f^\alpha \dot{\gamma}^\alpha = 0, \quad (2.86)$$

for each $\alpha = 1, \dots, 2N_{\text{sls}}$. In Equation (2.84) the critical resolved shear stress is composed of an initial value τ_0^α and an increase due to hardening τ_h^α , i.e.

$$\tau_y^\alpha = \tau_0^\alpha + \tau_h^\alpha, \quad (2.87)$$

where the initial shear stress is a material constant. The hardening contribution τ_h^α is determined from the deformation history. It is a function of the plastic multipliers as well as the material and slip system-specific hardening coefficients. The latter quantities which are represented by the hardening matrix $h_{\alpha\beta}$. Eventually, the evolution of the τ_h is defined as

$$\dot{\tau}_h^\alpha = \sum_{\beta=1}^{2N_{\text{sls}}} h_{\alpha\beta} \dot{\gamma}^\beta, \quad \alpha = 1, \dots, 2N_{\text{sls}}. \quad (2.88)$$

Lastly, the reversible elastic behavior is specified by the Helmholtz free energy for neo-Hookean material, introduced in Equation (2.71). Since the plastic deformation is volume-preserving, it is convenient to use the decomposition of the deformation gradient, introduced in Section 2.1.2, and rewrite Equation (2.71) in terms of the elastic, isochoric left Cauchy-Green Tensor

$$\mathbf{B}_{\text{iso}}^e = \mathbf{F}_{\text{iso}}^e (\mathbf{F}_{\text{iso}}^e)^T = (J^e)^{-\frac{1}{3}} \mathbf{B}^e, \quad (2.89)$$

where

$$J^e = \det(\mathbf{F}^e) \quad \text{and} \quad \mathbf{F}_{\text{iso}}^e = (J^e)^{-\frac{1}{3}} \mathbf{F}^e. \quad (2.90)$$

Consequently, the free Helmholtz energy is stated as

$$\rho_0 \psi(\mathbf{B}_{\text{iso}}^e) = \frac{1}{2} G [\text{tr}(\mathbf{B}_{\text{iso}}^e) - 3] + \frac{1}{2} K [\ln(J^e)]^2. \quad (2.91)$$

By means of Equation (2.91) and (2.68) the Kirchhoff stress can be computed as

$$\boldsymbol{\tau} = 2\rho_0 \frac{\partial \psi}{\partial \mathbf{B}_{\text{iso}}^e} \mathbf{B}^e = G \text{dev}(\mathbf{B}_{\text{iso}}^e) + K [\ln(J^e)] \mathbf{I}. \quad (2.92)$$

In Equation (2.92) $\text{dev}(\mathbf{B}_{\text{iso}}^e)$ denotes the deviatoric part of the tensor $\mathbf{B}_{\text{iso}}^e$. The slip system tensor $(\mathbf{s}^\alpha \otimes \mathbf{n}^\alpha)$ is deviatoric, meaning $\text{tr}(\mathbf{s}^\alpha \otimes \mathbf{n}^\alpha) = 0$, by construction. Therefore, the product of the slip system tensor and the hydrostatic part of the Kirchhoff stress vanishes and the resolved shear stress for slip system α becomes

$$\begin{aligned}
 \tau^\alpha &= (G (\mathbf{R}^e)^T \text{dev}(\mathbf{B}_{\text{iso}}^e) \mathbf{R}^e) : (\mathbf{s}^\alpha \otimes \mathbf{n}^\alpha) \\
 &= (G (\mathbf{R}^e)^T \mathbf{B}_{\text{iso}}^e \mathbf{R}^e) : (\mathbf{s}^\alpha \otimes \mathbf{n}^\alpha) \\
 &= (G \mathbf{C}_{\text{iso}}^e) : (\mathbf{s}^\alpha \otimes \mathbf{n}^\alpha) \\
 &= (G (\mathbf{F}_{\text{iso}}^e)^T \mathbf{F}_{\text{iso}}^e) : (\mathbf{s}^\alpha \otimes \mathbf{n}^\alpha).
 \end{aligned} \tag{2.93}$$

For convenience, the quantities

$$\bar{\mathbf{s}}^\alpha = \mathbf{F}_{\text{iso}}^e \mathbf{s}^\alpha \quad \text{and} \quad \bar{\mathbf{n}}^\alpha = \mathbf{F}_{\text{iso}}^e \mathbf{n}^\alpha \tag{2.94}$$

are introduced, so that the resolved shear stresses can be stated in a simplified manner as

$$\tau^\alpha = G \bar{\mathbf{s}}^\alpha \cdot \bar{\mathbf{n}}^\alpha. \tag{2.95}$$

Box 2.1 summarizes the governing equations of the constitutive elastoplastic model of single crystals with a neo-Hookean material behavior for the elastic part.

(i) Multiplicative decomposition of \mathbf{F} :

$$\mathbf{F} = \mathbf{F}^e \mathbf{F}^p$$

(ii) Free Helmholtz energy:

$$\rho_0 \psi(\mathbf{B}_{\text{iso}}^e) = \frac{1}{2} G [\text{tr}(\mathbf{B}_{\text{iso}}^e) - 3] + \frac{1}{2} K [\ln(J^e)]^2$$

(iii) Hyperelastic law for the Kirchhoff stress:

$$\boldsymbol{\tau} = 2\rho_0 \frac{\partial \psi}{\partial \mathbf{B}_{\text{iso}}^e} \mathbf{B}^e = G \text{dev}(\mathbf{B}_{\text{iso}}^e) + K [\ln(J^e)] \mathbf{I}$$

(iv) Resolved shear stress:

$$\tau^\alpha = G (\mathbf{R}^e)^T \text{dev}(\mathbf{B}_{\text{iso}}^e) \mathbf{R}^e : (\mathbf{s}^\alpha \otimes \mathbf{n}^\alpha) = G \bar{\mathbf{s}}^\alpha \cdot \bar{\mathbf{n}}^\alpha$$

(v) Yield function:

$$f^\alpha(\tau^\alpha, \tau_y^\alpha) = \tau^\alpha - \tau_y^\alpha(\tau_h^\alpha)$$

(vi) Evolution equations for \mathbf{F}^p and τ_h^α :

$$\dot{\mathbf{F}}^p = \left[\sum_{\alpha=1}^{2N_{\text{sls}}} \dot{\gamma}^\alpha \mathbf{s}^\alpha \otimes \mathbf{n}^\alpha \right] \mathbf{F}^p$$

$$\dot{\tau}_h^\alpha = \sum_{\beta=1}^{2N_{\text{sls}}} h_{\alpha\beta} \dot{\gamma}^\beta$$

(vii) Loading/unloading criterions

$$f^\alpha \leq 0, \quad \dot{\gamma}^\alpha \geq 0, \quad f^\alpha \dot{\gamma}^\alpha = 0$$

for $\alpha = 1, \dots, 2N_{\text{sls}}$

BOX 2.1: General finite strain and anisotropic material model for crystal plasticity in single crystals with a neo-Hooke material model for the elastic part.

2.5 Weak Form and Linearization

The numerical methods for solving a problem in continuum mechanics discussed in the next chapter, are based on variational formulations. Furthermore, the continuum theory presented above contains nonlinearities due to geometric and material contributions. The standard approach is to replace the nonlinear problem by a sequence of linear problems, e.g., to apply Newton's method. This approach requires a consistent

linearization of all quantities of the nonlinear problem. This aspect is discussed in the following sections for the continuum theory described in this chapter.

2.5.1 Weak Form of Equilibrium

Consider a body \mathcal{B} , where the boundary can be presented as $\partial\mathcal{B} = \partial\mathcal{B}_u \cup \partial\mathcal{B}_\sigma$. An equivalent postulate to the balance of linear momentum is the so-called principle of virtual work. The principle of virtual work is also known as the weak form of equilibrium, because of its reduced regularity requirements. The weak form is derived from the local equilibrium Equation (2.41) by multiplying with a test function $\delta\mathbf{x}$, which should vanish on the displacement boundary of the continuum body $\partial\mathcal{B}_u$, on which Dirichlet boundary conditions are applied, $\delta\mathbf{x} = \{\delta\mathbf{x} \mid \delta\mathbf{x} = \mathbf{0} \text{ on } \partial\mathcal{B}_u\}$. The integration over the volume of \mathcal{B} yields

$$\int_{\mathcal{B}} \text{Div} \mathbf{P} \cdot \delta\mathbf{x} \, dV + \int_{\mathcal{B}} \rho_0 \mathbf{b} \cdot \delta\mathbf{x} \, dV = 0. \quad (2.96)$$

Using the divergence theorem and partial integration, together with the boundary condition on $\partial\mathcal{B}_u$, leads to the weak form

$$G(\mathbf{x}, \delta\mathbf{x}) = \int_{\mathcal{B}} \mathbf{P} : \text{Grad} \delta\mathbf{x} \, dV - \int_{\mathcal{B}} \rho_0 \mathbf{b} \cdot \delta\mathbf{x} \, dV - \int_{\partial\mathcal{B}_\sigma} \mathbf{t} \cdot \delta\mathbf{x} \, dA = 0, \quad (2.97)$$

where $\partial\mathcal{B}_\sigma$ denotes the boundary of the body \mathcal{B} , where Neumann boundary conditions are applied. The test function is also known as the virtual displacement and the gradient of $\delta\mathbf{x}$ can be viewed as a virtual variation of the deformation gradient $\delta\mathbf{F}$, which is defined as

$$\delta\mathbf{F} = \frac{d}{d\epsilon} [\mathbf{F}(\mathbf{x} + \epsilon \delta\mathbf{x})] |_{\epsilon=0}. \quad (2.98)$$

To derive the weak form in the spatial formulation, the Piola-Kirchhoff stress tensor has to be expressed in terms of the Cauchy stress tensor by Equation (2.30). In particular following relationships can be shown

$$\mathbf{P} : \text{Grad} \delta\mathbf{x} = J \boldsymbol{\sigma} \mathbf{F}^{-T} : \text{Grad} \delta\mathbf{x} = J \boldsymbol{\sigma} : \text{Grad} \delta\mathbf{x} \mathbf{F}^{-1} = J \boldsymbol{\sigma} : \text{grad} \delta\mathbf{x}. \quad (2.99)$$

With the known relations $dv = J dV$ and $\rho = \rho_0 J$ and Equation (2.99), the weak form in the current configuration is derived as

$$g(\mathbf{x}, \delta\mathbf{x}) = \int_{\mathcal{R}} \boldsymbol{\sigma} : \text{grad}_S \delta\mathbf{x} \, dv - \int_{\mathcal{R}} \rho \mathbf{b} \cdot \delta\mathbf{x} \, dv - \int_{\partial\mathcal{R}_\sigma} \mathbf{t} \cdot \delta\mathbf{x} \, da = 0. \quad (2.100)$$

In Equation (2.100), the symmetry of the Cauchy stress tensor allows to replace the spatial gradient of $\delta\mathbf{x}$ by its symmetric part. It is defined as

$$\text{grad}_S \delta\mathbf{x} = \frac{1}{2} (\text{grad} \delta\mathbf{x} + \text{grad}^T \delta\mathbf{x}). \quad (2.101)$$

2.5.2 Linearization

Let $\mathcal{F} = \mathcal{F}(\mathbf{x})$ be a scalar-valued, vector-valued or tensor-valued nonlinear and smooth function of \mathbf{x} . The linearization of \mathcal{F} is based on the Taylor series expansion, which can be expressed as

$$\mathcal{F}(\bar{\mathbf{x}} + \Delta\mathbf{x}) = \bar{\mathcal{F}} + \bar{D}\mathcal{F} \cdot \Delta\mathbf{x} + R, \quad (2.102)$$

where R is a small error with the property $\lim_{\Delta \mathbf{x} \rightarrow \mathbf{0}} \frac{R}{|\Delta \mathbf{x}|} \rightarrow 0$. The overbar on quantities and operators in this section illustrates the evaluation at point $\bar{\mathbf{x}}$. The linearization $L[\mathcal{F}]$ is defined as the linear part of \mathcal{F} at the point $\mathbf{x} = \bar{\mathbf{x}}$

$$L[\mathcal{F}]_{\mathbf{x}=\bar{\mathbf{x}}} = \bar{\mathcal{F}} + \bar{D}\mathcal{F} \cdot \Delta \mathbf{x}, \quad (2.103)$$

where the term $\Delta \mathcal{F} = \bar{D}\mathcal{F} \cdot \Delta \mathbf{x}$ can be interpreted as the directional derivative of \mathcal{F} , computed at $\bar{\mathbf{x}}$ in the direction of $\Delta \mathbf{x}$. This can be shown by means of the definition of the directional derivative and the chain rule:

$$\begin{aligned} \left. \frac{d}{d\epsilon} [\mathcal{F}(\bar{\mathbf{x}} + \epsilon \Delta \mathbf{x})] \right|_{\epsilon=0} &= \left[\frac{\partial \mathcal{F}(\bar{\mathbf{x}} + \epsilon \Delta \mathbf{x})}{\partial \mathbf{x}} \cdot \frac{\partial (\bar{\mathbf{x}} + \epsilon \Delta \mathbf{x})}{\partial \epsilon} \right]_{\epsilon=0} \\ &= \left. \frac{\partial \mathcal{F}}{\partial \mathbf{x}} \right|_{\mathbf{x}=\bar{\mathbf{x}}} \cdot \Delta \mathbf{x} = \bar{D}\mathcal{F} \cdot \Delta \mathbf{x} = \Delta \mathcal{F}. \end{aligned} \quad (2.104)$$

As said before, many approximation methods, like the FEM, are based on the weak form of the equilibrium, i.e. Equation (2.97) or Equation (2.100), in order to overcome high differentiability requirements. For the solution often an iterative scheme, based on the linearization is used. To derive the linearization of the weak form with respect to the reference configuration, Equation (2.103) is used to linearize $G(\mathbf{x}, \delta \mathbf{x})$ from Equation (2.97), i.e.

$$L[G]_{\mathbf{x}=\bar{\mathbf{x}}} = G(\bar{\mathbf{x}}, \delta \mathbf{x}) + \bar{D}G(\bar{\mathbf{x}}, \delta \mathbf{x}) \cdot \Delta \mathbf{x}, \quad (2.105)$$

where the first term is the weak form in the reference configuration, evaluated at $\mathbf{x} = \bar{\mathbf{x}}$ and $\bar{D}G(\bar{\mathbf{x}}, \delta \mathbf{x})$ can be interpreted as the tangent of the problem at $\bar{\mathbf{x}}$. By making use of $\mathbf{P} = \mathbf{F}\mathbf{S}$ the directional derivative of G in direction of $\Delta \mathbf{x}$ results in

$$\begin{aligned} \Delta G &= \bar{D}G(\bar{\mathbf{x}}, \delta \mathbf{x}) \cdot \Delta \mathbf{x} = \int_{\mathcal{B}} [\bar{D}\mathbf{P}(\bar{\mathbf{x}}) \cdot \Delta \mathbf{x}] : \text{Grad } \delta \mathbf{x} \, dV \\ &= \int_{\mathcal{B}} \{ \text{Grad } \Delta \mathbf{x} \bar{\mathbf{S}} + \bar{\mathbf{F}}[\bar{D}\mathbf{S}(\bar{\mathbf{x}}) \cdot \Delta \mathbf{x}] \} : \text{Grad } \delta \mathbf{x} \, dV. \end{aligned} \quad (2.106)$$

The directional derivative of the second Piola-Kirchhoff stress tensor often reads

$$\bar{D}\mathbf{S} \cdot \Delta \mathbf{x} = \bar{\mathbb{C}}[\Delta \bar{\mathbf{E}}]. \quad (2.107)$$

By using the equation above and considering the symmetry of \mathbf{S} , Equation (2.106) can be reformulated to

$$\begin{aligned} \Delta G &= \int_{\mathcal{B}} \{ \text{Grad } \Delta \mathbf{x} \bar{\mathbf{S}} + \bar{\mathbf{F}}\bar{\mathbb{C}}[\Delta \bar{\mathbf{E}}] \} : \text{Grad } \delta \mathbf{x} \, dV \\ &= \int_{\mathcal{B}} \{ \text{Grad } \Delta \mathbf{x} \bar{\mathbf{S}} : \text{Grad } \delta \mathbf{x} + \delta \bar{\mathbf{E}} : \bar{\mathbb{C}}[\Delta \bar{\mathbf{E}}] \} \, dV. \end{aligned} \quad (2.108)$$

The fourth order tensor $\bar{\mathbb{C}}$ depends on the constitutive model and is referred to as the material tangent. For a constitutive model that accounts for plastic deformation, as the model introduced in Section 2.4, the material tangent becomes a complex expression. Details on the computation of $\bar{\mathbb{C}}$ can be found in de Souza Neto et al. (2011). In order to express the linearization of the weak form in the actual configuration, Equation (2.108) has to be considered. The transformation of the first term to the

current configuration in (2.108) is

$$\text{Grad } \Delta \mathbf{x} \bar{\mathbf{S}} : \text{Grad } \delta \mathbf{x} = \overline{\text{grad}} \Delta \mathbf{x} J \bar{\boldsymbol{\sigma}} : \overline{\text{grad}} \delta \mathbf{x}, \quad (2.109)$$

and for the second term, one obtains

$$\delta \bar{\mathbf{E}} : \bar{\mathbf{C}} \Delta \bar{\mathbf{E}} = \overline{\text{grad}}_S \delta \mathbf{x} : \bar{\mathbf{c}} \overline{\text{grad}}_S \Delta \mathbf{x}, \quad (2.110)$$

where $\bar{\mathbf{c}}$ symbolizes the material tangent in spatial formulation. For the calculation of $\bar{\mathbf{c}}$ the index notation of tensors is used. Each index runs from 1 to 3, and the summation convention is adopted. The computation of $\bar{\mathbf{c}}$ is given by

$$\bar{c}_{ijkl} = \bar{F}_{iA} \bar{F}_{jB} \bar{F}_{kC} \bar{F}_{lD} \bar{\mathbf{C}}_{ABCD}. \quad (2.111)$$

Finally, the incremental Δg is required to solve the linearized form of (2.100)

$$L[g]_{\mathbf{x}=\bar{\mathbf{x}}} = g(\bar{\mathbf{x}}, \delta \mathbf{x}) + \bar{D}g(\bar{\mathbf{x}}, \delta \mathbf{x}) \cdot \Delta \mathbf{x} = g(\bar{\mathbf{x}}, \delta \mathbf{x}) + \Delta g(\bar{\mathbf{x}}, \delta \mathbf{x}) \quad (2.112)$$

and reads

$$\Delta g = \bar{D}g(\bar{\mathbf{x}}, \delta \mathbf{x}) \cdot \Delta \mathbf{x} = \int_{\mathcal{R}} (\overline{\text{grad}} \Delta \mathbf{x} \bar{\boldsymbol{\sigma}} : \overline{\text{grad}} \delta \mathbf{x} + \overline{\text{grad}}_S \delta \mathbf{x} : \hat{\mathbf{c}} \overline{\text{grad}}_S \Delta \mathbf{x}) \, dv, \quad (2.113)$$

with the introduction of $\hat{\mathbf{c}} = \frac{1}{J} \bar{\mathbf{c}}$.

Chapter 3

Numerical Discretization

The weak form, introduced in Chapter 2 is an integral equation, which cannot be solved directly for complex problems. Therefore, an approximation method, the Finite Element Method (FEM), is used. Within the FEM, the geometry and the associated fields, for example, the displacement, are approximated. The fundamentals of the FEM are introduced in the first part of this chapter. Furthermore, there are material-specific phenomena which require special treatment. These aspects, which are associated with the incompressible behavior of plastic material, are outlined in the second part. Finally, the chapter ends with the description of an update algorithm for the crystal plastic material at finite strains. The outlined descriptions mainly follow the text books of Wriggers (2006, 2008), Zienkiewicz and Taylor (2013) and Zienkiewicz et al. (2005), Simo and Hughes (1998) and de Souza Neto et al. (2011).

3.1 Fundamentals of the Finite Element Method

If the continuum mechanical equations are applied to a specific problem, a boundary value problem (BVP) results. It is composed of a kinematic theory, a constitutive model, and the equilibrium equations, introduced in Chapter 2. In order to solve the BVP, boundary conditions must also be added to these basic equations. In this work, the FEM is used to solve the resulting BVP. The idea of the FEM approximation is to divide the domain of interest, \mathcal{B} , into n_e subdomains, the finite elements:

$$\mathcal{B} \approx \mathcal{B}^h = \bigcup_{e=1}^{n_e} \Omega_e. \quad (3.1)$$

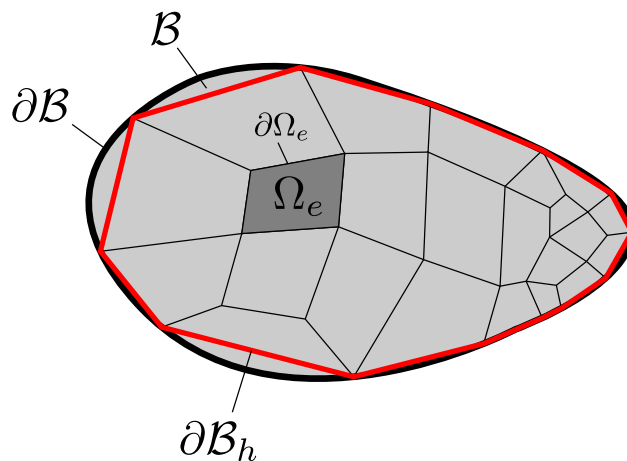


FIGURE 3.1: Finite Element discretization of body \mathcal{B} .

Figure 3.1 shows the discretization of a two-dimensional body \mathcal{B} . A discretized body \mathcal{B}^h with the boundary $\partial\mathcal{B}^h$ arises, where Ω_e is the configuration of a finite element with element boundary $\partial\Omega_e$. The field variable approximation for a finite element is given by

$$\mathbf{u}(\mathbf{X}, t) \approx \mathbf{u}^h(\mathbf{X}) = \sum_{I=1}^N N_I(\mathbf{X}) \mathbf{u}_I, \quad (3.2)$$

where the $N_I(\mathbf{X})$ are the shape functions which are defined on Ω_e and \mathbf{u}_I are the unknown nodal values of the field variable, e.g. the displacement field. In addition, the isoparametric concept is used. In this approach the geometry and the field variables are approximated by the same interpolation

$$\mathbf{X}_e^h = \sum_{I=1}^N N_I(\boldsymbol{\xi}) \mathbf{X}_I, \quad \mathbf{x}_e^h = \sum_{I=1}^N N_I(\boldsymbol{\xi}) \mathbf{x}_I, \quad \mathbf{u}_e^h = \sum_{I=1}^N N_I(\boldsymbol{\xi}) \mathbf{u}_I. \quad (3.3)$$

Hence, within the isoparametric concept a reference element Ω_{\square} with the element coordinates $\boldsymbol{\xi} = [\xi, \eta, \zeta]^T$ is mapped to a deformed element in the global coordinate system, compare Figure 3.2. Thereby, the matrix \mathbf{J}_e transforms the coordinates

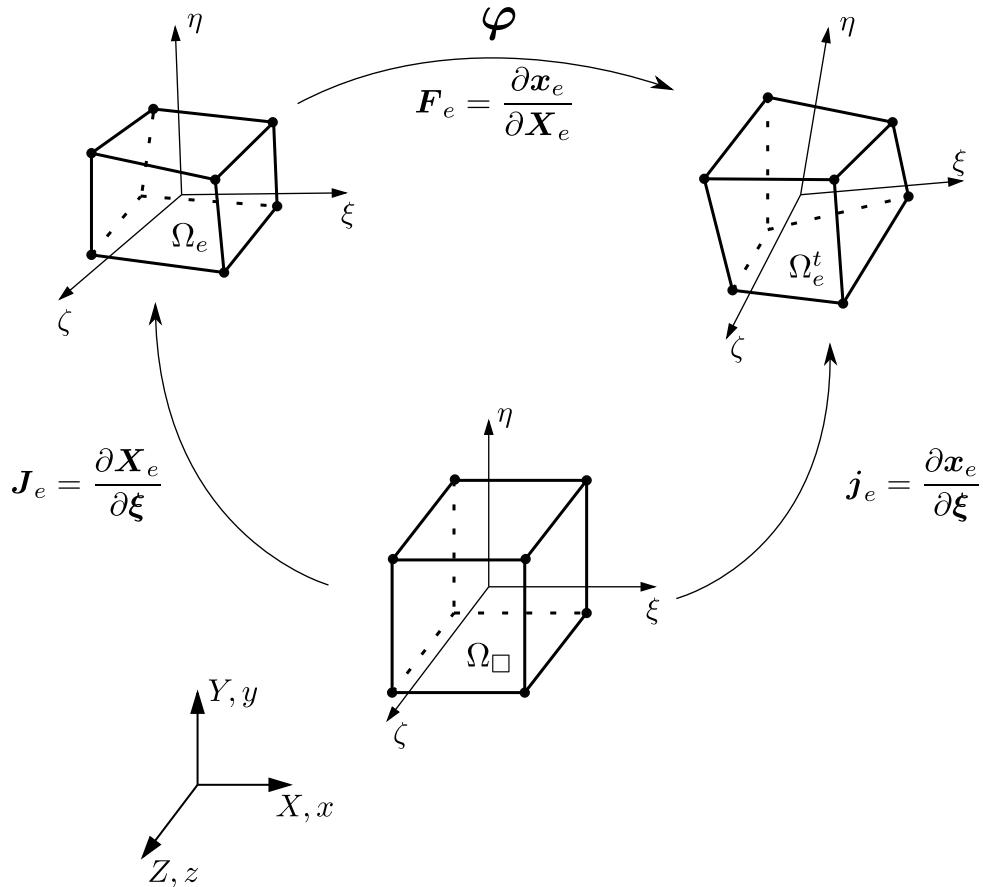


FIGURE 3.2: Isoparametric mapping of an 8-node three-dimensional element to the reference as well as the current configuration.

of the reference element to the reference configuration and the matrix \mathbf{j}_e maps the coordinates of the reference element to the deformed, current configuration. In this work, a three-dimensional 8-node brick element with linear shape functions, which is also shown in Figure 3.2, is used and consequently the number of nodes is $N = 8$.

The shape function of node I is given by

$$N_I = \frac{1}{2}(1 + \xi_I \xi) \frac{1}{2}(1 + \eta_I \eta) \frac{1}{2}(1 + \zeta_I \zeta). \quad (3.4)$$

With equations (3.3) and (3.4), the gradient operator in the reference and the current configuration can be expressed as

$$\begin{aligned} \text{Grad } \mathbf{u}_e &= \sum_{I=1}^N \mathbf{u}_I \otimes \text{Grad } N_I = \sum_{I=1}^N \mathbf{u}_I \otimes N_{I,\mathbf{X}} \quad \text{and} \\ \text{grad } \mathbf{u}_e &= \sum_{I=1}^N \mathbf{u}_I \otimes \text{grad } N_I = \sum_{I=1}^N \mathbf{u}_I \otimes N_{I,\mathbf{x}}. \end{aligned} \quad (3.5)$$

The gradient of the shape functions can again be calculated by using the transformation matrix \mathbf{J}_e or \mathbf{j}_e . For instance, the gradient of N_I in the current configuration can be expressed by

$$\begin{bmatrix} N_{I,\xi} \\ N_{I,\eta} \\ N_{I,\zeta} \end{bmatrix} = \begin{bmatrix} \frac{\partial x}{\partial \xi} & \frac{\partial y}{\partial \xi} & \frac{\partial z}{\partial \xi} \\ \frac{\partial x}{\partial \eta} & \frac{\partial y}{\partial \eta} & \frac{\partial z}{\partial \eta} \\ \frac{\partial x}{\partial \zeta} & \frac{\partial y}{\partial \zeta} & \frac{\partial z}{\partial \zeta} \end{bmatrix} \begin{bmatrix} N_{I,x} \\ N_{I,y} \\ N_{I,z} \end{bmatrix} = \mathbf{j}_e^T \begin{bmatrix} N_{I,x} \\ N_{I,y} \\ N_{I,z} \end{bmatrix}, \quad (3.6)$$

where \mathbf{j}_e can be computed by using Equation (3.3)₂. Finally, a relation for the deformation gradient and the determinant of the deformation gradient is obtained as

$$\mathbf{F}_e = \frac{\partial \mathbf{x}_e}{\partial \mathbf{X}_e} = \frac{\partial \mathbf{x}_e}{\partial \boldsymbol{\xi}} \frac{\partial \boldsymbol{\xi}}{\partial \mathbf{X}_e} = \mathbf{j}_e \mathbf{J}_e^{-1} \quad \text{and} \quad \det(\mathbf{F}_e) = \frac{\det(\mathbf{j}_e)}{\det(\mathbf{J}_e)}, \quad (3.7)$$

respectively. For the volume integrals, which arise for the chosen approximations, the relationship:

$$\int_{\mathcal{R}} (\dots) dv \approx \int_{\mathcal{R}^h} (\dots) dv = \bigcup_{e=1}^{n_e} \int_{\Omega_e} (\dots) dv = \bigcup_{e=1}^{n_e} \int_{\square} (\dots) \det(\mathbf{j}_e) d\square, \quad (3.8)$$

with

$$dv = \det(\mathbf{F}_e) \det(\mathbf{J}_e) d\square = \det(\mathbf{j}_e) d\square \quad (3.9)$$

holds. In order to specify the discretized weak form, a formulation for the symmetric part of the gradient of $\delta \mathbf{x}$, compare Equation (2.101), is needed. Within the isoparametric concept, the test function $\delta \mathbf{x}$ is approximated by the same interpolation as the geometry and field variables, see Equation (3.3). With

$$\begin{aligned} \text{grad } \delta \mathbf{x} &= \sum_{I=1}^N \delta \mathbf{x}_I \otimes \text{grad } N_I = \sum_{I=1}^N \delta \mathbf{x}_I \otimes N_{I,\mathbf{x}} \quad \text{and} \\ \text{grad}^T \delta \mathbf{x} &= \sum_{I=1}^N \text{grad } N_I \otimes \delta \mathbf{x}_I = \sum_{I=1}^N N_{I,\mathbf{x}} \otimes \delta \mathbf{x}_I \end{aligned} \quad (3.10)$$

follows

$$\text{grad}_S \delta \mathbf{x} = \frac{1}{2} \sum_{I=1}^N (\delta \mathbf{x}_I \otimes N_{I,\mathbf{x}} + N_{I,\mathbf{x}} \otimes \delta \mathbf{x}). \quad (3.11)$$

Due to the symmetry of the Cauchy stress tensor $\boldsymbol{\sigma}$ and $\text{grad}_S \delta \mathbf{x}$, the spatial symmetric gradient in Voigt notation, indicated by the underbar, is given by

$$\underline{\text{grad}}_S \delta \mathbf{x} = \sum_{I=1}^N \begin{bmatrix} N_{I,1} & 0 & 0 \\ 0 & N_{I,2} & 0 \\ 0 & 0 & N_{I,3} \\ N_{I,2} & N_{I,1} & 0 \\ 0 & N_{I,3} & N_{I,2} \\ N_{I,3} & 0 & N_{I,1} \end{bmatrix} \begin{bmatrix} (\delta \mathbf{x})_1 \\ (\delta \mathbf{x})_2 \\ (\delta \mathbf{x})_3 \end{bmatrix} = \sum_{I=1}^N \underline{\mathbf{B}}_I \delta \mathbf{x}_I, \quad (3.12)$$

and the Cauchy stress tensor can be expressed as

$$\underline{\boldsymbol{\sigma}} = \begin{bmatrix} \sigma_{11} \\ \sigma_{22} \\ \sigma_{33} \\ \sigma_{12} \\ \sigma_{23} \\ \sigma_{31} \end{bmatrix}. \quad (3.13)$$

Subsequently, the discretization of the first part of the weak form (2.100) can be formulated

$$\begin{aligned} \int_{\mathcal{R}} \text{grad}_S \delta \mathbf{x} : \boldsymbol{\sigma} \, dv &= \bigcup_{e=1}^{n_e} \int_{\Omega_e^t} (\underline{\text{grad}}_S \delta \mathbf{x})^T \underline{\boldsymbol{\sigma}} \, dv \\ &= \bigcup_{e=1}^{n_e} \sum_{I=1}^N \delta \mathbf{x}_I^T \int_{\Omega_e} \underline{\mathbf{B}}_I^T \underline{\boldsymbol{\sigma}} \, dv \\ &= \bigcup_{e=1}^{n_e} \sum_{I=1}^N \delta \mathbf{x}_I^T \underline{\mathbf{r}}_I^e(\mathbf{u}_e) = \delta \mathbf{x}^T \underline{\mathbf{r}}(\mathbf{u}), \end{aligned} \quad (3.14)$$

where $\underline{\mathbf{r}}_I^e$ and $\underline{\mathbf{r}}$ are called the element residual and the global residual, respectively. The second part of Equation (2.100), which includes the external loads, can be rewritten as

$$\int_{\mathcal{R}} \rho \mathbf{b} \cdot \delta \mathbf{x} \, dv + \int_{\partial \mathcal{R}_\sigma} \mathbf{t} \cdot \delta \mathbf{x} \, da = \bigcup_{e=1}^{n_e} \sum_{I=1}^N \delta \mathbf{x}_I^T \underline{\mathbf{P}}_I^e = \delta \mathbf{x}^T \underline{\mathbf{P}}. \quad (3.15)$$

Recalling, that the values of the virtual displacement $\delta \mathbf{x}$ are arbitrary except for the restrictions described in chapter 2, the system of nonlinear algebraic equations for the unknown displacement $\underline{\mathbf{u}}$ follows from Equation (3.14) and (3.15) as

$$\underline{\mathbf{g}}(\underline{\mathbf{u}}) = \underline{\mathbf{r}}(\underline{\mathbf{u}}) - \underline{\mathbf{P}} = \mathbf{0}. \quad (3.16)$$

For solving this system of nonlinear equations, a discretized form of the linearization $\Delta \mathbf{g}$, see Equation (2.113), is needed. With the discretizations

$$\overline{\text{grad}} \Delta \mathbf{u} = \sum_{J=1}^N \Delta \mathbf{u}_J \otimes N_{J,\mathbf{x}}, \quad \overline{\text{grad}} \delta \mathbf{x} = \sum_{I=1}^N \delta \mathbf{x}_I \otimes N_{I,\mathbf{x}}, \quad (3.17)$$

the first part of the discretized form of Δg can be expressed as

$$\int_{\mathcal{R}} (\overline{\text{grad}} \Delta \mathbf{u} \bar{\boldsymbol{\sigma}} : \overline{\text{grad}} \delta \mathbf{x}) \, dv = \bigcup_{e=1}^{n_e} \sum_{I=1}^N \sum_{J=1}^N \delta \mathbf{x}_I^T \left(\int_{\Omega_e^t} \bar{g}_{IJ} \mathbf{I} \, dv \right) \Delta \mathbf{u}_J, \quad (3.18)$$

with

$$\begin{aligned} \bar{g}_{IJ} &= [N_{I,1} \quad N_{I,2} \quad N_{I,3}] \begin{bmatrix} \bar{\sigma}_{11} & \bar{\sigma}_{12} & \bar{\sigma}_{13} \\ \bar{\sigma}_{21} & \bar{\sigma}_{22} & \bar{\sigma}_{23} \\ \bar{\sigma}_{31} & \bar{\sigma}_{32} & \bar{\sigma}_{33} \end{bmatrix} \begin{bmatrix} N_{J,1} \\ N_{J,2} \\ N_{J,3} \end{bmatrix} \\ &= (N_{I,\mathbf{x}})^T \cdot [\bar{\boldsymbol{\sigma}} N_{J,\mathbf{x}}]. \end{aligned} \quad (3.19)$$

The second term of Δg , with the matrix $\underline{\mathbf{B}}_J$ of Equation (3.12), is approximated by:

$$\int_{\mathcal{R}} (\overline{\text{grad}}_S \delta \mathbf{x} : \hat{\mathbb{c}} \overline{\text{grad}}_S \Delta \mathbf{u}) \, dv = \bigcup_{e=1}^{n_e} \sum_{I=1}^N \sum_{J=1}^N \delta \mathbf{x}_I^T \left(\int_{\Omega_e^t} \underline{\mathbf{B}}_I^T \hat{\mathbb{c}} \underline{\mathbf{B}}_J \, dv \right) \Delta \mathbf{u}_J. \quad (3.20)$$

In conclusion, Δg can be represented as

$$\Delta g = \bigcup_{e=1}^{n_e} \sum_{I=1}^N \sum_{J=1}^N \delta \mathbf{x}_I^T \mathbf{k}_{IJ}^e \Delta \mathbf{u}_J \quad (3.21)$$

with the tangential element stiffness matrix

$$\mathbf{k}_{IJ}^e = \int_{\Omega_e^t} (\bar{g}_{IJ} \mathbf{I} + \underline{\mathbf{B}}_I^T \hat{\mathbb{c}} \underline{\mathbf{B}}_J) \, dv. \quad (3.22)$$

By means of Equation (3.21), the nonlinear system of Equation (3.16) for the unknown displacement \mathbf{u} vector can be solved with an iterative solution scheme. In this work the Newton-Raphson scheme is used.

3.2 Extension for Incompressible Material

Due to the plastic incompressibility of the crystal plastic continuum model, as mentioned by Steinmann and Stein (1996), additional techniques compared to the standard FEM are necessary. It is known, that the performance of finite elements with linear shape functions, as presented in the section above, is very poor if a material formulation with nearly incompressible behavior is used. In such cases, volumetric locking occurs which leads to an overly stiff material behavior. There are several approaches to prevent volumetric locking. For example, higher order elements can be used, which means the usage of shape functions with quadratic or higher order. An alternative is the mixed u/p (displacement-pressure) formulation proposed by Sussman and Bathe (1987). The F-bar approach is another possibility to avoid volumetric locking. It was proposed by de Souza Neto et al. (1996) and is related to the B-bar procedure of Hughes (1980). The approach is chosen in this work because of its simplicity. It is based on the multiplicative split of the deformation gradient \mathbf{F} into an isochoric and a volumetric part. Remember that \mathbf{F} can be decomposed as

$$\mathbf{F} = \mathbf{F}_{\text{iso}} \mathbf{F}_V, \quad (3.23)$$

where

$$\mathbf{F}_{\text{iso}} = (\det \mathbf{F})^{-\frac{1}{3}} \mathbf{F} \quad \text{and} \quad \mathbf{F}_{\text{v}} = (\det \mathbf{F})^{\frac{1}{3}} \mathbf{I}. \quad (3.24)$$

The key idea of the F-bar method is to apply the isochoric/volumetric split to the standard deformation gradient \mathbf{F} , which is evaluated at every gauss point, as well as to the deformation gradient \mathbf{F}_0 , which is evaluated at the centroid of the element, i.e. $\boldsymbol{\xi} = \boldsymbol{\xi}_0$. The procedure is illustrated in Figure 3.3 for a three-dimensional 8-node brick element. With the split

$$\mathbf{F}_0 = (\mathbf{F}_0)_{\text{iso}}(\mathbf{F}_0)_{\text{v}}, \quad (3.25)$$

the F-bar deformation gradient is defined as the product of the isochoric component of \mathbf{F} and the volumetric part of \mathbf{F}_0 , i.e.

$$\bar{\mathbf{F}} = \mathbf{F}_{\text{iso}}(\mathbf{F}_0)_{\text{v}} = \left(\frac{\det \mathbf{F}_0}{\det \mathbf{F}} \right)^{\frac{1}{3}} \mathbf{F}. \quad (3.26)$$

The F-bar deformation gradient formulation for the 8-node brick element is obtained by simply replacing the standard deformation gradient \mathbf{F} by the modified deformation gradient $\bar{\mathbf{F}}$. Subsequently, the Cauchy stress is computed as

$$\boldsymbol{\sigma} = \boldsymbol{\sigma}(\bar{\mathbf{F}}). \quad (3.27)$$

Furthermore, it must be noted, that the F-bar approach requires the tangential stiffness matrix, Equation (3.22), to be adjusted. More details to the tangential stiffness matrix for the F-Bar approach can be found in de Souza Neto et al. (2011).

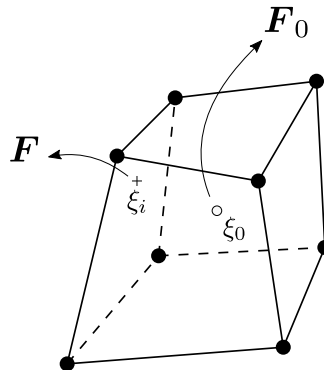


FIGURE 3.3: Evaluation of different deformation gradients for the F-bar procedure. (Own figure based on de Souza Neto et al. (2011))

3.3 Integration Algorithm for Crystal Plastic Material

The finite strain crystal plasticity material is a so-called path-dependent material and involves rate dependent constitutive equations, see Chapter 2. For this reason, an algorithm for the rate dependent constitutive equations is needed. The return mapping or predictor/corrector algorithm is a widely used state-update algorithm for elastoplastic material, which is also used within this work. The integration scheme is based on implicit time integration. The general form of such integration scheme is indicated in Figure (3.4), whereas the complete algorithm is described in the following paragraph.

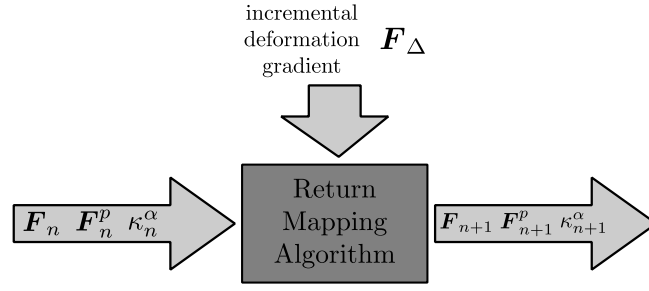


FIGURE 3.4: General elastoplastic update algorithm.

The return mapping algorithm is based on a two-step predictor-corrector scheme. Inside the predictor step an arbitrary, but kinematically permissible displacement is applied on a body. Assuming, that boundary conditions are set so that the body can deform, a so-called trial state arises. The yield surface indicates whether the computed trial stress state is inside or outside the elastic domain. If the stress state is inside the elastic domain no plastic slip occurs and all quantities of the next timestep are equal to the quantities in the trial state $(\cdot)_{n+1} = (\cdot)_{n+1}^{\text{trial}}$. However, if the trial stress state is outside the elastic domain, plastic slip occurs. In this case the plastic increments of the active slip systems have to be computed and a corrector step for the trial quantities is needed that brings the stress state back to an admissible state. The general return mapping algorithm is illustrated in Figure 3.5 and is explained in more detail in the following.

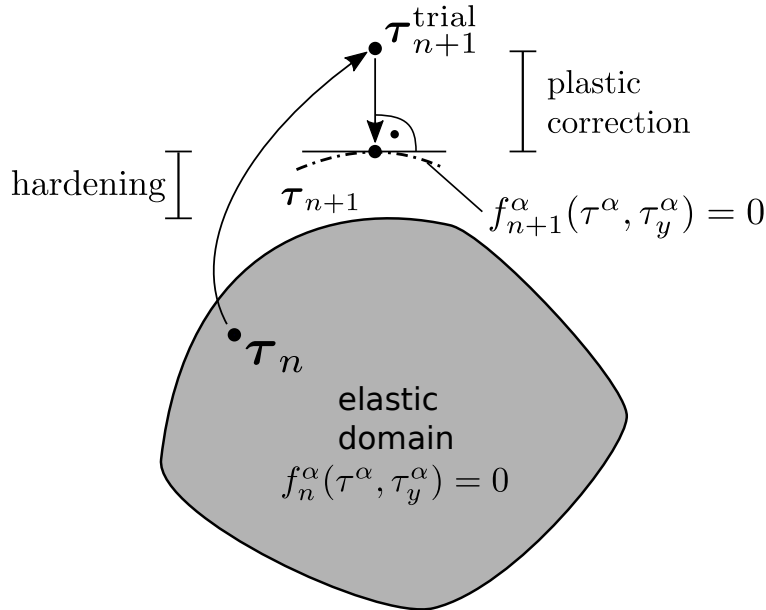


FIGURE 3.5: General return mapping scheme.

The elastic trial step

Considering the time interval $[t_n, t_{n+1}]$. With the incremental deformation gradient

$$\mathbf{F}_\Delta = \mathbf{I} + \text{grad}(\Delta \mathbf{u}), \quad (3.28)$$

the elastic trial deformation gradient is given by

$$\mathbf{F}_{n+1}^{e,\text{trial}} = \mathbf{F}_\Delta \mathbf{F}_n^e. \quad (3.29)$$

The resolved shear stress in slip system α of the trial state is computed according to (2.93), i.e.

$$\tau_{n+1}^{\alpha,\text{trial}} = G \left(\mathbf{F}_{n+1}^{e,\text{trial}} \right)^T \mathbf{F}_{n+1}^{e,\text{trial}} : (\mathbf{s}^\alpha \otimes \mathbf{n}^\alpha), \quad (3.30)$$

In Equation (3.30), G is the material specific shear modulus. Subsequently, the trial yield surface $f_{n+1}^{\alpha,\text{trial}}$ is used to check whether plastic slip occurs. If the trial state lies inside or on the yield surface, i.e. if

$$f_{n+1}^{\alpha,\text{trial}} = \tau_{n+1}^{\alpha,\text{trial}} - \tau_{y,n+1}^{\alpha,\text{trial}} \leq 0, \quad \text{for } \alpha = 1, \dots, N_{\text{sls}}, \quad (3.31)$$

for all N_{sls} slip systems, then the trial values correspond to the real values of the next step:

$$(\cdot)_{n+1} = (\cdot)_{n+1}^{\text{trial}}. \quad (3.32)$$

Otherwise, if $f_{n+1}^{\alpha,\text{trial}} > 0$ for any slip system α , plastic slip occurs and the second, plastic corrector step, which is described below, is applied.

The plastic corrector step

Starting point for the plastic corrector step, is the update Equation (2.82) for the plastic deformation gradient \mathbf{F}^p . By means of implicit time integration within the interval $[t_n, t_{n+1}]$ and the assumption, that $\dot{\gamma}^\alpha$ is constant within this time interval, the update formula leads to

$$\mathbf{F}_{n+1}^p = \exp \left(\sum_{\alpha \in \mathcal{A}} \Delta t \dot{\gamma}^\alpha \mathbf{s}^\alpha \otimes \mathbf{n}^\alpha \right) \mathbf{F}_n^p = \exp \left(\sum_{\alpha \in \mathcal{A}} \Delta \gamma^\alpha \mathbf{s}^\alpha \otimes \mathbf{n}^\alpha \right) \mathbf{F}_n^p, \quad (3.33)$$

where $\Delta \gamma^\alpha$ denotes the incremental plastic slip or plastic multiplier of slip system α and \mathcal{A} contains the set of active slip systems. In Equation (3.33) $\exp(\mathbf{A})$ denotes the tensor exponential function of an arbitrary tensor \mathbf{A} . For more details on the implicit time integration scheme and the tensor exponential function, see de Souza Neto et al. (2011). The determination of the set of active slip systems is a crucial aspect of the whole algorithm and therefore is described in detail in Section 4.1. It is convenient to reformulate the update Equation (3.33) in terms of the elastic deformation gradient. The corresponding update equation reads

$$\mathbf{F}_{n+1}^e = \mathbf{F}_{n+1}^{e,\text{trial}} \exp \left(- \sum_{\alpha \in \mathcal{A}} \Delta \gamma^\alpha \mathbf{s}^\alpha \otimes \mathbf{n}^\alpha \right). \quad (3.34)$$

For the computation of the plastic multipliers $\Delta \gamma^\alpha$, the following system of nonlinear equations have to be solved:

$$f^\alpha(\Delta \gamma) = \tau^\alpha(\mathbf{F}_{n+1}^e(\Delta \gamma)) - \tau_y^\alpha(\Delta \gamma) = 0, \quad \text{with } \alpha \in \mathcal{A}, \quad (3.35)$$

with the set of active slip systems \mathcal{A} and $\Delta \gamma = \{\Delta \gamma^\alpha | \alpha \in \mathcal{A}\}$. Equation (3.35) follows from the fact, that the KKT conditions, i.e.

$$f^\alpha \leq 0, \quad \Delta \gamma^\alpha \geq 0, \quad \Delta \gamma^\alpha f^\alpha = 0, \quad (3.36)$$

need to be fulfilled. The solution for $\Delta \gamma^\alpha$ must not violate the conditions (3.36). To solve the equation systems of Equation (3.35) with the Newton-Raphson scheme, the linearization of the equations is necessary. For a detailed description of the solution scheme and the linearization see also de Souza Neto et al. (2011). Finally, with

the computed plastic multipliers, the elastic deformation gradient is calculated by Equation (3.34). Together with Equation (2.92) one obtains the update equation of the Kirchhoff stress

$$\boldsymbol{\tau}_{n+1} = G \operatorname{dev}(\mathbf{F}_{\text{iso}}^e (\mathbf{F}_{\text{iso}}^e)^T) + K \ln(J^e) \mathbf{I}, \quad (3.37)$$

where

$$\mathbf{F}_{\text{iso}}^e = (\mathbf{F}_{\text{iso}}^e)_{n+1} \quad \text{and} \quad J^e = J_{n+1}^e = J_{n+1} = \det[\mathbf{F}_{n+1}] \quad (3.38)$$

The algorithm described above is summarized in Box 3.1.

(i) Given the incremental deformation gradient $\mathbf{F}_\Delta = \mathbf{I} + \operatorname{grad}(\Delta \mathbf{u})$.
Compute the elastic trial state:

$$\mathbf{F}_{n+1}^{e,\text{trial}} = \mathbf{F}_\Delta \mathbf{F}_n^e$$

(ii) Perform the isochoric/volumetric decomposition:

$$J = \det(\mathbf{F}_{n+1}), \quad \mathbf{F}_{\text{iso}}^{e,\text{trial}} = J^{-\frac{1}{3}} \mathbf{F}_{n+1}^{e,\text{trial}}$$

(iii) Compute the elastic trial resolved Schmidt stress:

$$\bar{\mathbf{s}}^{\alpha,\text{trial}} = \mathbf{F}_{\text{iso}}^{e,\text{trial}} \mathbf{s}^\alpha, \quad \bar{\mathbf{n}}^{\alpha,\text{trial}} = \mathbf{F}_{\text{iso}}^{e,\text{trial}} \mathbf{n}^\alpha$$

$$\tau_{n+1}^{\alpha,\text{trial}} = G \bar{\mathbf{s}}^{\alpha,\text{trial}} \cdot \bar{\mathbf{n}}^{\alpha,\text{trial}}$$

for $\alpha = 1, \dots, N_{\text{sls}}$

(iv) Perform consistency check:

IF $f^{\alpha,\text{trial}} = \tau_{n+1}^{\alpha,\text{trial}} - \tau_y^{\alpha,\text{trial}} \leq 0$ THEN
 set $(\cdot)_{n+1} = (\cdot)_{n+1}^{\text{trial}}$ and GOTO (v)
ELSE
 Return mapping:
 1.) Choose a procedure to determine
 the set of active slip systems (see Section 4.1)
 2.) Calculate $\Delta\gamma^\alpha$ for active slip systems
 3.) Update $\mathbf{F}_{\text{iso}}^e$

(v) Update \mathbf{F}_{n+1}^e and stress tensor:

$$\mathbf{F}_{n+1}^e = J^{\frac{1}{3}} \mathbf{F}_{\text{iso}}^e$$

$$\mathbf{B}_{\text{iso}}^e = \mathbf{F}_{\text{iso}}^e (\mathbf{F}_{\text{iso}}^e)^T$$

$$\boldsymbol{\tau}_{n+1} = G \operatorname{dev}(\mathbf{B}_{\text{iso}}^e) + K \ln(J_{n+1}) \mathbf{I}$$

BOX 3.1: General elastic predictor/corrector algorithm for finite strain crystal plasticity.

Chapter 4

Implementation Details

In addition to the implementation by means of the FEM, there are another crucial implementation details. On the one hand, details regarding the material model, e.g., the determination of the active slip systems or the properties of the hexagonal close-packed crystal structure, are explained. On the other hand, the concept for the material separation, which is required for the micro-cutting process, is presented. Generally, methods of parallelization are used in the implementation. For the algorithm of assembling the global stiffness matrix OpenMP[®] is used for parallelization, for more information see OpenMP[®] ARB (2020). The parallel Intel[®] MKL PARDISO is used to solve the equation system. For further information about the PARDISO it is referred to the literature; see De Coninck et al. (2016), Kourounis et al. (2018), and Verbosio et al. (2017). More information about the Intel[®] MKL PARDISO can be found in Intel[®] Corporation (2020).

4.1 Determination of Active Slip Systems

As denoted in several parts of the literature, e.g., de Souza Neto et al. (2011), the determination of the set of active slip systems is a crucial part of the whole return mapping algorithm of crystal plastic material. Since there is a known weakness of the standard algorithm, an alternative Algorithm based on the Fischer-Burmeister equations is introduced besides the standard algorithm.

Determination by means of the yield function

The algorithm for the determination of active slip systems, which is widely used in the literature, is based on the Karush-Kuhn-Tucker (KKT) conditions, Equation (3.36). In the following this algorithm is called the standard algorithm and is used for example in Miehe (1996b), the ultimate algorithm of Borja and Wren (1993) and Borja (2013) or Cuitiño and Ortiz (1993). In the standard algorithm the yield function delivers the first set of active slip systems \mathcal{A}^1 . In the next step the system of nonlinear equations (3.35) are solved for the unknown $\Delta\gamma^\alpha$ with $\alpha \in \mathcal{A}^1$. Then the solution is checked, and negative $\Delta\gamma^k$ are set to zero, and the yield function is rechecked. This algorithm is done until all plastic slip increments are greater zero for the active set \mathcal{A}^k in the k -th iteration and the yield function is less than zero for all slip systems. Box 4.1 shows the whole algorithm.

- (i) Yield function delivers first active set:
 - $k = 1$
 - $\mathcal{A}^k = \{\alpha | f_{n+1}^{\alpha, \text{trial}} > 0\}$
 - (ii) Calculation of $\Delta\gamma^\alpha$ for $\alpha \in \mathcal{A}^k$ by solving system of nonlinear equations:
 - $f_{n+1}^\alpha(\Delta\gamma) = \tau_{n+1}^\alpha(\Delta\gamma_{n+1}^\alpha) - \tau_y^\alpha(\Delta\gamma_{n+1}^\alpha) = 0$
 - (iii) Check solution:
 - IF $\Delta\gamma^\alpha < 0$, THEN $\Delta\gamma^\alpha = 0$
 - (iv) Check yield function and build new set:
 - Calculate $f_{n+1}^\alpha(\Delta\gamma^\alpha) \forall \alpha$
 - IF $f_{n+1}^\alpha \leq 0 \forall \alpha$: STOP
 - ELSE $k = k + 1$; $\mathcal{A}^k = \{\alpha | f_{n+1}^\alpha > 0 \vee \Delta\gamma^\alpha > 0\}$
and GOTO (ii)

Box 4.1: Algorithm for determination of active slip systems based on the yield function and the KKT conditions.

Determination by means of the Fischer-Burmeister function

The second, alternative determination algorithm, bases on a special function, which was proposed by Fischer (1992). This function is often called the Fischer-Burmeister (FB) function, see Equation (4.1). The FB function is used for several problems in mechanics, for example, Bartel et al. (2019) used the function for a rate-dependent model for ferroelectrics. Also, in contact mechanics, the FB function is used, see Acary et al. (2018). The function is used in Akpama et al. (2016) for the determination of the active slip system in body-centered crystals, like iron. In Bischof et al. (2017), the FB function is finally adapted to the hexagonal close-packed crystal structure, like titanium or magnesium and can be expressed as

$$\varphi^\alpha = \sqrt{(f_{n+1}^\alpha)^2 + (\Delta\gamma_{n+1}^\alpha)^2} + f_{n+1}^\alpha - \Delta\gamma_{n+1}^\alpha = 0. \quad (4.1)$$

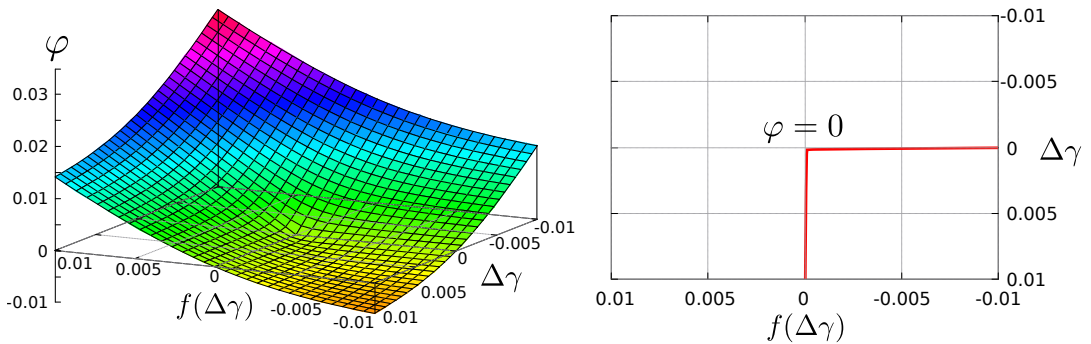


FIGURE 4.1: Contourplot and roots of the FB function.

The basic idea of the FB Function is to transform the KKT conditions into an equivalent system of nonlinear equations φ^α . The advantage is the semi-smoothness of the function. The roots correspond to the KKT conditions. A three-dimensional function plot and a plot of the roots of the FB function is shown in Figure 4.1. On the right side, it can be seen that for the solution of the FB Function $\varphi = 0$, the KKT conditions can be found again. For $f(\Delta\gamma) = 0$ the plastic increment is $\Delta\gamma \geq 0$ and in turn for $\Delta\gamma = 0$ the yield function is $f(\Delta\gamma) \leq 0$. In comparison to the determination explained in the section above, the set of active slip systems \mathcal{A} always contains all slip systems. The final active set of slip systems is determined implicitly by solving the system of equations φ^α for all slip systems. The special form of the equation results in $\gamma^\alpha > 0$ for active and $\gamma^\alpha = 0$ for non-active slip systems. The algorithm is summarized in Box 4.2.

(i) Yield function identifies plastic step:

- IF $f_{n+1}^{\alpha, \text{trial}} > 0$ for any $\alpha : \mathcal{A} = \{\alpha | \alpha = 1, \dots, 2N_{\text{sls}}\}$

(ii) Solve system of FB functions $\forall \alpha \in \mathcal{A}$:

- $\varphi^\alpha = \sqrt{(f_{n+1}^\alpha)^2 + (\Delta\gamma_{n+1}^\alpha)^2} + f_{n+1}^\alpha - \Delta\gamma_{n+1}^\alpha = 0$

(iii) Implicit determination of the set of active slip systems:

- $\mathcal{A} = \{\alpha | \Delta\gamma^\alpha > 0\}$

Box 4.2: Algorithm for determination of active slip systems based on the FB function.

4.2 Properties of the Hexagonal Close-Packed Crystal Structure and Hardening Mechanisms

In this work, the material of commercially pure (cp-) titanium is taken into account. The material cp-titanium consists of the α -titanium phase, and the hexagonal-closed packed (hcp) crystal structure of the α -phase significantly influences the deformation behavior.

Slip systems of hcp crystals

A plastic slip occurs in the various slip systems of the hcp unit cell. Though, a slip system is the totality of a slip plane and its slip direction. The main slip systems are shown in Figure 4.2. The basal slip systems, shown in blue, consisting of one slip plane and three slip directions. The prismatic slip systems are displayed in red and contain three slip planes with one slip direction each. Finally, the pyramidal slip systems, indicated in green, are counted as main slip systems. They contain six slip planes, each with one slip direction.

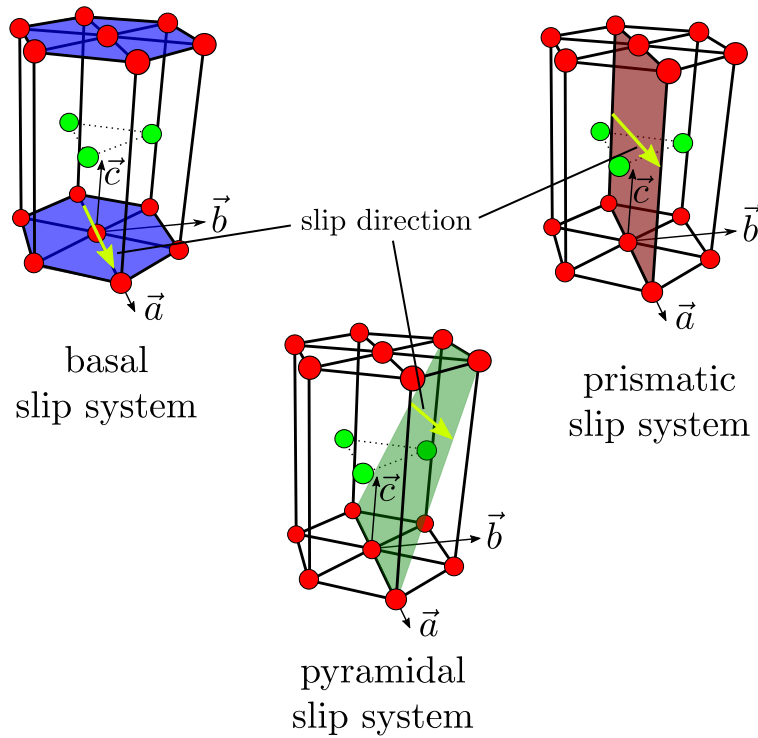


FIGURE 4.2: Main slip systems of the hcp unit cell.

The 12 main slip systems are not independent. Especially, the plastic deformation due to the pyramidal slip systems can be reproduced by a combined slip of the basal and prismatic slip systems. This leads to six independent main slip systems and the pyramidal slip systems and their influence are neglected for the material model. In cp-titanium and several titanium alloys, there is a presence of another slip direction observed. The often called $\langle c+a \rangle$ type slip system is illustrated in Figure 4.3. With the $\langle c+a \rangle$ type slip systems, there are another six slip systems. As described in Lütjering and Williams (2013), the percentage of grain deformation due to the $\langle c+a \rangle$ slip systems is meager, because of the much higher critical shear stress to activate this type. Therefore, the influence of the $\langle c+a \rangle$ type slip systems is also neglected, if nothing else is mentioned.

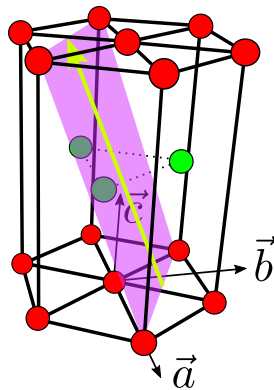


FIGURE 4.3: $\langle c+a \rangle$ type slip system.

Hardening mechanisms

With an increasing plastic slip, the resistance against plastic deformation is increasing. This physical phenomenon, known as hardening, is quite complex. The general approach to recognize hardening in the material model, proposed by Asaro and Needleman (1985), is already proposed in Equation (2.88). Now, different approaches for the hardening matrix $h^{\alpha\beta}$ will be discussed. There are two dominant hardening mechanisms, isotropic and latent hardening. On the one hand, isotropic hardening means that the plastic deformation of a slip system β has no effect on the hardening of another the slip system α . In contrast, Peirce et al. (1983) has observed, that there is an influence of the plastic slip of other slip systems β on a specific slip system α , which is called latent hardening. A general approach for $h^{\alpha\beta}$ is given by the following equation (with no sum on β)

$$h^{\alpha\beta} = q^{\alpha\beta} h^\beta(\gamma), \quad (4.2)$$

where $q^{\alpha\beta}$ contains the isotropic and latent hardening coefficients. For the pure isotropic case follows

$$\begin{aligned} q^{\alpha\beta} &= 1 & \text{for } \alpha = \beta, \\ q^{\alpha\beta} &= 0 & \text{for } \alpha \neq \beta, \\ h^\beta(\gamma) &= h_0^\beta, \end{aligned} \quad (4.3)$$

with the slip system specific hardening module h_0 and the accumulated slip

$$\gamma = \sum_{\alpha}^{2N_{\text{sls}}} \int \dot{\gamma}^{\alpha} dt. \quad (4.4)$$

Other popular approaches, which also contain latent hardening, are proposed by Asaro (1983) or Brown et al. (1989). While Brown et al. (1989) uses unknown parameters, which can only be obtained through the fitting of experimental data, Bassani and Wu (1991) shows that the approach of Asaro is inconsistent to experimental observations and published an own complicated relationship, based on this approach, but with the disadvantage of many unknown material constants. Another possibility is shown by Hama et al. (2016). They propose a linear hardening and an approach for the Voce hardening. Both with material-specific latent hardening matrix $q^{\alpha\beta}$, compare to Equation (4.2). The linear hardening and the Voce hardening are described by the following equations

- linear hardening: $h^\beta(\gamma) = h_0^\beta$,
 - Voce hardening: $h^\beta(\gamma) = h_0^\beta \left(1 - \frac{\tau_0^\beta}{\tau_\infty^\beta} \right) \exp \left(-\frac{h_0^\beta \gamma}{\tau_\infty^\beta} \right)$,
- (4.5)

where τ_∞^β is the material and slip system specific saturation stress and τ_0^β the initial yield stress. In Hama et al. (2016) the approach 4.5 is identified to describe the hardening behaviour of titanium.

4.3 Material Separation

For the simulation of micromachining processes, material separation has to be modeled for the chip formation. In general, material separation is modeled by deactivating the relevant element of the mesh in the separation zone. That means, in the context

of FEM, the element has no more contribution to the global residual and the global stiffness matrix. In order to prevent instabilities from one time step to the next due to many element deletions, the stiffness proportion of the respective elements is reduced stepwise. The Young's modulus is reduced in three steps to 10% of the original value. Then the element is deleted, or the stiffness is set to 0. Finding appropriate criteria for separation is a difficult task. In this work, two different approaches are used. The first one is a purely geometrical approach, which means, if the tip of the tool is inside an element, the element is deactivated, see Figure 4.4. The second approach is taken

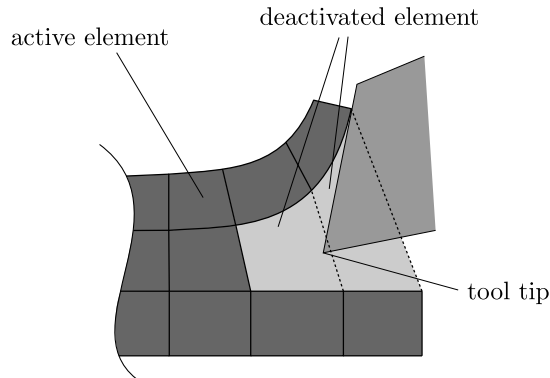


FIGURE 4.4: Geometrical separation criterion.

from damage mechanics. Thereby, an indicator D is introduced, which is used by de Geus et al. (2016) for the prediction of ductile fracture initiation. The approach is using the damage indicator of Johnson and Cook (1985) and is based on the equivalent plastic strain rate $\dot{\varepsilon}_{pl}$:

$$D = \int_0^t \frac{\dot{\varepsilon}_{pl}}{\varepsilon_c(\eta)} d\tau, \quad (4.6)$$

where ε_c is the material dependent critical strain, which depends on the local stress triaxiality η as follows

$$\varepsilon_c = A \exp(-B \eta) + \varepsilon_{pc}. \quad (4.7)$$

In the equation above, A, B , and the critical plastic strain ε_{pc} are material parameters. The stress triaxiality is the ratio of hydrostatic shear stress τ_m and equivalent shear stress τ_{eq}

$$\eta = \frac{\tau_m}{\tau_{eq}}. \quad (4.8)$$

Material failure and thus the deactivation of elements occurs, if the indicator D reaches a critical value D_c .

Chapter 5

Validation Examples

The material model and the concepts presented in the previous chapters are implemented in a numerical framework. The following simple examples now serve to validate or compare these concepts in detail.

5.1 Validation of the Material Model

In the following two examples, the implementation of the crystal plastic material model is evaluated, and it is shown that the model exhibits the expected behavior. Therefore, the crystal plastic material model with isotropic hardening is implemented. First, the standard active slip determination algorithm based on the KKT conditions is used, and the number of slip systems is reduced to two slip systems. Since the slip directions are mirrored, this results in a total number of four slip systems. With the reduced number, the plastic deformation along the slip directions can be better recognized. As an example, a simple tensile test is carried out, whereby the lower edge is fixed. At the upper edge, the displacement of u_0 in y -direction is applied. It is a three-dimensional simulation, but the displacement in z -direction is omitted and only deformations in x - and y -direction are considered. The sample is modeled as a single crystal, and two different orientations for the slip systems are tested. A symmetrical orientation, in which the slip direction differs by 60° , starting from the horizontal. And an asymmetric orientation, where the angle between the slip direction \mathbf{s}_1 and the horizontal is 75° and the angle between the slip directions \mathbf{s}_1 and \mathbf{s}_2 is 60° . Furthermore, three differently sized FEM meshes are used. The smallest mesh has $10 \times 30 \times 1$ elements, the medium-sized FEM mesh uses $20 \times 60 \times 1$ elements and the large mesh consists of $30 \times 90 \times 1$ elements. For this and all other simulations of this work, three-dimensional 8-node brick elements are used. The simulation setup with the mentioned boundary conditions and the coarsest mesh is shown in Figure 5.1. The right side of Figure 5.1 illustrates the symmetrical and asymmetrical slip system orientation. If not stated differently, the following exemplary material data are used for all examples of this chapter:

$$\begin{aligned} \text{Youngs Modulus } E &= 115 \text{ GPa,} \\ \text{Poisson Number } \nu &= 0.3, \\ \text{Initial Yield Stress } \tau_0 &= 0.3 \text{ GPa,} \\ \text{Hardening Modulus } h_0 &= 1 \text{ GPa,} \\ \text{Length unit } L &= 1 \text{ mm.} \end{aligned}$$

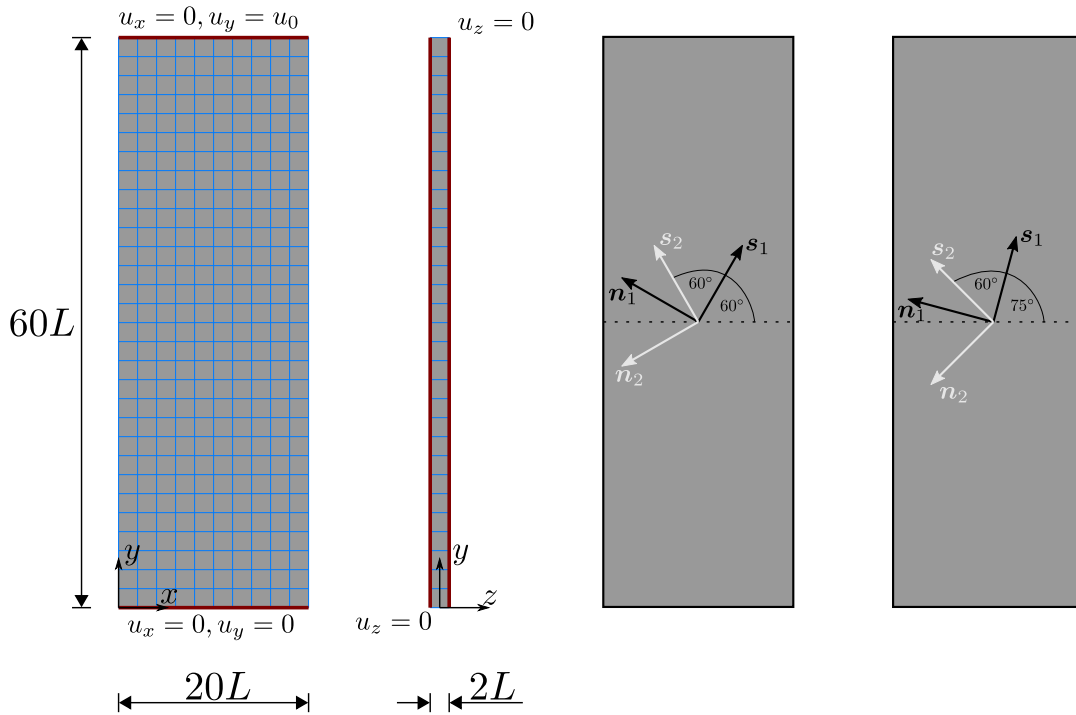


FIGURE 5.1: Geometry, boundary conditions and mesh with $10 \times 30 \times 1$ elements (left) and symmetric and asymmetric orientation of the slip systems (right) for the tensile test of the rectangular strip.

Figure 5.2 shows the comparison of the results of the mesh with $30 \times 90 \times 1$ elements for the symmetric example on the left side and the asymmetric example on the right side. The contour indicates the distribution of the plastic deformation and shows the norm of the plastic deformation gradient minus the identity tensor $\|\mathbf{F}^p - \mathbf{I}\|$.

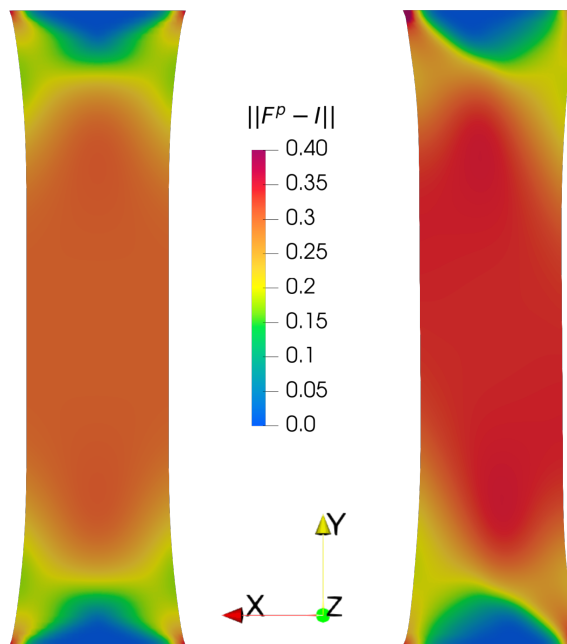


FIGURE 5.2: Deformed shape of the rectangular strip. Symmetrical example (left) and asymmetrical example (right).

For the symmetric example, the plastic deformation starts in the first and last third of the sample, which are areas with the highest load. Plastic slip occurs in all slip systems, and the plastic deformation spreads symmetrically over the strip. In contrast, the plastic slip in the second example occurs preferred in slip system 1 and its mirrored system and weaker in slip system 2 and its mirrored system. Figure 5.3 shows the force-displacement diagram for both examples and different mesh sizes. It can be seen that the plastic deformation begins earlier with asymmetric orientation than with symmetric orientation of the slip systems. In addition, it can be seen that the results for meshes of different sizes do not differ significantly from each other. The difference between the coarsest mesh and the middle mesh is still clearly visible but the results of the medium mesh and the finest mesh are very well matched.

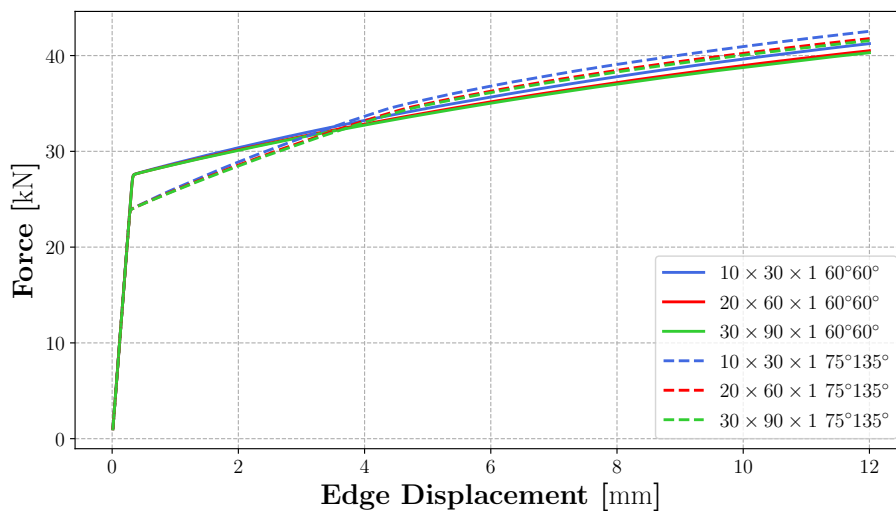


FIGURE 5.3: Force-displacement diagram for the tensile test with two slip systems to validate the crystal plastic material model.

5.2 Determination of Active Slip Systems

As already mentioned in Section 4.1, the determination of the active slip systems is an essential part of the crystal plastic material model. Since the slip systems and with them, the slip directions are not independent of each other, the selection is not unique. The standard algorithm based on the KKT conditions introduced in the previous chapter has known weaknesses. For this reason, another algorithm with an implicit determination based on the FB equation is also introduced and should be compared with the standard algorithm in regards to stability. Therefore, a tensile test is performed on a perforated disc. For this simulation, all main slip systems of the hcp unit cell are implemented. The disc is modeled as a single crystal, the unit cell is rotated by an angle $\Phi = 10^\circ$. The displacement $u_x = 0.6L$ at the right edge of the disc is applied linearly in 10 time steps. The meshing and the simulation setup is shown in Figure 5.4. The material constants and hardening mechanism remain the same as in the previous simulations. First of all, the standard algorithm leads to an abortion of the simulation, while the simulation with the FB algorithm is successfully completed. The details of the active slip systems during the simulation progress are listed in Table 5.1. It can be seen that the load in the first time step is too low to cause plastic deformation. In the second time step, both algorithms identify the same active

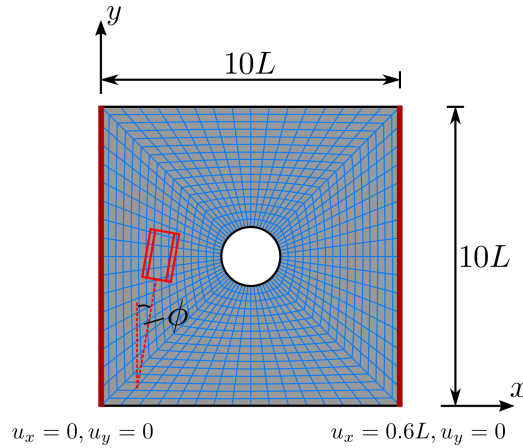


FIGURE 5.4: Simulation setup for the perforated disc.

slip systems 2, 6, and 10. But from the third time step on, the results differ. The standard algorithm jumps between different active sets, but does not converge and finally leads to an abortion. In contrast, the FB algorithm always uniquely identifies one set of active slip systems per time step and runs successfully until the end of the simulation. The upper two illustrations of Figure 5.5 show the distribution of the plastic deformation for both determination algorithms after the second time step whereby the results do not show significant differences. The lower illustration of Figure 5.5 shows the deformed shape and the distribution of the plastic deformation after the successful termination of the simulation with the FB algorithm. It should be noted that the FB algorithm requires a higher computing time compared to the algorithm based on KKT. On the one hand, all slip systems are regarded as potentially active, which has an influence on the size of the equation system to be solved. In addition, a line search algorithm is necessary in every time step, so that the FB algorithm converges against a sufficiently small error. But the FB algorithm proves to be robust compared to the KKT algorithm.

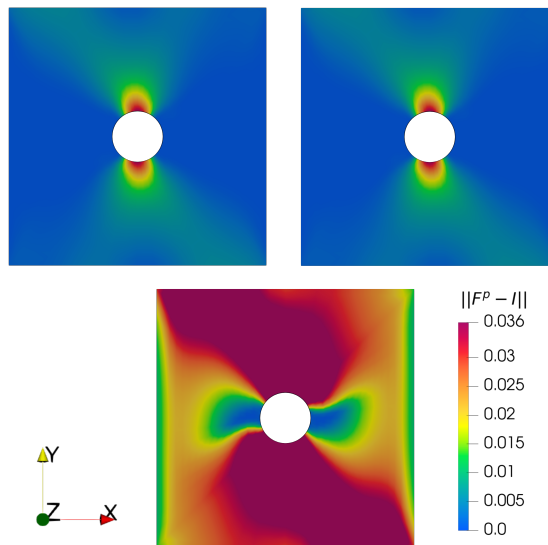


FIGURE 5.5: Deformed shape of perforated disc after second time step with the determination of the active slip systems based on the KKT conditions (top left), based on the FB function (top right) and after successful simulation based on FB algorithm (bottom).

TABLE 5.1: Comparison of the active slip systems for the two determination algorithms for the simulation of the perforated disc.

time step	KKT algorithm		FB algorithm	
	number of active slip systems	active slip systems	number of active slip systems	active slip systems
1	0	elastic step	0	elastic step
2	3	2, 6, 10	3	2, 6, 10
3	5	1, 2, 3, 6, 10	4	1, 2, 6, 10
	3	2, 6, 10		
	5	1, 2, 6, 9, 10		
	3	1, 6, 10		
	no convergence			
4			4	1, 2, 6, 10
5			4	1, 2, 6, 10
6			4	1, 2, 6, 10
7			4	1, 2, 6, 10
8			4	1, 2, 6, 10
9			5	1, 2, 3, 6, 10
10			5	1, 2, 3, 6, 10

5.3 F-Bar Implementation

As already described in Section 3.2, the volume-preserving plastic deformation leads to so-called volumetric locking, which results in a stiffened material behavior. In this work, the F-Bar approach is used to prevent these locking effects. To show this behavior, another tensile test on a notched plate, see Figure 5.6, is performed. The sample is modeled as a single crystal, the lower edge is fixed, and displacement to the upper edge is applied. Furthermore, it is a three-dimensional simulation, with one element of length $1L$ in z -direction and the displacement into the z -direction of all nodes is blocked. The total displacement of the upper edge is $u_0 = 3L$. For the crystal plastic material model, the main slip systems of cp-titanium are considered. The material data, which are used for this example, are published for cp-titanium by Hama et al. (2016). The material data and the crystal orientation are also shown in Table 5.2.

TABLE 5.2: Material parameters for the F-Bar simulation.

	Youngs Modulus [GPa]	Poisson's ratio [-]	τ_0 [MPa]	h_0 [MPa]	\vec{a}	\vec{b}
	105	0.34			$\begin{bmatrix} -0.044 \\ 0.075 \\ 0.9962 \end{bmatrix}$	$\begin{bmatrix} 0.866 \\ 0.5 \\ 0.0 \end{bmatrix}$
basal			133	1950		
prismatic			62	1050		

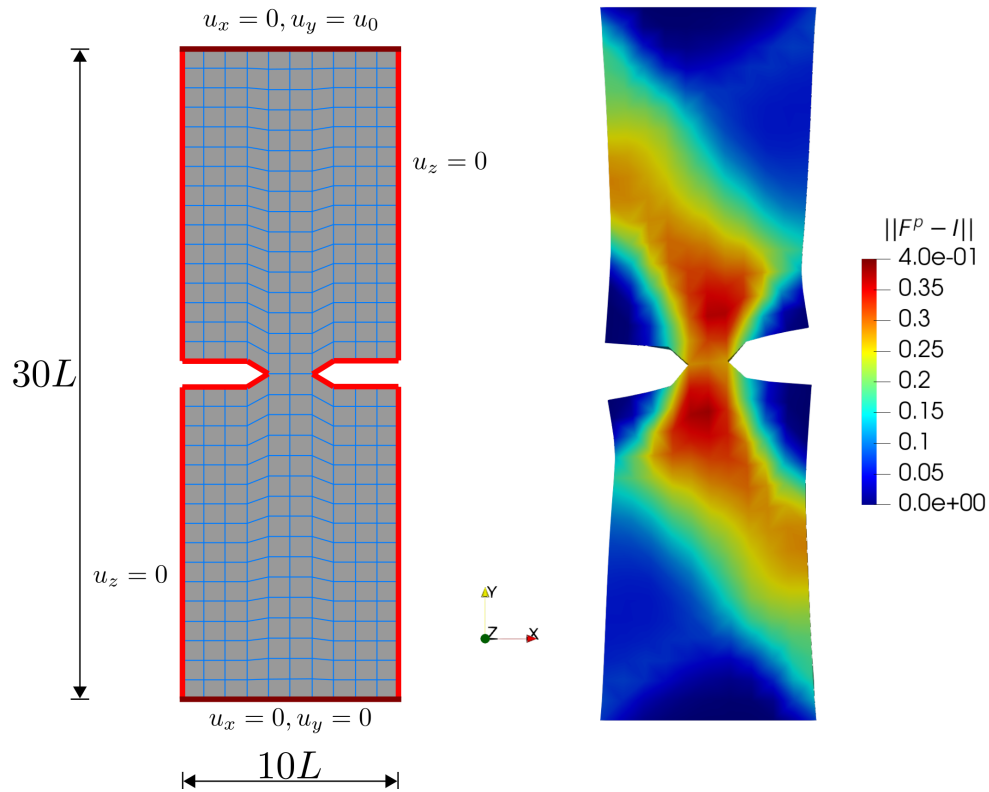


FIGURE 5.6: F-Bar example: Simulation setup (left) and deformed shape (right).

In Figure 5.6 the deformed shape of the sample computed with the F-Bar approach is shown, the contour plot illustrates the distribution of the plastic deformation. The crystal orientations are chosen such that large plastic deformation occurs, and the stiffening effect in the force-displacement diagram of the solution without F-Bar extension is clearly visible, see Figure 5.7.

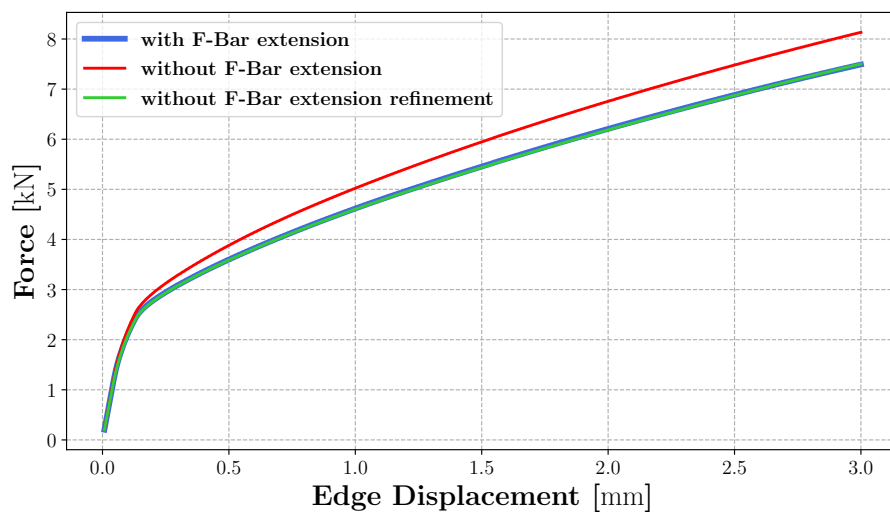


FIGURE 5.7: Force-displacement diagram to illustrate the locking in the simulation of the tensile test.

In this diagram, the blue line represents the solution with the F-Bar extension, and the red line shows the solution without the F-Bar method. Both with the same mesh of 742 elements. Thus, it is clearly visible, that the result with the F-Bar method shows a lower force at the same displacement, compared to the approach without F-Bar. Locking can always be alleviated by using finer meshes. The green line shows the result of a finer meshing of the sample with 2762 Elements without using the F-Bar approach. Obviously, the simulation using the F-Bar method with 742 elements are as good as simulations using a standard displacement formulation with 2762 elements.

5.4 Hardening

When metallic materials are undergoing plastic deformation, the materials show hardening behavior. In this work, three different hardening mechanisms are mentioned in the previous section, implemented in the material model, and will be compared in the following. Note, the F-Bar method is used for all the following simulations. To investigate the variation of the hardening mechanisms, once more the tensile test of a notched plate, displayed in Figure 5.6 on the left side, is performed. The material data remains the same as in Section 5.3. Figure 5.8 shows the deformed shape

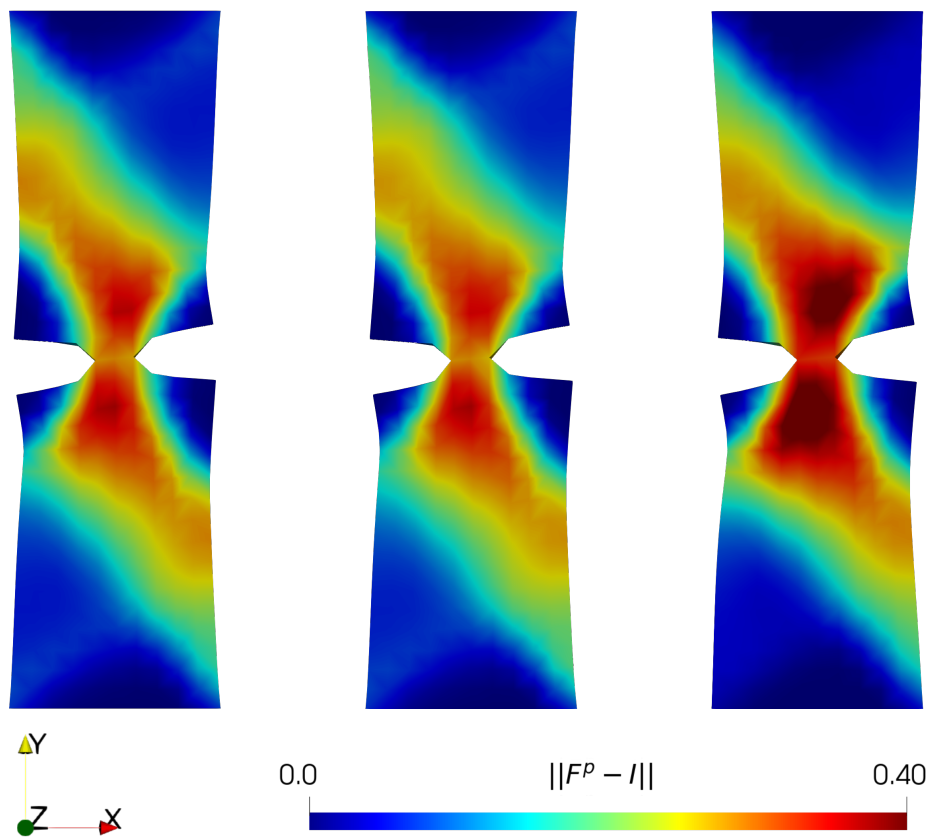


FIGURE 5.8: Deformed shape and distribution of plastic deformation after tensile test of notched plate for different hardening mechanisms. Isotropic linear hardening (left), latent linear hardening (middle) and latent Voce hardening (right).

of the notched plate after successful tensile test simulations for all three hardening mechanisms. Besides, the contour shows once more the distribution of the plastic deformation. In the distribution of the plastic deformation, changes are visible. The

changes between the isotropic linear hardening on the left side and the latent linear hardening in the middle are not so clearly visible, the plastic deformation of the middle simulation is spreading a little bit more. One can see a higher plastic deformation if the latent Voce hardening mechanism is used. Similar behavior is seen in the force diagram. While the tensile test shows for the isotropic and latent linear hardening nearly the same trend, the simulation with latent Voce hardening shows a significant higher hardening and thus a flattened course, see Figure 5.9. The latent linear and the latent Voce hardening introduce an additional nonlinearity into the material model. So, one would expect higher computational time with regard to isotropic linear hardening. And in fact, a higher number of iterations are visible for the latent linear and the Voce hardening. This results in a higher computational time. With respect to the isotropic linear hardening, the computational time increases about 31% for the latent linear hardening and even 784% for the latent Voce hardening for this relatively simple tensile test.

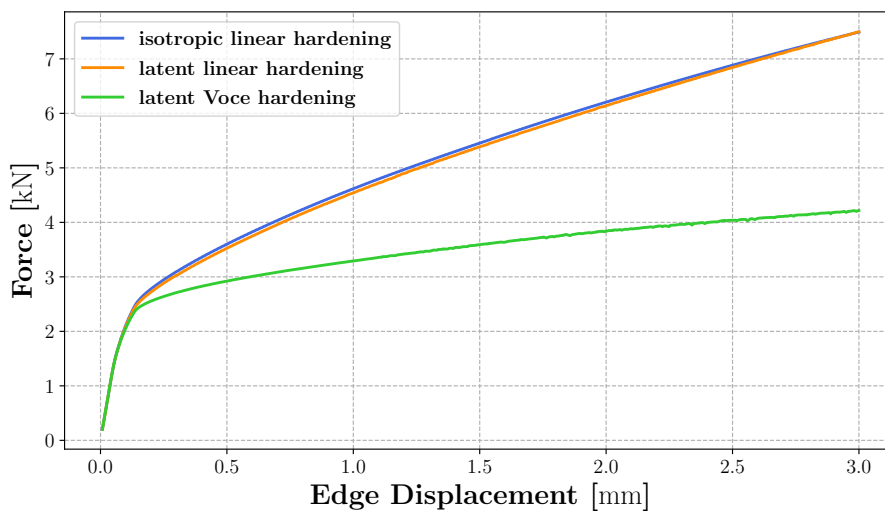


FIGURE 5.9: Force-displacement diagram for the variation of the hardening mechanism.

5.5 Material Separation

In the next chapter, the micro-cutting process is investigated. This process is a machining process in which a chip is cut off the workpiece. This material separation has to be modeled. For this purpose, two basic methods are presented in the previous chapter. A method based on purely geometric criteria and an approach based on damage mechanics. A simple micro-cutting setup is chosen to compare the two approaches for the mesh separation. The workpiece is fixed at the lowest edge, and the deformation perpendicular to the direction of movement of the tool, the z -direction, is locked. Even this simple example shows that the damage mechanics approach does not work without further restrictions. In the first phase, at the beginning of the contact between tool and workpiece, elements are deleted at different locations but not in the separation region. Furthermore, the parameter D_{crit} is not mesh independent and difficult to choose, even within one simulation. The results with the damage mechanics approach are shown in Figure 5.10 on the left are obtained with further restrictions. For example, only elements at the height of the tooltip may be deleted.

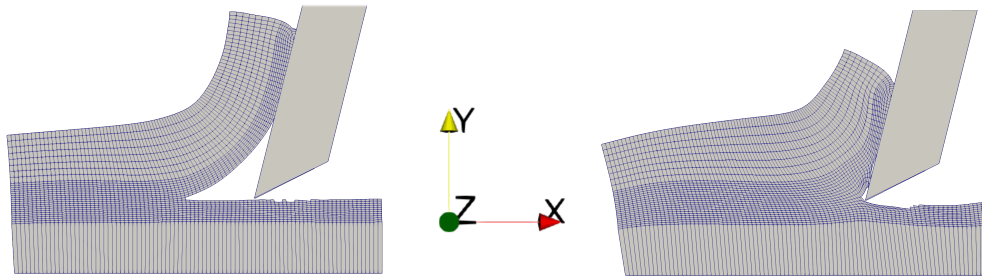


FIGURE 5.10: Comparison of the mesh separation approaches. The damage mechanics approach with further restrictions (left) and the geometrical approach (right).

Furthermore, an initial crack is introduced into the workpiece, and the front part is bent upwards to allow easier chip formation. Therefore, this method is not suitable for the use in the micro-cutting with large FEM meshes. On the right side of Figure 5.10, the result of the micro-cutting process with the geometrical approach, which is used in the following chapter, is shown.

Chapter 6

Micro-Cutting Simulations

In the previous chapter, details of the implementations are investigated separately. The advantages and disadvantages of the individual implementation choices were discussed. This has been done by simple validation examples. In the following, the concepts are combined to investigate the complex process of micro-cutting of cp-titanium. In the first section, the setup for the micro-cutting simulation is introduced, and the difficulty of symmetric crystal orientation and the critical phases in this setup are shown. In the next part, different process parameters and hardening mechanisms are varied, and their influence on the process is investigated. Finally, a simulation setup is built from a real microstructure of cp-titanium.

6.1 Simulation Setup for Micro-Cutting Simulations

The basic setup of all simulations is illustrated in Figure 6.1. The figure shows the tool with the width b_t and the rake angle α_t . The parameter t_c denotes the cutting depth of the tool relative to the workpiece. The workpiece has the dimensions width b_w , length l_w and height h_w . Thereby, it consists of one or multiple crystals with different orientations. The boundary conditions are defined in such a way that the workpiece is fixed at the bottom in all directions, and displacement of the tool is prescribed in positive y -direction. In addition, the tool is modeled as a rigid body. Mesh refinements, therefore, only affect the workpiece and not the tool. In the contact between tool and workpiece, only normal contact is considered, the influence of friction is neglected for the sake of simplicity. For the separation process, the geometrical approach is used due

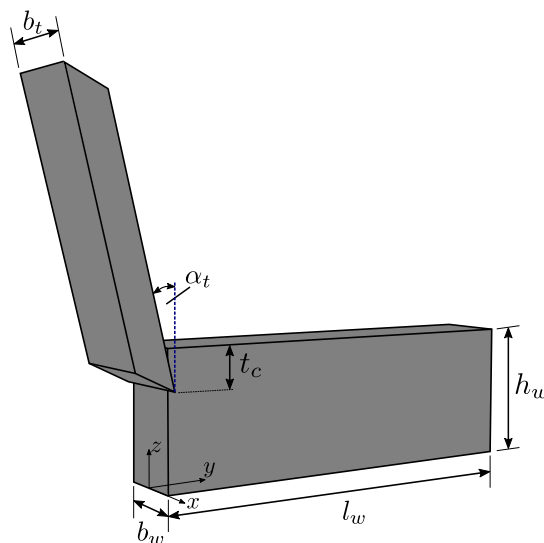


FIGURE 6.1: General setup of the micro-cutting simulation.

TABLE 6.1: Dimensions of example 1 and the symmetric crystal orientation vectors.

b_t [μm]	α_t [rad]	t_c [μm]	b_w [μm]	l_w [μm]	h_w [μm]	\vec{a}	\vec{b}
120	10	5	50	300	20	$\begin{bmatrix} 1 \\ 0 \\ 0 \end{bmatrix}$	$\begin{bmatrix} 0 \\ 1 \\ 0 \end{bmatrix}$

to the advantages compared to the damage mechanics approach. Of course, the geometrical dimensions, the mesh element size, and the crystal orientations are changing, depending on the specific examples. The material data of cp-titanium, which were also used in the previous chapter are published in Hama et al. (2016). These parameters used for the following simulations, if not stated differently. In addition, pure isotropic hardening is used if nothing different is mentioned, and only the main slip systems are initially considered. The following first example shows that the simulation of the micro-cutting process works in general. But it also reveals the first challenges within the process simulation. For this example, the workpiece is modeled as a single crystal,

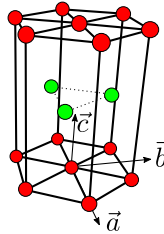


FIGURE 6.2: Hcp unit cell and orientation vectors.

which is symmetrically oriented. The parameters for the simulation setup and the crystal orientation are listed in Table 6.1. To indicate the crystal orientation with the vectors \vec{a} and \vec{b} , the hexagonal unit cell is shown in Figure 6.2 again. The meshing for this example and the following examples of the parameter variation is intentionally chosen as coarse as possible to save simulation time on the one hand and to illustrate the effects sufficiently accurately on the other hand. The simulation setup with the meshing of the workpiece for this first example is shown in Figure 6.3. On the left side of Figure 6.4 the whole workpiece and the tool is depicted.

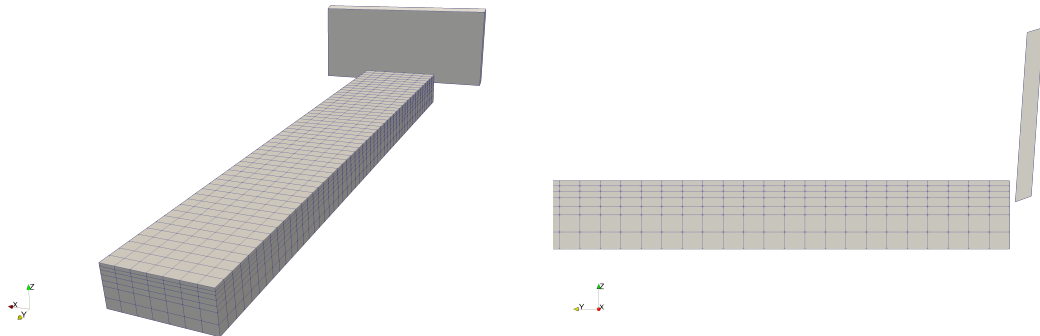


FIGURE 6.3: FEM mesh for the symmetric crystal orientation example.

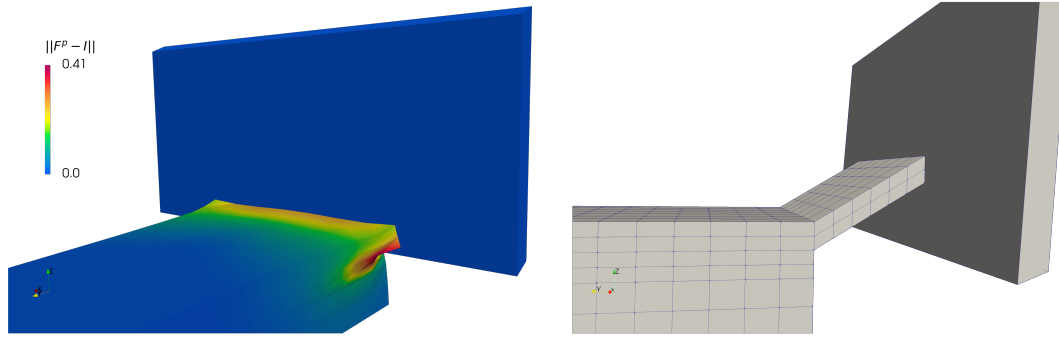


FIGURE 6.4: Initial contact situation of tool and workpiece (left); mesh with auxiliary elements to prevent chip forming problems (right).

Next to this, a side view is shown, where the cutting depth of $t_c = 5 \mu\text{m}$ and the rake angle $\alpha_t = 10^\circ$ of the tool can be seen. The workpiece is not visible completely in this side view. Considering the results, a crucial observation is that the process of initial contact between workpiece and tool until the chip forms and slides over the tool is the most critical time period during the simulation in terms of robustness. For this example, the simulation aborts shortly after the first contact. The Newton iteration does not converge in this time step. The chip shows deformations to the side and is pushed forward due to the crystal orientation instead of sliding over the tool. This point in time is shown in Figure 6.4 on the left side. The contour shows the norm of the plastic deformation gradient minus the identity tensor, $\|\mathbf{F}^p - \mathbf{I}\|$, which indicates the distribution of the plastic deformation. It can be seen that the

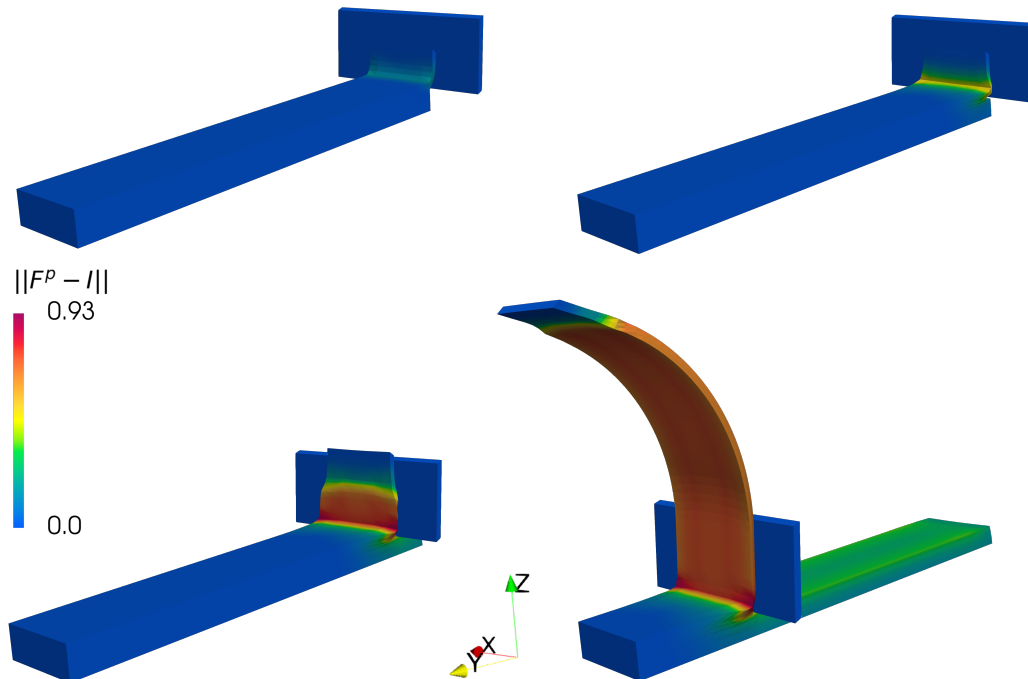


FIGURE 6.5: Chip formation in example 1 with auxiliary elements at different time steps:

plastic deformation is very high in the contact area and that the chip bends outwards, which leads to a very unfavorable deformation state. Two approaches are followed to circumvent the stability problem at the first contact between workpiece and tool. In the first approach, additional elements are added to the workpiece, which is depicted in Figure 6.4 on the right side. These additional elements allow the chip to bend upwards easily and consequently slide over the tool. This approach helps to overcome the critical deformation state, and the simulation does not abort but terminates as expected after the entire tool displacement is applied. The result can be seen at four different time steps in Figure 6.5. Furthermore, a symmetrical distribution of the plastic deformation can be seen, which is expected for the symmetrical orientation of the crystal and validates the implementation of the material model once again. The symmetrical orientation of the chip can be seen in the front view in Figure 6.6 on the left side. The evaluation of the force of the tool in y -direction, hereinafter

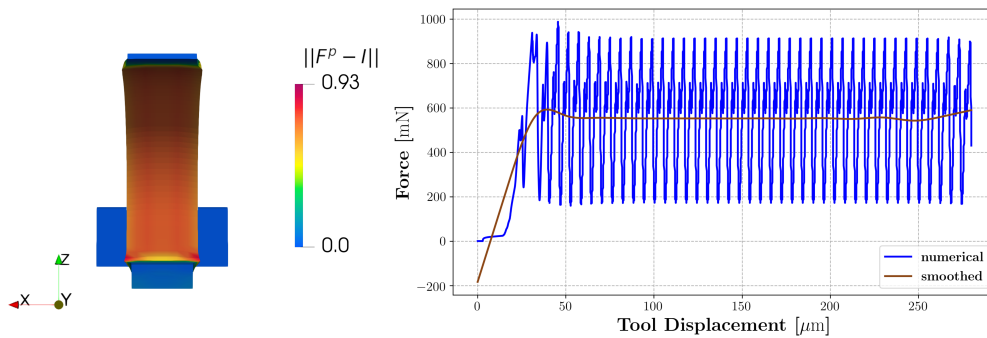


FIGURE 6.6: Front view of the chip forming (left) and force of the tool (right) of example 1.

referred to as the cutting force F_{cut} , over the displacement of the tool is presented in Figure 6.6 on the right side. The blue graph shows the evaluation resulting from the numerical simulation, based on the evaluation element by element. The course in brown displays the smoothed cutting force. The evolution of the cutting force over time reveals a quasi-harmonic behavior, except for the initial contact. Noticeable are the high amplitudes. The fluctuations are caused by the method of the separation of chip and workpiece. As resistance is built upon the tool due to chip formation, the stiffness drops from one time step to the other due to the deletion of elements, and the force signal decreases. The amplitude depends on the size of the elements in the separation zone between the workpiece and chip. For the chosen discretization, the amplitude is quite high since it is in the same order of magnitude as the mean value of the cutting force.

TABLE 6.2: Crystal orientation vectors of example 2.

Orientation 1		Orientation 2	
\vec{a}	\vec{b}	\vec{a}	\vec{b}
$\begin{bmatrix} 0.756474 \\ 0.371916 \\ -0.537982 \end{bmatrix}$	$\begin{bmatrix} -0.510099 \\ -0.179299 \\ -0.841220 \end{bmatrix}$	$\begin{bmatrix} 1 \\ 0 \\ 0 \end{bmatrix}$	$\begin{bmatrix} 0 \\ 1 \\ 0 \end{bmatrix}$

The second approach to avoid the critical state at the initial contact between workpiece and tool is to place another crystal in front of the symmetrically aligned crystal. Thus, the workpiece is changed to a double crystal. The orientation of the first crystal

is chosen so that it favors the chip formation upwards. This variant is shown in Figure 6.7. The blue part of the workpiece illustrates the first crystal and the grey part of the second crystal. The orientations are listed in Table 6.2. The length of the workpiece is reduced to $l_w = 100 \mu\text{m}$. This simulation also aborts when the tool

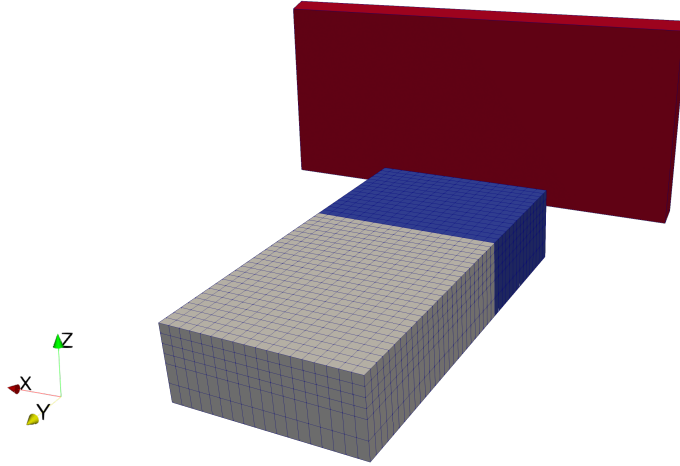


FIGURE 6.7: Example 2: FEM mesh of the double crystal setup.

reaches the symmetrically aligned crystal. The result at this time step is shown in Figure 6.8. It can be clearly seen how the chip initially forms anisotropic in the x -direction. However, as soon as the tool reaches the transition from the first to the second crystal, strong transverse expansion in x -direction can be observed. A similar critical state as in the first example is reached, and the simulation stops. It can be concluded that, from a perspective of the stability of the simulation, a symmetrically oriented crystal, and a vertical grain boundary, compare to Table 6.1, can lead to critical deformation states, which in turn lead to difficulties in the nonlinear iteration process. This situation can be solved by adding special elements. The two examples show that, in general, it is possible to perform and analyze micro-cutting processes with the setup described here.

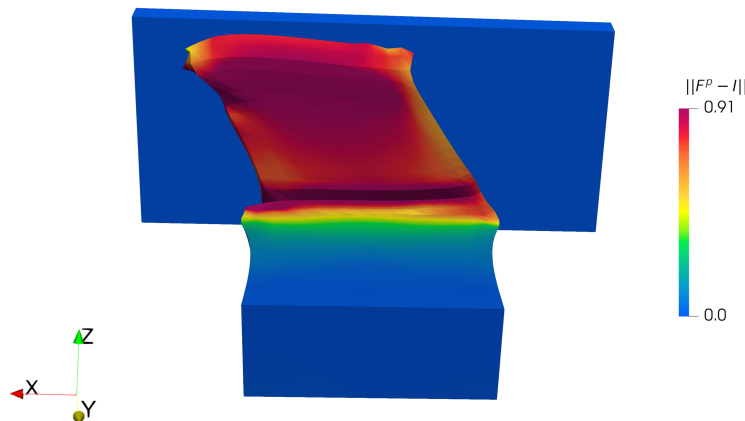


FIGURE 6.8: Deformed shape of the double crystal at the time step, when the simulation aborts.

TABLE 6.3: Crystal orientation vectors of the grain variation examples.

Simulation	Grain 1	Grain 2	Grain 3	Grain 4
1	$\vec{a} = \begin{bmatrix} 0.994 \\ 0.114 \\ 0.004 \end{bmatrix}$	$\vec{a} = \begin{bmatrix} 0.047 \\ 0.802 \\ 0.596 \end{bmatrix}$	$\vec{a} = \begin{bmatrix} 0.938 \\ 0.330 \\ 0.109 \end{bmatrix}$	$\vec{a} = \begin{bmatrix} -0.158 \\ 0.921 \\ 0.356 \end{bmatrix}$
	$\vec{b} = \begin{bmatrix} -0.064 \\ 0.530 \\ 0.845 \end{bmatrix}$	$\vec{b} = \begin{bmatrix} -0.834 \\ -0.295 \\ 0.464 \end{bmatrix}$	$\vec{b} = \begin{bmatrix} -0.345 \\ 0.853 \\ 0.392 \end{bmatrix}$	$\vec{b} = \begin{bmatrix} -0.933 \\ -0.258 \\ 0.253 \end{bmatrix}$
2	$\vec{a} = \begin{bmatrix} 0.569 \\ 0.819 \\ -0.074 \end{bmatrix}$	$\vec{a} = \begin{bmatrix} 0.287 \\ -0.809 \\ -0.513 \end{bmatrix}$	$\vec{a} = \begin{bmatrix} 0.787 \\ 0.540 \\ 0.300 \end{bmatrix}$	$\vec{a} = \begin{bmatrix} -0.791 \\ -0.602 \\ -0.112 \end{bmatrix}$
	$\vec{b} = \begin{bmatrix} -0.707 \\ 0.441 \\ -0.553 \end{bmatrix}$	$\vec{b} = \begin{bmatrix} -0.730 \\ -0.531 \\ 0.430 \end{bmatrix}$	$\vec{b} = \begin{bmatrix} -0.600 \\ 0.783 \\ 0.166 \end{bmatrix}$	$\vec{b} = \begin{bmatrix} -0.156 \\ 0.375 \\ -0.914 \end{bmatrix}$
3	$\vec{a} = \begin{bmatrix} -0.784 \\ -0.517 \\ -0.343 \end{bmatrix}$	$\vec{a} = \begin{bmatrix} -0.417 \\ 0.123 \\ 0.900 \end{bmatrix}$	$\vec{a} = \begin{bmatrix} 0.942 \\ 0.301 \\ -0.148 \end{bmatrix}$	$\vec{a} = \begin{bmatrix} -0.787 \\ 0.180 \\ -0.590 \end{bmatrix}$
	$\vec{b} = \begin{bmatrix} 0.603 \\ -0.504 \\ -0.618 \end{bmatrix}$	$\vec{b} = \begin{bmatrix} -0.634 \\ -0.749 \\ -0.191 \end{bmatrix}$	$\vec{b} = \begin{bmatrix} 0.056 \\ -0.576 \\ -0.815 \end{bmatrix}$	$\vec{b} = \begin{bmatrix} -0.604 \\ -0.419 \\ 0.678 \end{bmatrix}$

6.2 Variation of the Crystal Orientation

It has been shown in the previous section that the simulation of the micro-cutting process is possible with the chosen implementations. Now the influence of the crystal orientation on the deformation and the cutting force is to be investigated. For this purpose, simulations are executed, whereby the workpiece consists of four crystals, also called grains, with different orientations. The grain boundary remains parallel to the tooltip, as in the previous examples. The length of the workpiece is $l_w = 200 \mu\text{m}$.

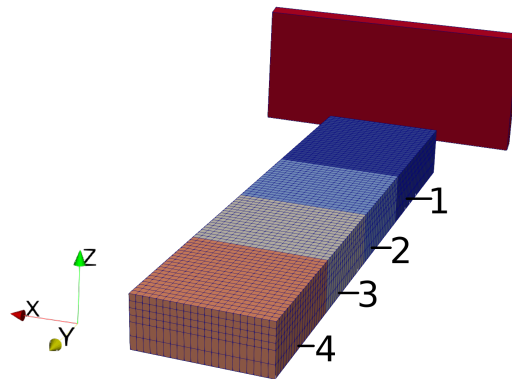
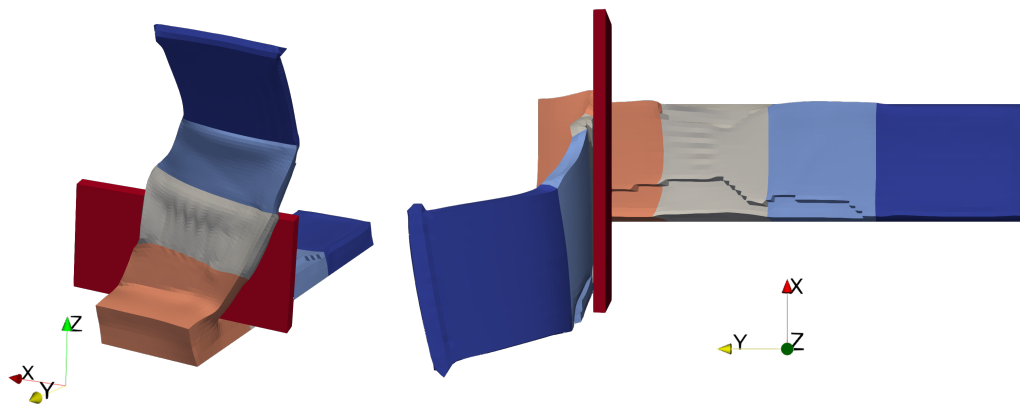
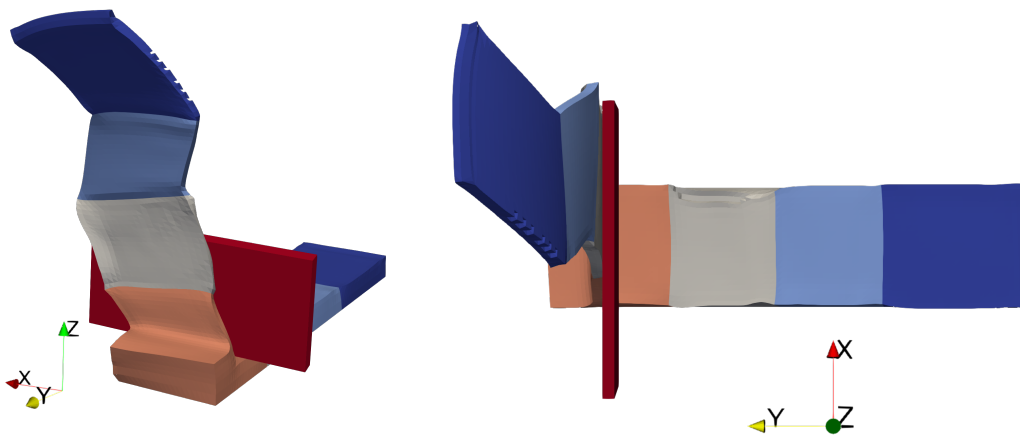


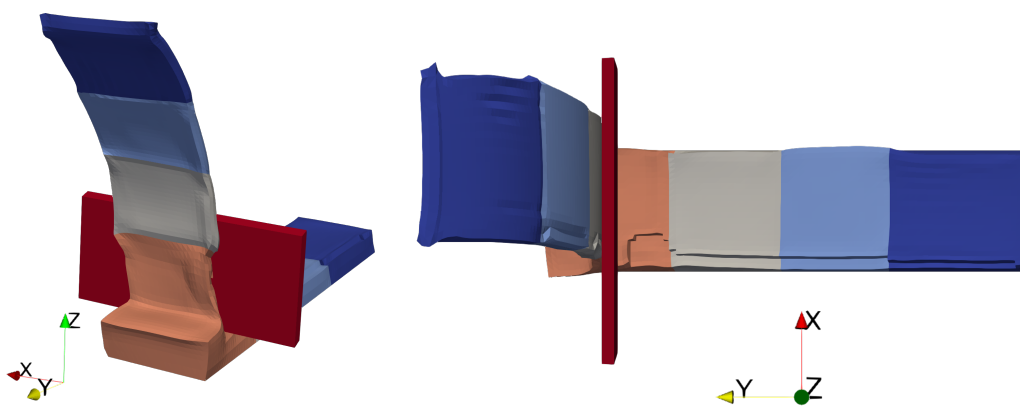
FIGURE 6.9: Example 3: mesh with four different crystal orientations.



(a) Simulation 1



(b) Simulation 2



(c) Simulation 3

FIGURE 6.10: Chip formation and top view of micro-cutting process with workpiece of four different crystal orientations. Displacement of the tool $w_{\text{tool}} = 185 \mu\text{m}$.

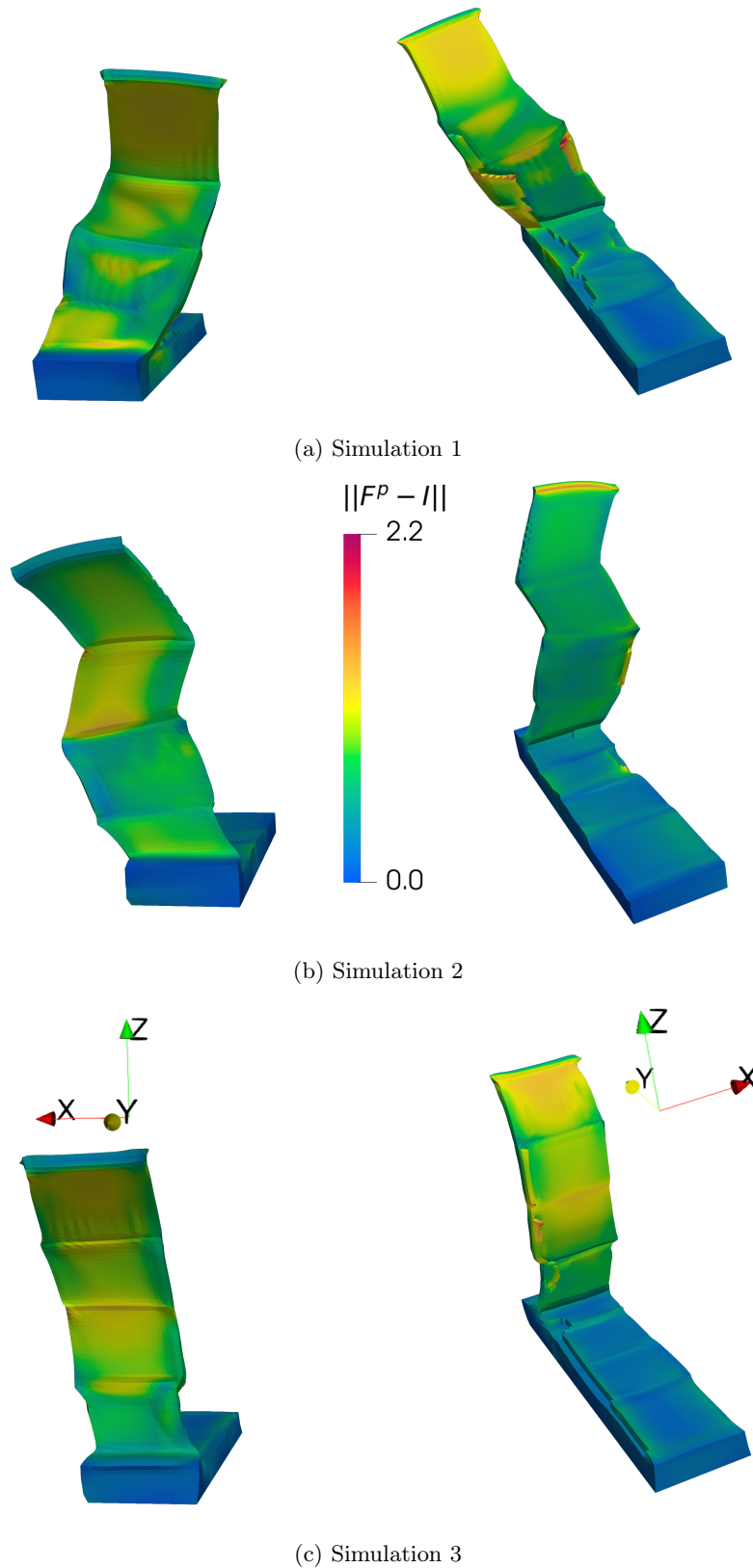


FIGURE 6.11: Deformed shape of the chip, where different bending of the chip is visible (left) and the resulting surface, which shows different height for simulation 1, 2 and 3. The contour shows the distribution of the plastic deformation after a tool displacement of $w_{\text{tool}} = 185 \mu\text{m}$.

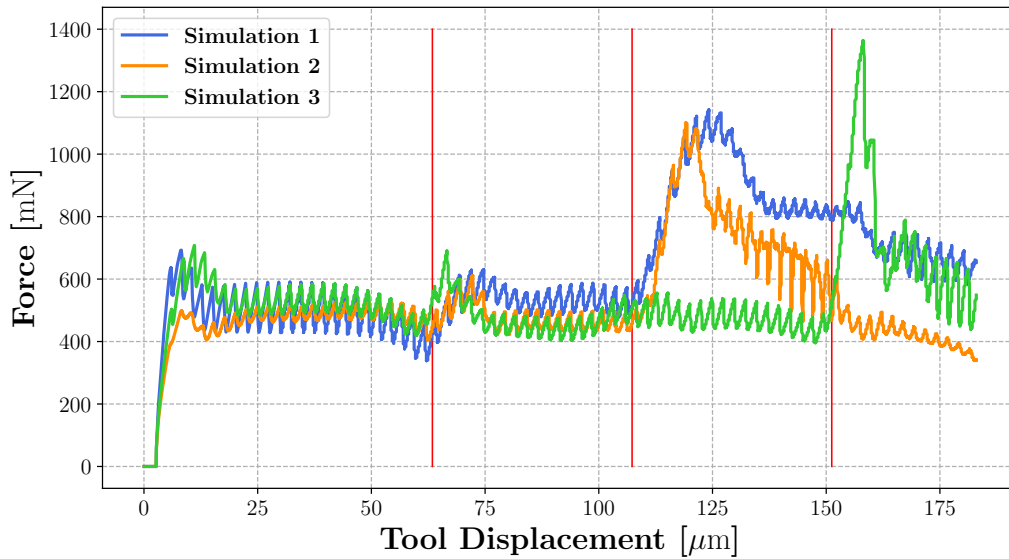


FIGURE 6.12: Cutting force of the crystal orientation variation examples.

The setup and meshing are illustrated in Figure 6.9, where the different colors of the workpiece represent different crystal orientations. Since the number of all possible orientations to each other is far too high, only tendencies are examined here. Several simulations are performed, where the grain orientation of all grains is chosen randomly. Three of these examples are shown here. The orientation vectors are listed in Table 6.3. In general, it can be stated that if the grain has an approximately symmetrical orientation, stability problems will occur. In some cases, only the number of iterations increases until the respective time step converges, other simulations terminate completely. The results of the three simulations are shown in the Figures 6.10 and 6.11. The first figure displays the influence of the crystal orientation on the deformation of the chip and the workpiece. On the left side, the chip can be seen from the front. On the right side, the top view of the workpiece and the chip is shown. For simulation 1 on the top, it can be recognized that the chip bends in different directions at the grain boundaries. This behavior is even more pronounced in simulation 2 in the middle. In contrast, the chip in simulation 3 at the bottom is almost straight. Moreover, it can be observed that the chip changes its width. While the chip becomes wider in the transition from grain 2 to grain 3 in simulation 1 and 2, it narrows considerably in the last grain of simulation 3. Figure 6.10, on the right side, also shows different curvature of the tip of the chip. The width of the workpiece also changes depending on the grain orientation. Finally, a slightly different thickness of the chip is also visible. Figure 6.11 demonstrates the influence of grain orientation on the plastic deformation. The contour shows again $\|\mathbf{F}^p - \mathbf{I}\|$ as in the previous examples. The tool is hidden for better visibility. The dependence of the plastic deformation on the grain orientation is clearly visible. In addition, the curvature of the resulting workpiece surface depends on grain orientation. In Figure 6.11, on the front side of the chip, the grain boundaries are clearly visible due to the plastic deformation, compare the plots on the left side, whereas this is not always the case on the backside of the chip, see the plots on the right side. However, a clear difference in the surface on the back of the chip can be identified. If one now compares these visual observations with the cutting force,

displayed in Figure 6.12, where the red lines mark the grain boundaries, the following can be determined. Simulation 1 shows a slight increase of F_{cut} at the transition from grain 1 to grain 2 and a strong increase within grain 3, which is also consistent with the strong deformation of the chip in this section. Simulation 2 shows a very similar course, with force decreasing faster in the region of the third grain. Here the width of the chip increases in the region of high cutting force. However, a correlation with the plastic deformation is not clearly recognizable. For simulation 3, the cutting force remains relatively constant in the first three grains, which is also consistent with the uniformity of the chip formation. In the third grain, the cutting force then increases sharply while the chip constricts strongly. In general, it can still be seen that the amplitude decreases significantly in all curves due to the smaller elements in the mesh separation region compared to the first example in Figure 6.6. The investigations clarify the dependencies of the deformation and cutting force on crystal orientation.

6.3 Variation of the Cutting Depth

The cutting depth is a process parameter that has a direct influence on the chip thickness. Since this, in turn, influences the cutting force, the influence of the cutting depth on the micro-cutting process is investigated. For this example, the number of grains of the workpiece is reduced to two grains with different orientations. The length of the workpiece is $l_w = 120 \mu\text{m}$. The cutting depth t_c is varied from $2 \mu\text{m}$ up to $10 \mu\text{m}$ in five different simulations. The simulation setup is displayed in Figure 6.13, the orientation vectors of the two grains are listed in Table 6.4.

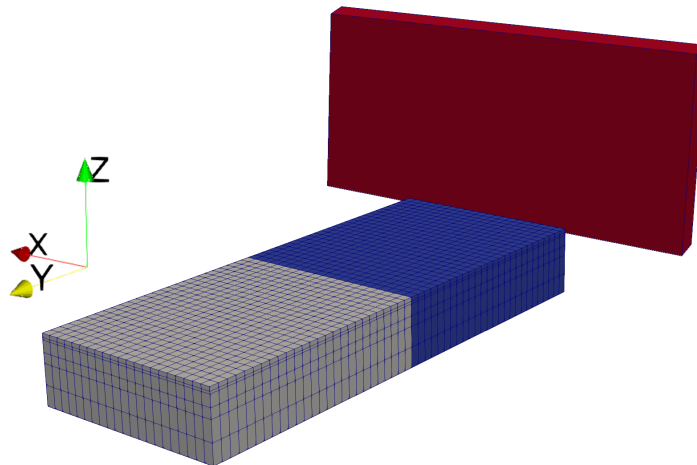


FIGURE 6.13: Simulation setup with two different crystal orientations for the variation of the cutting depth.

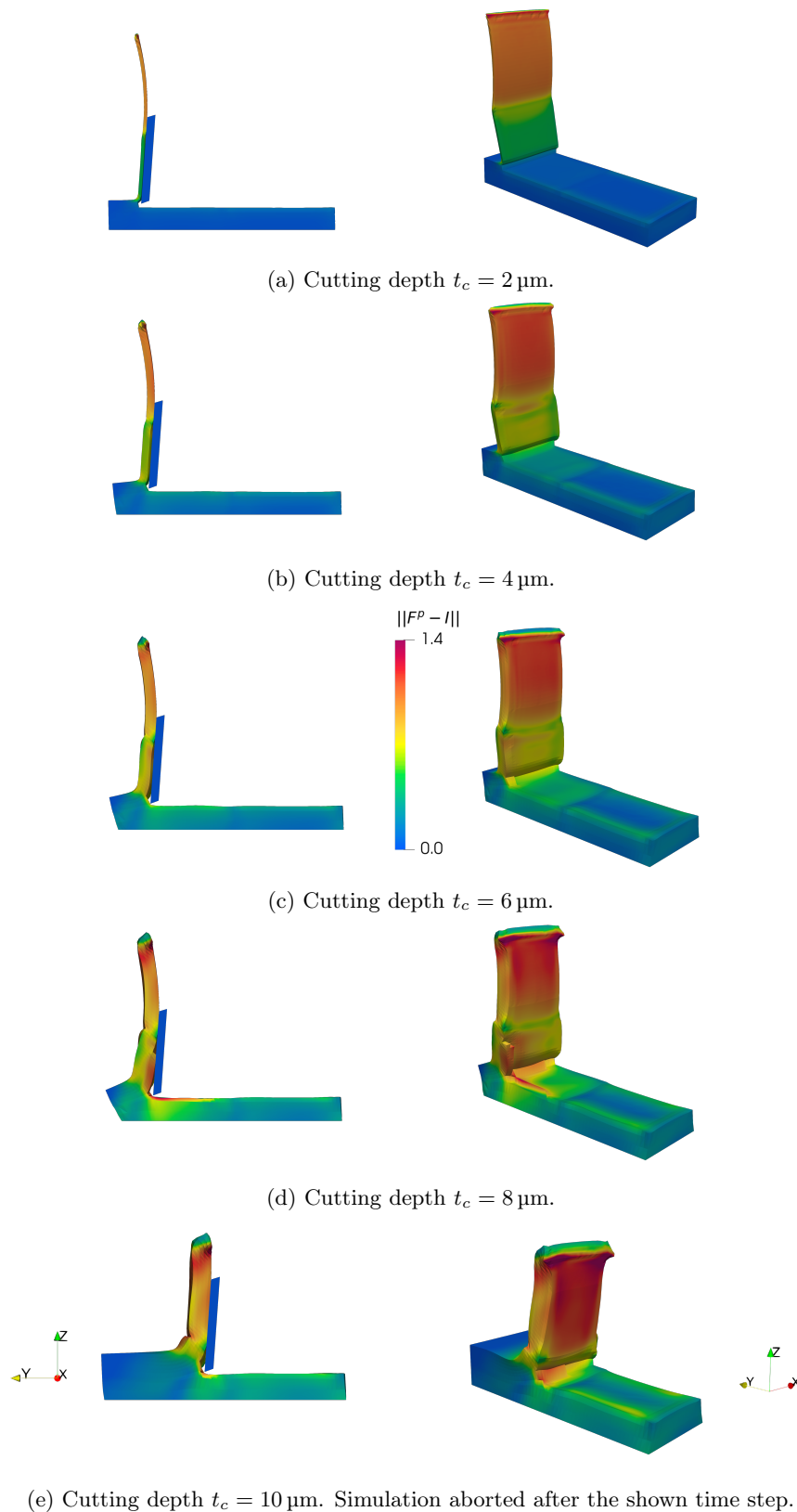


FIGURE 6.14: Deformed chip (left) and resulting surface, where the tool is not displayed, (right) resulting from micro-cutting simulation with different cutting depth t_c . The contour shows the distribution of the plastic deformation

TABLE 6.4: Crystal orientation vectors of the variation of cutting depth.

Grain 1	Grain 2
$\vec{a} = \begin{bmatrix} 0.993 \\ 0.114 \\ 0.004 \end{bmatrix}$	$\vec{a} = \begin{bmatrix} 0.047 \\ 0.802 \\ 0.596 \end{bmatrix}$
$\vec{b} = \begin{bmatrix} -0.064 \\ 0.530 \\ 0.845 \end{bmatrix}$	$\vec{b} = \begin{bmatrix} -0.834 \\ -0.295 \\ 0.464 \end{bmatrix}$

The chip and the resulting surface after the process are shown in Figure 6.14. It should be mentioned that the calculation with the cutting depth of $t_c = 10 \mu\text{m}$ aborted due to divergence in the nonlinear iteration. The evaluation up to the interruption is shown. The contour indicates the distribution of the plastic deformation. On the left side, there is a side view where the chip thickness and the plastic deformation of the chip are directly visible. On the right, the tool is hidden to see the back of the chip. In addition, the resulting surface can be viewed. The cutting depth increases from top to bottom in steps of $2 \mu\text{m}$. In general, the cutting depth has no significant influence on the shape of the chip. Shape and curvature are approximately the same in all results. However, differences can be seen when considering the plastic deformation. For a cutting depth of $2 \mu\text{m}$, the plastic deformation of the chip is distributed very evenly. A significant change occurs across the grain boundary from higher plastic deformation to lower plastic deformation. The resulting workpiece surface also shows an almost uniform and low plastic deformation for the whole surface. At a higher cutting depth, the plastic deformation increases. The difference in plastic deformation from grain 1 to grain 2 decreases for the chip, while it increases for the remaining surface of the workpiece. It is noticeable that especially the edge area of the workpiece shows higher plastic deformation, clearly visible in the region of the first grain. A bulge is forming. At a cutting depth of $8 \mu\text{m}$, finally, the chip in the section of the second grain has no

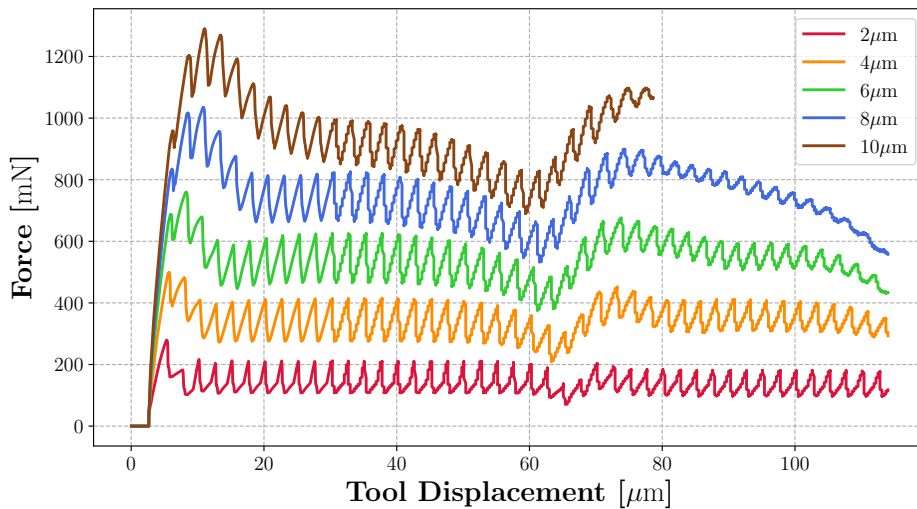


FIGURE 6.15: Cutting force of simulations with different cutting depths.

longer a constant thickness. Also, the resulting surface shows significant differences in thickness. The cutting force is evaluated in Figure 6.15. As expected, the cutting force increases with a higher t_c . For the cutting depth $t_c = 2\ \mu\text{m}$, F_{cut} remains at about the same level for the entire process, with only a minimal drop at the grain boundary. But the higher the cutting depth, the more pronounced is the following behavior. A higher initial F_{cut} with a decrease towards the grain boundary and a stronger re-increase in the region of the second grain. This re-increase correlates with the chip thickness shown in Figure 6.14. Also, the region of grain 2 shows a higher plastic deformation at a higher t_c .

6.4 Variation of the Rake Angle

Another process parameter, which influences the cutting process, is the rake angle α_t . The rake angle is defined as the angle between the vertical, here the z -axes, and the cutting face, also called the rake face, of the tool, see Figure 6.1. From the macroscopic cutting process literature, such as Denkena and Toenshoff (2011) or Böge and Böge (2015), it is known that smaller rake angles lead to higher cutting forces. To investigate this observation in micro-cutting processes, simulations with varying rake angle are performed. Therefore, the same simulation setup for the workpiece, as in Section 6.3, is used. The cutting depth is $5\ \mu\text{m}$, and the rake angle varies from 0° to 10° in 6 simulations. The deformed shapes with chip and workpiece surface are shown in the Figures 6.16 and 6.17. In the first figure, the side view can be seen, and the second figure shows a view of the resulting surface and the back of the chip. Again, for better visibility, the tool is hidden. As indicated by the tool in Figure 6.16, the rake angle increases in both figures from the upper left picture, where the rake angle is 0° , in steps of 2° to the lower right picture, where the rake angle is 10° . It can be observed that while the plastic deformation of the chip decreases with a higher rake angle, the plastic deformation on the resulting surfaces is nearly constant. In addition, the grain boundary is clearly visible. The rake angle has no significant influence on the plastic deformation of the resulting surface.

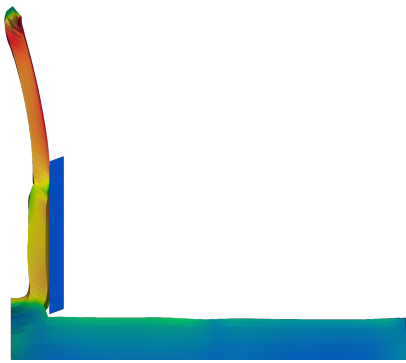
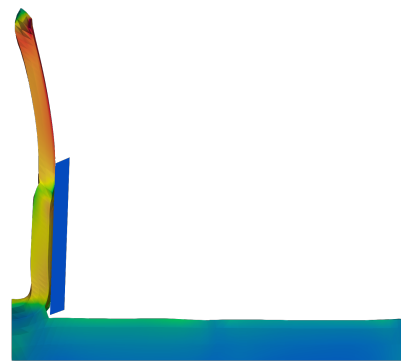
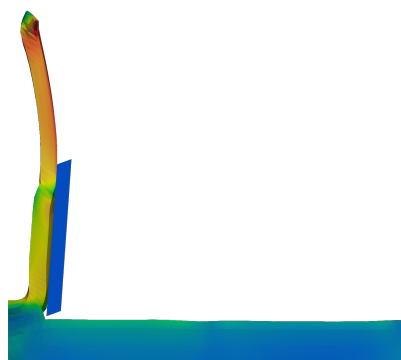
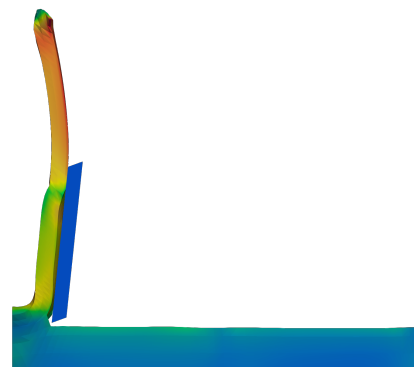
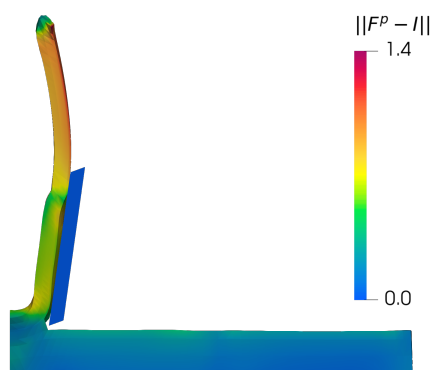
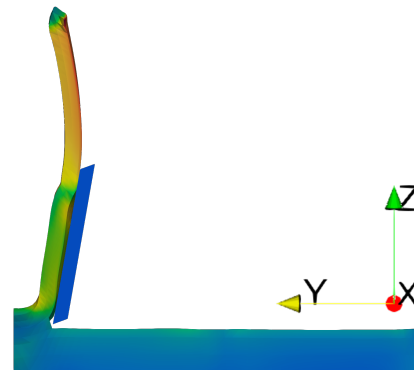
(a) Rake angle $\alpha_t = 0^\circ$.(b) Rake angle $\alpha_t = 2^\circ$.(c) Rake angle $\alpha_t = 4^\circ$.(d) Rake angle $\alpha_t = 6^\circ$.(e) Rake angle $\alpha_t = 8^\circ$.(f) Rake angle $\alpha_t = 10^\circ$.

FIGURE 6.16: Variation of the rake angle - deformed shape and plastic deformation in the side view.

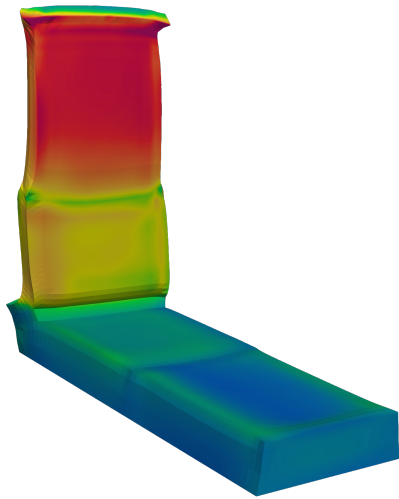
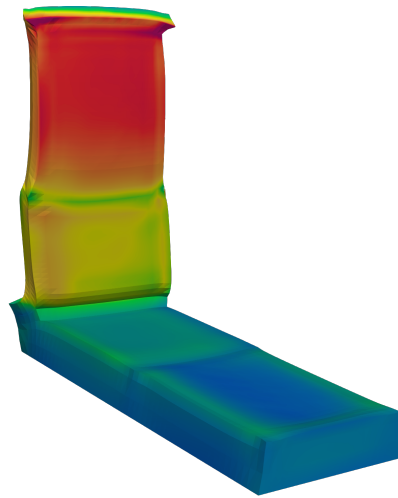
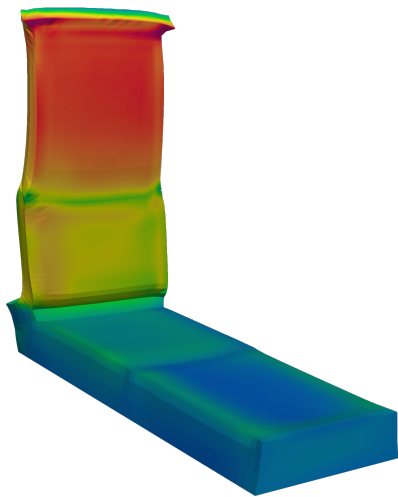
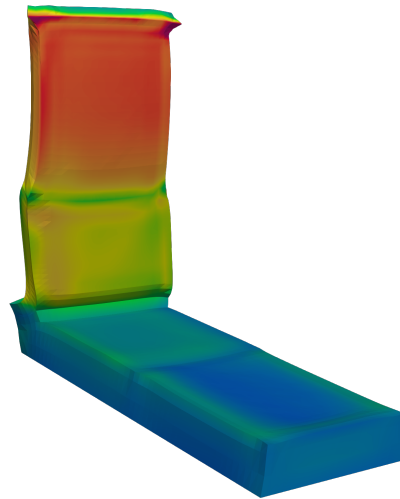
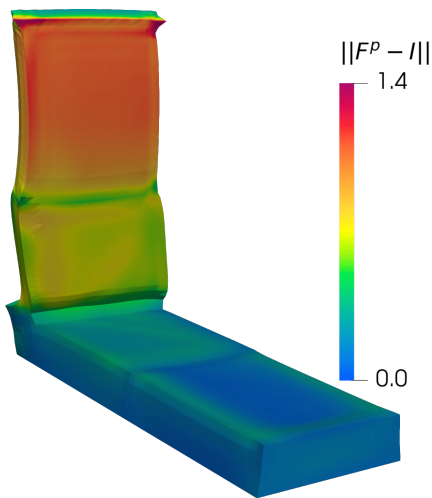
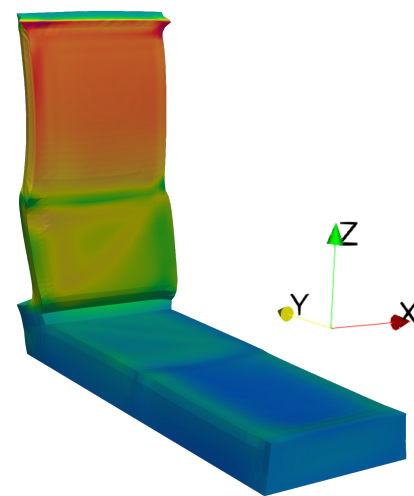
(a) Rake angle $\alpha_t = 0^\circ$.(b) Rake angle $\alpha_t = 2^\circ$.(c) Rake angle $\alpha_t = 4^\circ$.(d) Rake angle $\alpha_t = 6^\circ$.(e) Rake angle $\alpha_t = 8^\circ$.(f) Rake angle $\alpha_t = 10^\circ$.

FIGURE 6.17: Variation of the rake angle - deformed shape and plastic deformation of the back of the chip and the workpiece surface.

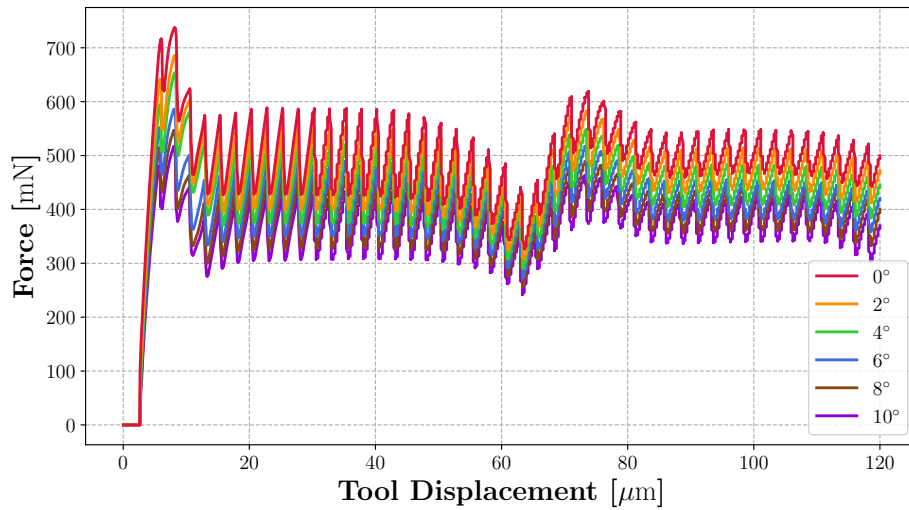


FIGURE 6.18: Cutting force with different rake angle.

The decreasing plastic deformation of the chip points out that the above statement of a smaller rake angle causes higher cutting forces also applies to the micro-cutting process. And in fact, this result can be seen in the cutting force, which is displayed in Figure 6.18. Also, the rake angle has no influence on the cutting force change when passing the grain boundary. The change of the force is nearly the same in all simulations. In the smoothed cutting force, see Figure 6.19, one can observe that the force-displacement curves are very similar. All curves increase strongly at the beginning and then fall down again a small amount. At the grain boundary, there is first a short decrease of the force and then a stronger rise followed by a slight drop to a constant force curve. Small differences can be seen in the initial phase. Especially between the simulation with the rake angle $\alpha_t = 4^\circ$ and $\alpha_t = 6^\circ$, the gap is a bit larger.

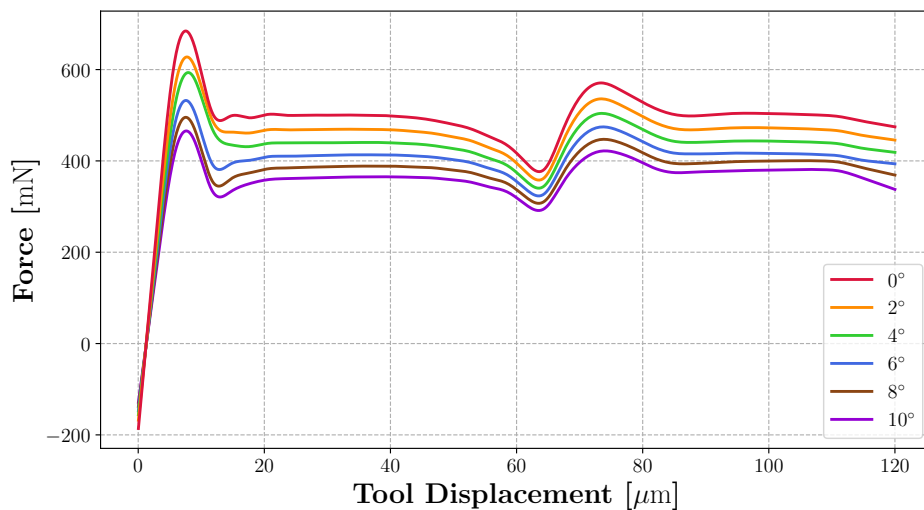


FIGURE 6.19: Smoothed cutting force with different rake angle.

6.5 Variation of the Hardening Mechanism

In Section 4.2 different hardening mechanisms are introduced. In the previous chapter, it is shown that there is no significant difference between isotropic linear hardening and latent linear hardening, besides the required calculation time. Only the latent Voce hardening shows a different plastic deformation and a significant change in the force-displacement diagram. Since the tensile test is a simple setup with lower plastic deformation in contrast to the micro-cutting process, the influence of the hardening mechanism on the micro-cutting simulation should be investigated. For the simulation, the same setup as in Section 6.3 with a cutting depth of $3\ \mu\text{m}$ and a rake angle of 10° is chosen. Considering observed computational costs, however, it becomes apparent that the application of the latent Voce hardening is not useful for the micro-cutting procedure because the time step size must be chosen very small, and thus the simulation duration increases strongly. This model is, therefore, not suitable for productive calculations of the micro-cutting process. Furthermore, it should be mentioned, that latent linear hardening also yields excessive computational costs. Thus, only isotropic linear and latent linear hardening mechanisms are compared here for the micro-cutting process. Figure 6.20 shows the deformed shape and the distribution

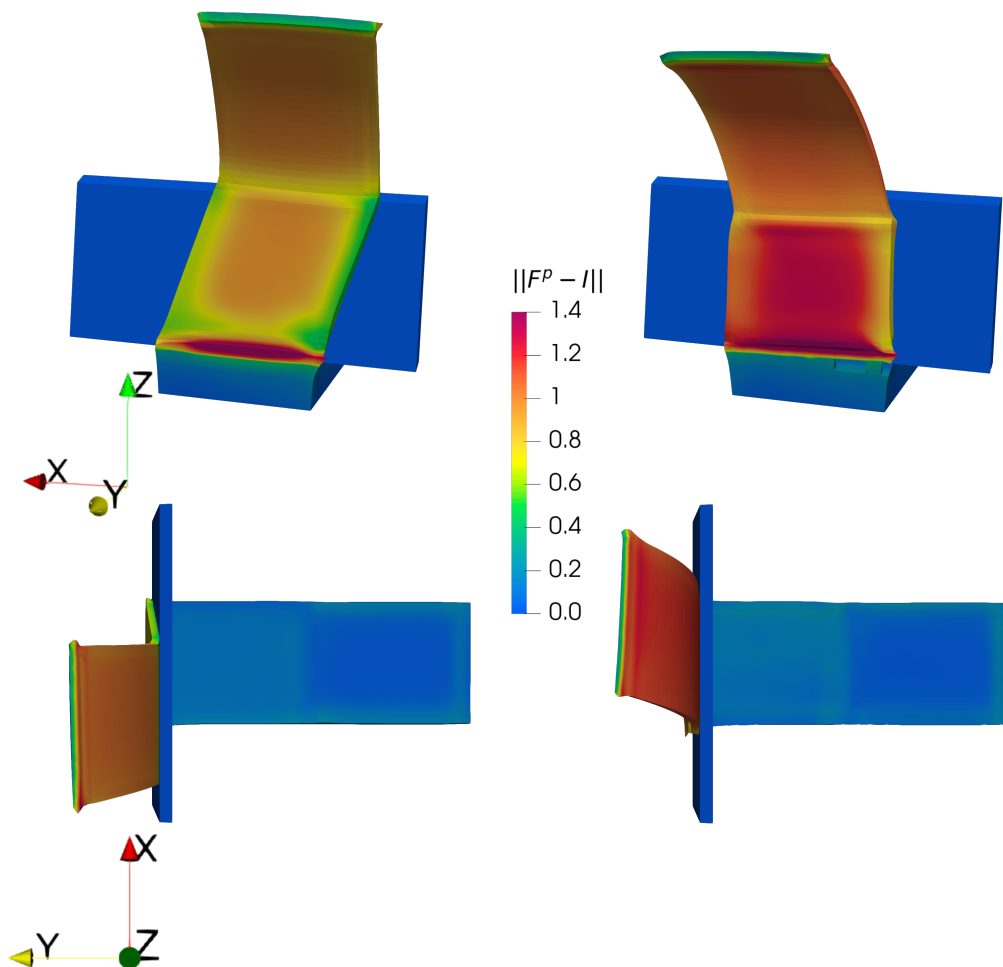


FIGURE 6.20: Chip formation and resulting surface for the micro-cutting process with isotropic linear hardening (left) and latent linear hardening (right).

of the plastic deformation. It can be observed that there is a significant difference between the two hardening mechanisms. One can see a higher plastic deformation on the right side of Figure 6.20, where latent linear hardening is used, compared to the simulation with the isotropic linear hardening on the left side. In addition, the two chips deform differently. While the chip bends to the right side for isotropic hardening, it bends to the left for latent linear hardening. Another difference can be seen on the grain boundary of the chip. While on the left side, the chip nearly maintains its width, a different shape develops on the right side, and the chip becomes a little wider. The resulting surfaces, in contrast, show almost the same deformation. From the cutting

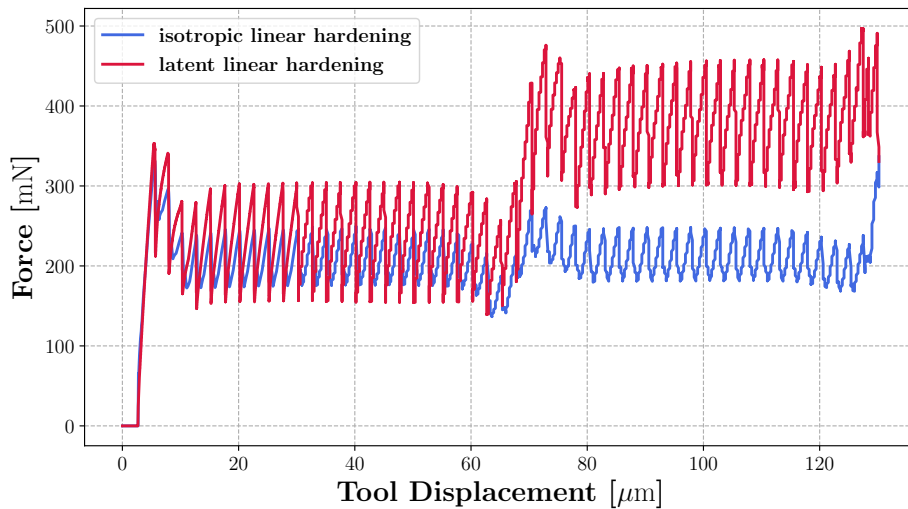


FIGURE 6.21: Cutting force of the micro-cutting process with two different hardening mechanisms.

force provided in Figure 6.21, the following can be evaluated. In the region of the first grain, a similar cutting force is observed for both hardening mechanisms. But the fluctuations, based on the element deletion algorithm, are higher for the latent linear hardening mechanisms. As expected, the higher hardening leads to a higher stiffness until finally, another element is deleted. If the tool reaches the second grain, a large difference in F_{cut} is visible. For latent linear hardening, the tool force increases strongly. This larger difference, which can be seen between the hardening effect in the tensile test and in the micro-cutting process, can be explained by two phenomena. First, the plastic deformation, which occurs in the cutting process, is much higher than the plastic deformation in the tensile test. The amount of plastic deformation has a direct influence on the amount of hardening since hardening directly depends on the plastic slip. The second phenomenon is yielded by the crystal orientation, which happens to be such that in latent linear hardening, more slip systems are favored to be active, and with that, higher plastic deformation is favored. In conclusion, it can be said that the hardening mechanism used has a significant influence on material deformation and cutting force in the micro-cutting process.

6.6 Micro-Cutting Simulations of Real Material

In the previous sections, it is shown that the micro-cutting process can be simulated, but the implementation is very involved, and a multitude of difficulties have to be handled. Subsequently, several influences on the process are investigated. The setups used for the micro-cutting process in the previous sections are to a certain degree of academic nature. For example, only one grain has been used over the entire width of the workpiece, and the grain boundary is parallel to the tooltip. This perfect state will never exist in real structures. This motivates the investigation of real structures, also, with regard to the functionality and stability of the chosen model. Therefore, in the following the procedure of creating a FEM mesh for the simulation from a real cp-titanium material is described.

6.6.1 Microstructure and Corresponding FEM Mesh

Starting from the raw material, a sample has been produced in cooperation with the Institute for Manufacturing Technology and Production Systems of TU Kaiserslautern, which contains bars on its surface with a width of $100\ \mu\text{m}$ and a height of $80\ \mu\text{m}$, see Figure 6.22. In the following step, the surfaces of the bars were polished.

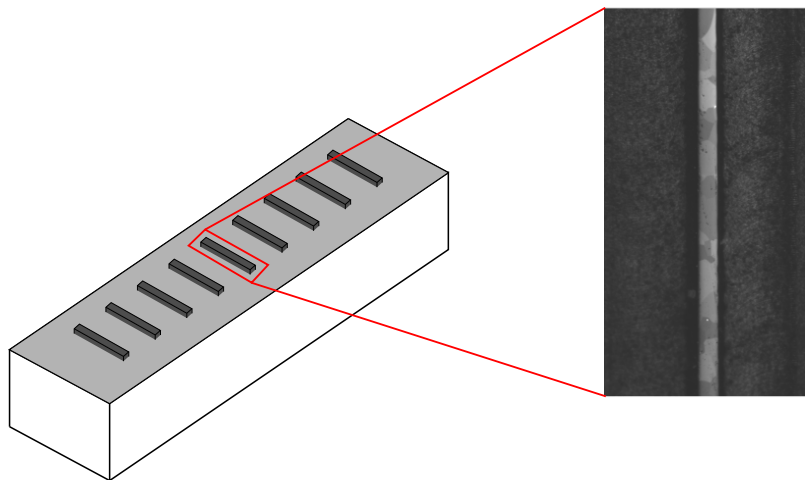


FIGURE 6.22: Manufactured bars and microscopic picture.

By light microscopy, two examples, which show the clearest structure with grains across the entire width of the bar as well as several grains next to each other, are selected. With the Electron Backscatter Diffraction (EBSD) Method, the grains can be made visible in different colors, and the crystal orientation of each grain can be determined. This investigation was carried out in cooperation with the Institute for Surface and Thin Film Analysis (IFOS) in Kaiserslautern. The light microscopic picture and the results of the EBSD analysis are displayed in Figure 6.23. Now, with the known microstructure and the known crystal orientations, the next step is to create a FEM mesh. Since the meshing of a whole bar would result in too many elements and the calculation time would increase unacceptably, only a section with a length of about $600\ \mu\text{m}$ and width of $100\ \mu\text{m}$ is used. This surface section is divided into rectangular elements. Each element is assigned the corresponding crystal with the specific orientation. The resulting two-dimensional mesh serves as a template for the three-dimensional workpiece. The procedure is illustrated in Figure 6.24. Finally, the surface mesh is projected into the third dimension. The resulting workpiece, which can be used for the micro-cutting simulation, is shown in Figure 6.25. The specific

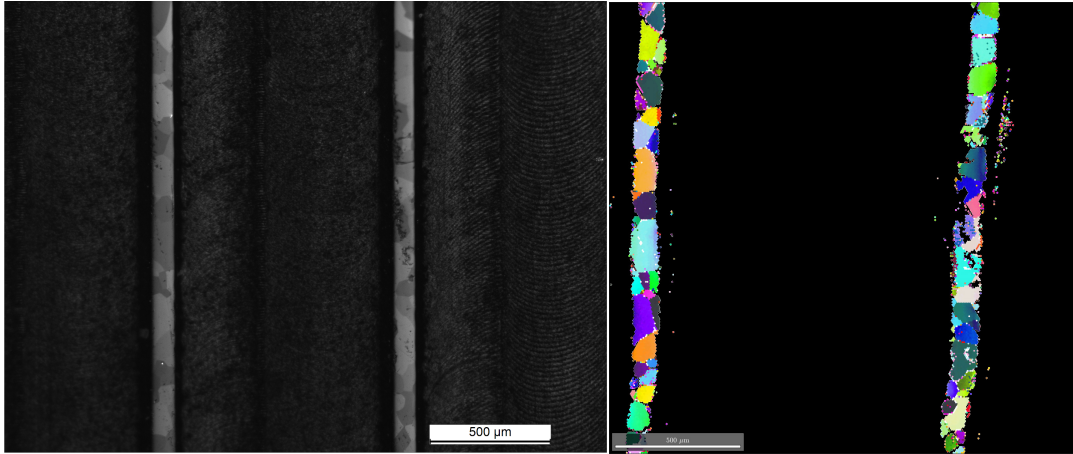


FIGURE 6.23: Microscopic picture and the EBSD analysis for the two example bars.

grains are displayed in different colors. The corresponding crystal orientations, according to the numbering in Figure 6.24, are listed in Table 6.5. The mesh element size has been reduced compared to the examples in the previous sections in order to obtain more accurate results of the chip formation and the resulting workpiece surface as well as the cutting force. The created workpiece mesh contains about 60,000 elements and about 210,000 degrees of freedom. Up to now, the influence of the element size, and thus, the mesh size on the results has not been investigated. For this reason, a second, finer mesh is created additionally. The number of elements is increased to approximately 114,000, resulting in approximately 387,000 degrees of freedom. The refinements are achieved by finer surface meshing and by smaller elements in the region of mesh separation. The aim of this investigation is to determine whether the use of higher resources compared to the results is justified. In the following, the coarser mesh will be referred to as mesh 1 and the finer mesh as mesh 2.

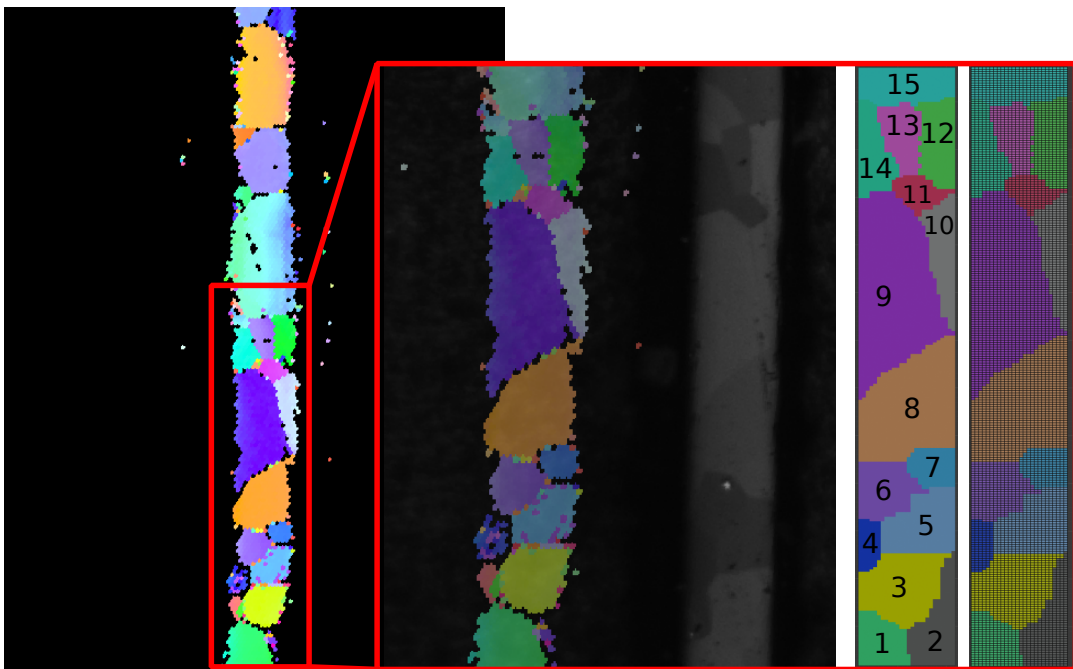


FIGURE 6.24: Surface mesh of real material based on EBSD investigations.

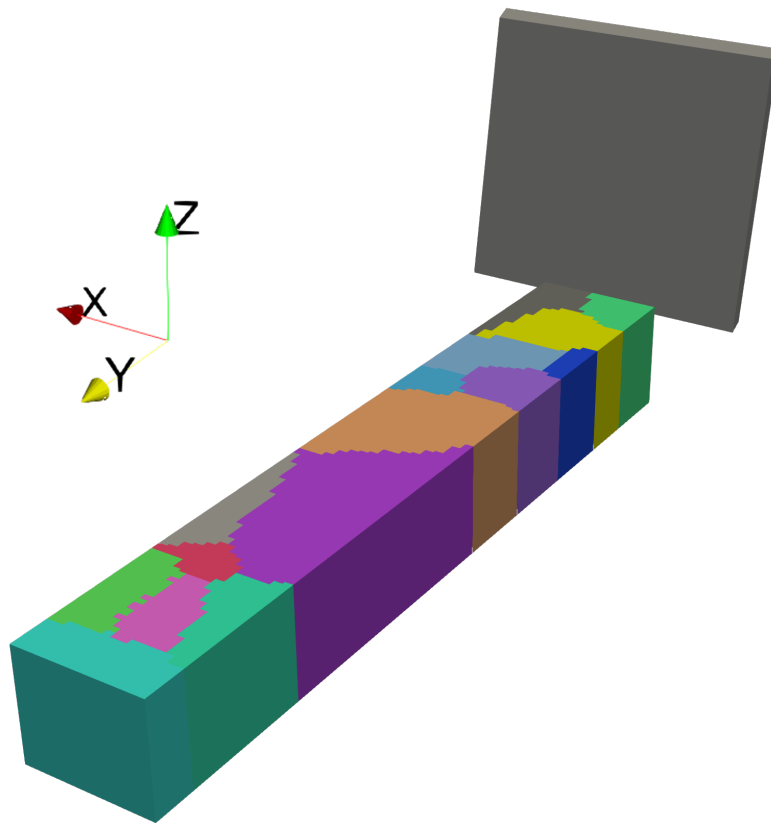


FIGURE 6.25: Simulation setup for micro-cutting of real material.

TABLE 6.5: Crystal orientation vectors of the real structure mesh.

Grain 1	Grain 2	Grain 3	Grain 4
$\vec{a} = \begin{bmatrix} 0.756 \\ 0.372 \\ -0.538 \end{bmatrix}$	$\vec{a} = \begin{bmatrix} 0.756 \\ 0.372 \\ -0.538 \end{bmatrix}$	$\vec{a} = \begin{bmatrix} 0.565 \\ 0.342 \\ 0.751 \end{bmatrix}$	$\vec{a} = \begin{bmatrix} 0.491 \\ 0.683 \\ -0.541 \end{bmatrix}$
$\vec{b} = \begin{bmatrix} -0.510 \\ -0.179 \\ -0.841 \end{bmatrix}$	$\vec{b} = \begin{bmatrix} -0.510 \\ -0.179 \\ -0.841 \end{bmatrix}$	$\vec{b} = \begin{bmatrix} -0.722 \\ 0.646 \\ 0.248 \end{bmatrix}$	$\vec{b} = \begin{bmatrix} 0.227 \\ 0.499 \\ 0.836 \end{bmatrix}$
Grain 5	Grain 6	Grain 7	Grain 8
$\vec{a} = \begin{bmatrix} 0.417 \\ -0.064 \\ -0.907 \end{bmatrix}$	$\vec{a} = \begin{bmatrix} 0.623 \\ 0.755 \\ 0.205 \end{bmatrix}$	$\vec{a} = \begin{bmatrix} 0.134 \\ 0.087 \\ 0.987 \end{bmatrix}$	$\vec{a} = \begin{bmatrix} -0.867 \\ -0.291 \\ 0.404 \end{bmatrix}$
$\vec{b} = \begin{bmatrix} 0.889 \\ 0.235 \\ 0.392 \end{bmatrix}$	$\vec{b} = \begin{bmatrix} -0.168 \\ 0.385 \\ -0.908 \end{bmatrix}$	$\vec{b} = \begin{bmatrix} -0.984 \\ -0.104 \\ 0.142 \end{bmatrix}$	$\vec{b} = \begin{bmatrix} 0.421 \\ -0.861 \\ 0.284 \end{bmatrix}$
Grain 9	Grain 10	Grain 11	Grain 12
$\vec{a} = \begin{bmatrix} 0.019 \\ -0.502 \\ 0.864 \end{bmatrix}$	$\vec{a} = \begin{bmatrix} 0.274 \\ 0.715 \\ -0.643 \end{bmatrix}$	$\vec{a} = \begin{bmatrix} -0.057 \\ -0.793 \\ 0.607 \end{bmatrix}$	$\vec{a} = \begin{bmatrix} 0.438 \\ 0.263 \\ -0.860 \end{bmatrix}$
$\vec{b} = \begin{bmatrix} -0.549 \\ 0.717 \\ 0.429 \end{bmatrix}$	$\vec{b} = \begin{bmatrix} -0.689 \\ -0.320 \\ -0.650 \end{bmatrix}$	$\vec{b} = \begin{bmatrix} 0.744 \\ -0.439 \\ -0.504 \end{bmatrix}$	$\vec{b} = \begin{bmatrix} -0.730 \\ -0.455 \\ -0.511 \end{bmatrix}$
Grain 13	Grain 14	Grain 15	
$\vec{a} = \begin{bmatrix} 0.557 \\ 0.826 \\ -0.090 \end{bmatrix}$	$\vec{a} = \begin{bmatrix} -0.345 \\ 0.334 \\ 0.877 \end{bmatrix}$	$\vec{a} = \begin{bmatrix} 0.965 \\ 0.254 \\ -0.070 \end{bmatrix}$	
$\vec{b} = \begin{bmatrix} -0.375 \\ 0.154 \\ -0.914 \end{bmatrix}$	$\vec{b} = \begin{bmatrix} -0.635 \\ 0.605 \\ -0.480 \end{bmatrix}$	$\vec{b} = \begin{bmatrix} 0.014 \\ 0.216 \\ -0.976 \end{bmatrix}$	

6.6.2 The Micro-Cutting Simulation of Real Material

The micro-cutting simulation has been successfully completed for both meshes. Consequently, both simulations are evaluated and compared. First mesh 1 is considered, and in the following step mesh 2 is evaluated.

Evaluation of the process

Figure 6.26 shows the progress of the micro-cutting process and the chip formation at two different time steps for mesh 1. The contour, again, shows $\|F^p - I\|$ as measure for the plastic deformation. On the left side, a plateau is clearly visible on the chip surface, and an increase in plastic deformation at the grain boundaries can be observed. The right figure shows a similar situation at a later point. Depending on the grain and the specific orientation, regions of higher and lower plastic deformation can be seen, and the grain boundaries are clearly visible. Furthermore, one can see that the chip first bends in negative x -direction, but later on, it slides again almost centrally over the tool. In addition, the bending of the chip forward is also noticeable.

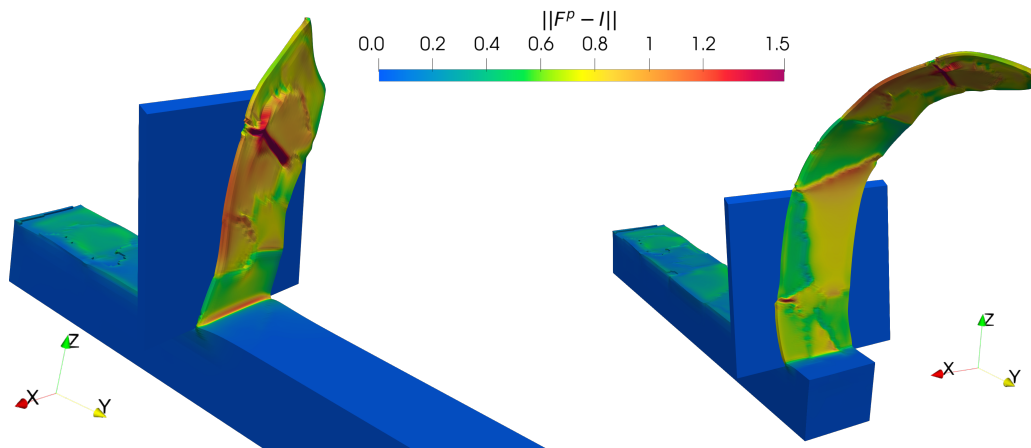


FIGURE 6.26: Chip forming during micro-cutting process for mesh 1.

Now, the resulting surface of the micro-cutting process is studied. The contour of the workpiece in Figure 6.27 provides the distribution of the plastic deformation at the end of the cutting process, and in Figure 6.28 the resulting height profile of the surface can be seen by showing the relative displacement in z -direction, u_z . The tool is not displayed for the sake of better visibility of the surface. It can be seen

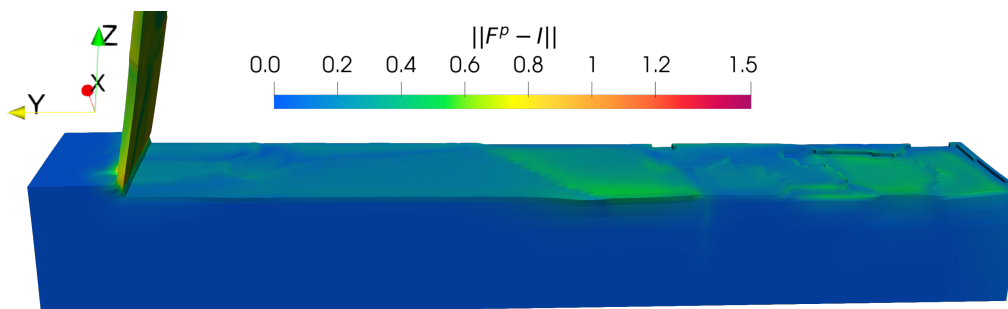


FIGURE 6.27: Surface after the micro-cutting process. The contour shows the distribution of the plastic deformation.

that an uneven surface arises. On both figures, the grain boundaries are partially visible. The height profile shows, that dependent on the crystal orientation, higher and lower regions arise. Consequently, material accumulation often occurs at the grain boundaries. From Figure 6.27, it is recognizable that the most plastic deformation occurs in the first half of the workpiece. In this region, the highest differences in height are also visible. Another interesting aspect is that there are often material elevations at the edges of the workpiece.

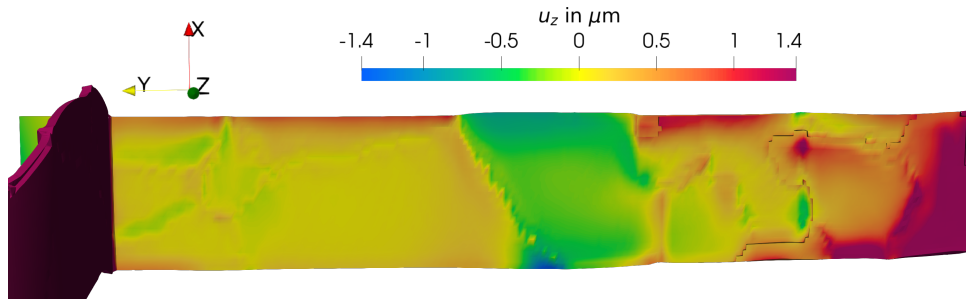


FIGURE 6.28: Height profile of the surface of the workpiece after micro-cutting process.

Influence of the element size

The influence of the element size is investigated, by comparing the results provided above to the results of the finer mesh 2. In general, the results of mesh 1 and 2 provided in Figure 6.29 and Figure 6.26, respectively, show a qualitatively good agreement. There is a deformation of higher and lower value, depending on the specific grains, and a pile-up of material on specific grain boundaries. In mesh 2, the plastic deformation is of higher intensity and the bending to the side, see Figure 6.29 on the left, is stronger. In addition, an unrealistic structure is formed at the beginning of the chip, where a pointed structure with large plastic deformation can be seen. The same statements can be made, when the formed surface, given in Figures 6.30 and 6.31, is compared. The trend of deformation remains consistent with mesh 1, but the plastic deformation, as well as the deformation u_z , which forms the height profile, are higher. What is particularly noticeable on the formed surface is the wave-like structure in the middle of the workpiece.

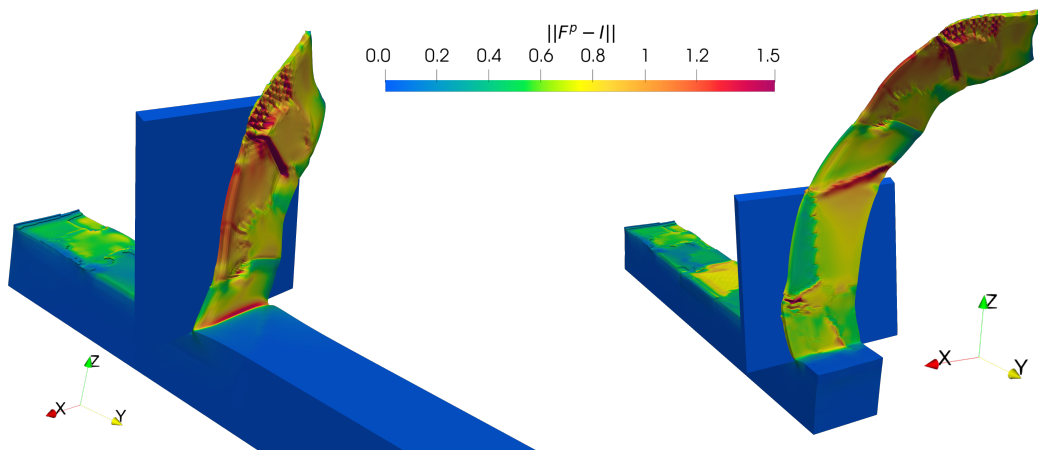


FIGURE 6.29: Chip forming during micro-cutting process for mesh 2.

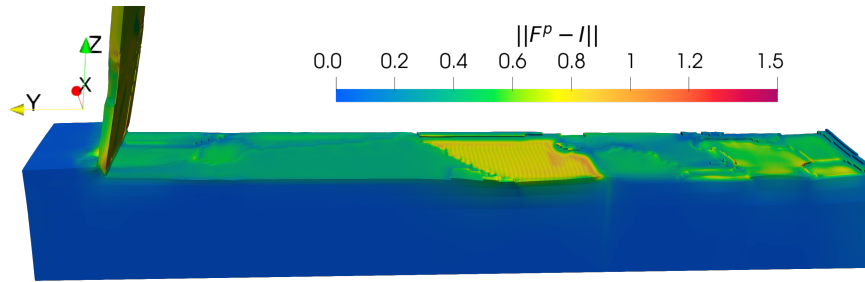


FIGURE 6.30: Surface after the micro-cutting process. The contour shows the distribution of the plastic deformation.

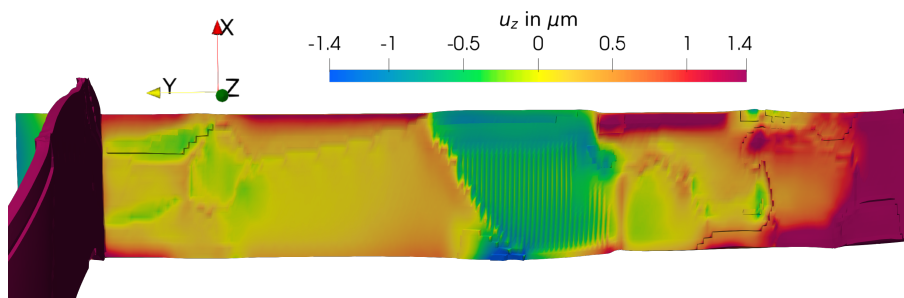


FIGURE 6.31: Height profile of the surface of the workpiece after micro-cutting process.

This region also shows a higher plastic deformation compared to the other parts of the surface. The higher plastic deformation is also visible for mesh 1 in Figure 6.27, but the difference to the rest of the workpiece is lower. By comparing the cutting force curve of both meshes, similar observations as for the deformations and the plastic strains can be made. The two curves are qualitatively very well agreeing. Only in some areas, e.g., with a tool displacement of $50\ \mu\text{m} - 100\ \mu\text{m}$, slight differences can be seen. However, the entire course for mesh 2 is shifted towards higher cutting force.

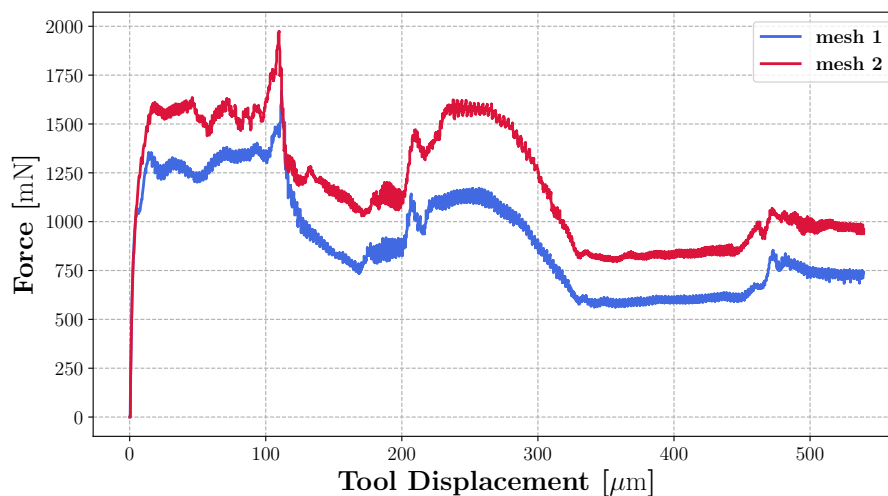


FIGURE 6.32: Comparison of the cutting force for the coarser mesh 1 and the finer mesh 2.

6.6.3 Influence of All Slip Systems

As described in Section 4.2 the $\langle c+a \rangle$ slip systems have a very low impact on the total plastic deformation because of the very high initial shear stress. Now, there are different statements about the initial shear stress in the literature. In Hama et al. (2016) there is a given value for the initial shear stress for the $\langle c+a \rangle$ slip systems of $\tau_0 = 145$ MPa, which is not significantly more than the initial shear stress of the basal slip system of $\tau_0 = 133$ MPa. In contrast, Lütjering and Williams (2013) report a significantly higher initial shear stress to activate the $\langle c+a \rangle$ slip systems compared to the other slip systems but stated that the initial shear stress strongly depends on the specific alloy. They are also showing an example, where the τ_0 for $\langle c+a \rangle$ slip systems is about 3 times higher than τ_0 of the basal slip systems. These values are for titanium alloy Ti-6.6Al, but both cp-titanium and the Ti-6.6Al contain the same crystal structure and therefore offer a reference point for the initial shear stress of $\langle c+a \rangle$ slip systems. Finally, to investigate how the additional slip systems

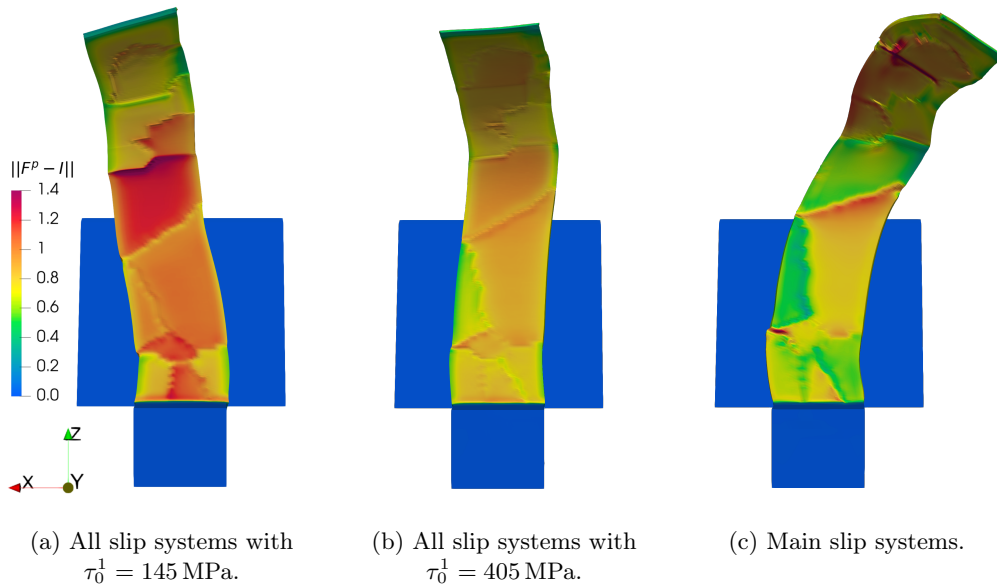
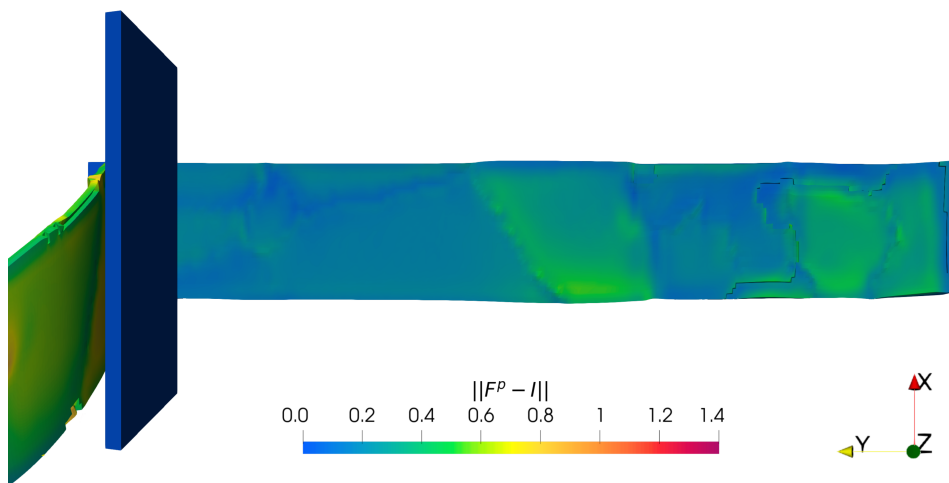


FIGURE 6.33: Comparison of the deformation and the distribution of the plastic deformation for the chip forming of simulations, where the $\langle c+a \rangle$ slip systems are included with different initial shear stress, and the simulation with only the main slip systems.

influence the micro-cutting process, the material is extended by the missing $\langle c+a \rangle$ slip systems. The real structure and the same mesh size of simulation of mesh 1 from the previous section are used for this example. Two simulations are processed with two different values for the initial shear stress of the $\langle c+a \rangle$ slip systems, $\tau_0^1 = 145$ MPa, following Hama et al. (2016), and $\tau_0^2 = 405$ MPa, which is approximately 3 times higher than the value for the basal slip system, following Lütjering and Williams (2013). Comparing the results, as shown in Figure 6.33, where the chip can be seen from the front view and the contour shows the distribution of the plastic deformation, it can be clearly seen that the additional $\langle c+a \rangle$ slip systems have a strong influence. Both the deformation and the intensity of the plastic deformation are different for the three simulations. For the simulation with $\langle c+a \rangle$ slip systems and an initial shear stress of τ_0^1 , the chip is bent to the left. In the first section of the chip, the plastic deformation is lower, while it is significantly higher in the remaining section. If the initial shear stress is increased to τ_0^2 , one can see that the chip is

(a) Main and $\langle c+a \rangle$ slip systems with $\tau_0^1 = 145$ MPa.(b) Main and $\langle c+a \rangle$ slip systems with $\tau_0^1 = 405$ MPa.

(c) Mesh 1 with main slip systems.

FIGURE 6.34: Comparison of the deformation and the distribution of the plastic deformation of the resulting surface of simulations, where the $\langle c+a \rangle$ slip systems are included with different initial shear stress, and the simulation with only the main slip systems.

approximately straight and that there is a moderate plastic deformation throughout. This is compared to the simulation of mesh 1 with the main slip systems from the previous section. Here the chip bends to the right, and sections with high and low plasticity are clearly visible, as already mentioned in the previous section. It is also to mention that the additional slip systems with low initial shear stress favor plastic deformation of certain crystal orientations. This is clearly visible in the middle part of the chip for one grain. With the higher stress, the plastic deformation decreases. If the $\langle c + a \rangle$ slip systems are missing completely, the plastic deformation in this region decreases even more. The observed differences also become visible when looking at the resulting surfaces, see Figure 6.34. But in the opposite direction. There are regions with lower plastic deformation for the simulation with additional slip systems and the low initial shear stress τ_0^1 , the same region shows more plastic deformation for the higher initial shear stress τ_0^2 and shows the highest plastic deformation for the simulation with only the main slip systems. Overall, it can be stated that with the additional $\langle c + a \rangle$ slip systems, and the here used values for the initial shear stress τ_0^1 and τ_0^2 , the plastic deformation on the resulting surface decreases compared to the simulation without these slip systems. If one compares the courses of these three

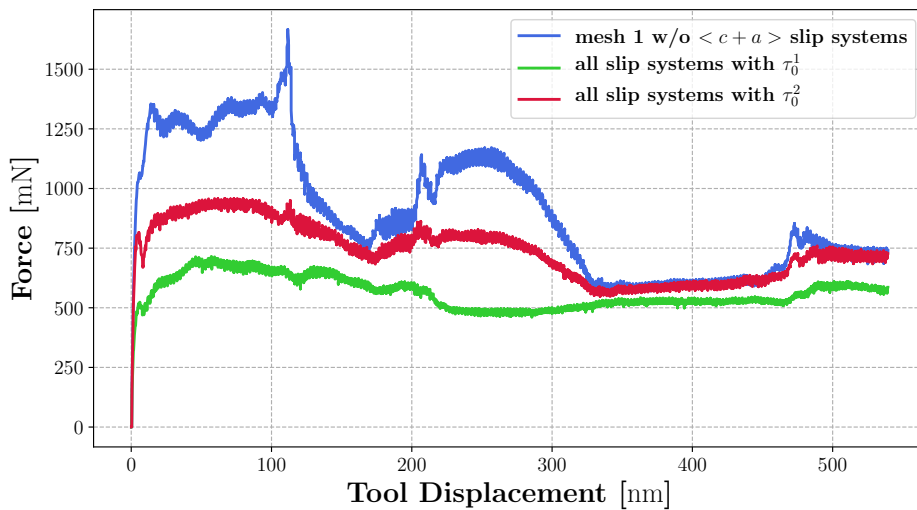


FIGURE 6.35: Comparison of the cutting force between the simulation with the additional $\langle c + a \rangle$ slip systems and the initial shear stress τ_0^1 , the simulation with the additional $\langle c + a \rangle$ slip systems and the initial shear stress τ_0^2 and the simulation of mesh 1 of the previous section without the additional slip systems.

simulations, see Figure 6.35, the following can be observed. For the simulation with all slip systems and the initial shear stress τ_0^1 , a relatively flat curve, in comparison with the simulation using only the main slip systems, results. Significant points, such as peaks, are lost. A higher cutting force in the first part of the simulation is followed by a lower, approximately constant cutting force in the second part. The cutting force for the simulation with all slip systems and the initial shear stress τ_0^2 is already higher in the whole simulation than for the simulation with all slip systems and the initial shear stress τ_0^1 , and so gets closer to the simulation using only the main slip systems. Peaks can be seen in the same places, although they are much less pronounced. It is noticeable that a tool displacement in the range from about 330 μm to 550 μm shows a very similar curve of the cutting force to the cutting force of the simulation, which only

considers the main slip systems. Only the transition in the region of $470\ \mu\text{m}$ shows a lower cutting force, but a similar qualitatively course. It can be summarized that the additional $\langle c + a \rangle$ slip systems certainly have an influence on the deformation and cutting force during the micro-cutting process. It is, therefore, an important task in the preliminary investigation to determine whether these slip systems are active in the specific material and to determine their initial shear stress with high accuracy.

Chapter 7

Conclusion and Outlook

The aim of this work is to gain a better understanding of the elastic and plastic deformation phenomena that occur on the microscale during the micro-cutting process of cp-titanium. To achieve this goal, an elastic-plastic material model, which includes the crystal-plastic slip systems of cp-titanium, has been developed and implemented in this work using the Finite Element Method.

The basis of the finite strain crystal plastic material model is the multiplicative split of the deformation gradient into elastic and plastic part. Additionally, the material model includes an extension to prevent volumetric locking. This so-called F-Bar method proves to be effective and at the same time is easy to implement. In order to decide whether the deformation is elastic or plastic, a yield function is introduced. A neo-Hooke material model is used to calculate the hyperelastic stress. In the plastic case, a plastic corrector is calculated using the return mapping algorithm. Titanium is the material under investigation and has a hexagonal close-packed crystal lattice. Therefore, the material model consists of the slip systems of the hcp unit cell. In this work, a distinction is made between the main slip systems, which are the three basal, three prismatic and six pyramidal slip systems, and the six $\langle c + a \rangle$ slip systems. For the phenomena of hardening, three different hardening mechanisms are introduced. Finally, two different approaches for the mesh separation, which allows the separation and forming of the chip within the micro-cutting process, are presented.

A crucial part of the return mapping algorithm is the determination of the active slip systems. Two different determination algorithms are presented. The first approach is the determination by means of the yield function, which is largely used in the standard literature. The second approach is the determination by means of the Fischer-Burmeister function, proposed by Fischer (1992). These two algorithms are compared in terms of stability and efficiency. It turns out that the standard algorithm based on the yield function leads to unstable states, and no unique set of active slip systems is found. In contrast, the Fischer-Burmeister algorithm is very robust, but requires higher computational capacities, since the system of equations from which the plastic increments are calculated always includes all slip systems. The active slip systems are determined implicitly.

In principle, the crystal plastic material model is validated using a simple example. Furthermore, simple examples are used to show that different hardening mechanisms yield different material behavior. Also, the functionality of the two mesh separation approaches is demonstrated by a simple example. It is shown that the approach based on damage mechanics is not suitable. All micro-cutting simulations are performed with the approach based on geometric criteria.

In the last part of this work, the micro-cutting process is investigated. At first, the general difficulties in performing the simulation of the process are shown. It turns out that the simulation is basically possible, but especially the initial contact between tool and workpiece is a very crucial part of the simulation regarding stability. Furthermore, it is shown that symmetrical crystal orientation leads to instability and, thus, to the termination of the simulation. This can be prevented by additional elements at the beginning of the workpiece, which help to allow the chip to slide over the tool. In further steps, various influences on the micro-cutting process are investigated using model examples. By varying the crystal orientation, it can be seen that the crystal orientation has a strong influence on the plastic deformation of the chip and the resulting workpiece surface and the cutting force. It can also be seen that depending on the crystal orientation from one grain to the next, material piling up or changes in thickness can occur, both in the chip and the resulting surface.

Other process parameters that have been varied are the cutting depth and the rake angle. One workpiece with two different crystal orientations is used in each case. Increasing the cutting depth increases the plastic deformation of the chip and the resulting surface. In addition, the cutting force increases with higher cutting depth, and the influence of the grain boundary on the cutting force increases. With a higher rake angle, the plastic deformation of the chip decreases. On the resulting surface, however, this qualitative evolution can barely be observed. With an increasing rake angle, the cutting force also decreases, but there is no influence of the grain boundary visible. These basic observations can also be seen in macroscopic cutting processes.

Finally, the influence of the hardening mechanism on the simulation has been investigated in this part. For the simple tensile test, few differences in the distribution of the plastic deformation and the force-displacement diagram between the isotropic linear hardening and the latent linear hardening are observed. Only the computation time significantly increases when using the linear latent hardening. However, the differences between isotropic linear hardening and latent linear hardening are more evident for the micro-cutting simulation. Both the forming and the distribution of the plastic deformation of the chip differ clearly. This difference is also visible by observing the cutting force. Nevertheless, approximately the same cutting force can be found in the first grain region, whereas it differs sharply in the second grain region. For the simulation with the latent linear hardening, a much higher cutting force can be seen. Furthermore, it can be concluded that both the linear latent hardening and the latent Voce hardening are not suitable for the use in micro-cutting simulations, because the computation time increases very much, and the simulation cannot be performed in a reasonable time.

In the last part, the micro-cutting process of a real workpiece sample is investigated. For this purpose, the FEM mesh and the crystal orientation are created using a real sample. The simulation is performed with two meshes, a coarser and a finer one, to additionally investigate the influence of the element size of the mesh. Depending on the crystal orientation, sections with higher and lower plastic deformation are formed on the chip surface and the resulting workpiece surface. Furthermore, the grain boundaries are usually clearly visible, often due to material accumulation and a gap in the amount of plastic deformation. The chip bends to the side during the simulation, depending on the crystal orientation. The deformation and the distribution of the plastic deformation are qualitatively very similar for the chip and the resulting surface for both FEM meshes. Also, the graphs of the cutting force are qualitatively very well

agreeing. The final investigation regarding the influence of the additional $\langle c + a \rangle$ slip systems is also performed on the FEM mesh of the real sample. Various aspects of the impact of these slip systems are described in the literature. An important observation is, that these slip systems have an influence on the deformation and the cutting force of the process.

For further work, an experimental validation would be very interesting to adapt to the material model since the different slip systems have a strong influence on material behavior. It should be experimentally determined whether slip occurs on the additional slip systems, and a determination of the material parameters should be carried out as accurately as possible. For this purpose, further investigations using atomistic simulation or dislocation dynamics could be helpful. It has been shown in the work that the introduced latent hardening mechanisms lead to very small time steps and strongly increasing simulation time. Therefore, the discussed hardening mechanisms are unsuitable for the micro-cutting process. Hardening should be further investigated, and attention should be paid to the implementation. Friction and heat generation should be considered as they play an important role in the process.

Bibliography

- Acary, V., Brémond, M., and Huber, O. (2018). “On Solving Contact Problems with Coulomb Friction: Formulations and Numerical Comparisons”. In: *Advanced Topics in Nonsmooth Dynamics: Transactions of the European Network for Nonsmooth Dynamics*. Ed. by R. Leine, V. Acary, and O. Brüls. Cham: Springer International Publishing, pp. 375–457.
- Akpama, H. K., Bettaieb, M. B., and Abed-Meraim, F. (2016). “Numerical integration of rate-independent BCC single crystal plasticity models: comparative study of two classes of numerical algorithms”. In: *International Journal for Numerical Methods in Engineering* 108.5, pp. 363–422.
- Asaro, R. and Needleman, A. (1985). “Overview no. 42 Texture development and strain hardening in rate dependent polycrystals”. In: *Acta Metallurgica* 33.6, pp. 923 – 953.
- Asaro, R. J. (1983). “Micromechanics of Crystals and Polycrystals”. In: ed. by J. W. Hutchinson and T. Y. Wu. Vol. 23. *Advances in Applied Mechanics*. Elsevier, pp. 1 –115.
- Bartel, T., Schulte, R., Menzel, A., Kiefer, B., and Svendsen, B. (2019). “Investigations on enhanced Fischer–Burmeister NCP functions : application to a rate-dependent model for ferroelectrics”. In: *Archive of Applied Mechanics* 89.6, pp. 995–1010.
- Bassani, J. L. and Wu, T.-y. (1991). “Latent hardening in single crystals. II. Analytical characterization and predictions”. In: *Proceedings of the Royal Society of London. Series A: Mathematical and Physical Sciences* 435.1893, pp. 21–41.
- Bischof, R., Böhme, L., Kuhn, C., Müller, R., and Kerscher, E. (2018). “Deformation behaviour of small scale cp-titanium specimen with large grains”. In: *PAMM* 18.1, e201800360.
- Bischof, R., Schneider, F., Müller, C., Kuhn, C., Aurich, J., and Müller, R. (2017). “Robust implementation of multi-slip crystal plasticity for micro machining simulations based on Fischer-Burmeister complementary functions”. In: *PAMM* 17, pp. 407–408.
- Borja, R. (2013). *Plasticity: Modeling & Computation*. Springer Berlin Heidelberg.
- Borja, R. I. and Wren, J. R. (1993). “Discrete micromechanics of elastoplastic crystals”. In: *International Journal for Numerical Methods in Engineering* 36.22, pp. 3815–3840.
- Braess, D. (2007). *Finite Elements - Theory, Fast Solvers, and Applications in Solid Mechanics*. Cambridge: Cambridge University Press.

- Brown, S. B., Kim, K. H., and Anand, L. (1989). "An internal variable constitutive model for hot working of metals". In: *International Journal of Plasticity* 5.2, pp. 95–130.
- Böge, A. and Böge, W. (2015). *Formeln und Tabellen Maschinenbau - Für Studium und Praxis*. Berlin Heidelberg New York: Springer-Verlag.
- Cuitiño, A. and Ortiz, M. (1993). "Computational modeling of single crystals". In: *Modelling and Simulation in Materials Science and Engineering* 1, pp. 225–263.
- De Coninck, A., De Baets, B., Kourounis, D., Verbosio, F., Schenk, O., Maenhout, S., and Fostier, J. (2016). "Needles: Toward Large-Scale Genomic Prediction with Marker-by-Environment Interaction". In: *Genetics* 203.1, pp. 543–555.
- de Geus, T., Maresca, F., Peerlings, R., and Geers, M. (2016). "Microscopic plasticity and damage in two-phase steels: On the competing role of crystallography and phase contrast". In: *Mechanics of Materials* 101, pp. 147–159.
- de Souza Neto, E. A., Perić, D., Dutko, M., and Owen, D. (1996). "Design of simple low order finite elements for large strain analysis of nearly incompressible solids". In: *International Journal of Solids and Structures* 33.20, pp. 3277–3296.
- de Souza Neto, E. A., Perić, D., and Owen, D. R. J. (2011). *Computational Methods for Plasticity - Theory and Applications*. New York: John Wiley & Sons.
- Denkena, B. and Toenshoff, H. K. (2011). *Spanen - Grundlagen*. Berlin Heidelberg New York: Springer-Verlag.
- Fischer, A. (1992). "A special newton-type optimization method". In: *Optimization* 24.3-4, pp. 269–284.
- Godard, C. (2015). "Auswirkungen von Mikrokerben auf das quasistatische und zyklische Verformungsverhalten von cp-Titan-Mikroproben". Dissertation. Technische Universität Kaiserslautern.
- Gross, D., Hauger, W., and Wriggers, P. (2011). *Technische Mechanik 4 - Hydromechanik, Elemente der Höheren Mechanik, Numerische Methoden*. Berlin Heidelberg New York: Springer-Verlag.
- Gurtin, M. (1982). *An Introduction to Continuum Mechanics*. Academic Press New York.
- Hama, T., Kobuki, A., Fujimoto, H., and Takuda, H. (2016). "Crystal-plasticity finite-element analysis of deformation behavior in a commercially pure titanium sheet". In: *Journal of Physics: Conference Series* 734, p. 032071.
- Havner, K. S. (1992). *Finite Plastic Deformation of Crystalline Solids*. Cambridge Monographs on Mechanics. Cambridge University Press.
- Holzappel, G. A. (2000). *Nonlinear Solid Mechanics - A Continuum Approach for Engineering*. New York: Wiley.

- Hughes, T. J. R. (1980). “Generalization of selective integration procedures to anisotropic and nonlinear media”. In: *International Journal for Numerical Methods in Engineering* 15.9, pp. 1413–1418.
- Intel[®] Corporation (Aug. 2020). *Intel[®] MKL PARDISO - Parallel Direct Sparse Solver Interface*. URL: <https://software.intel.com/content/www/us/en/develop/documentation/mkl-developer-reference-fortran/top/sparse-solver-routines/intel-mkl-pardiso-parallel-direct-sparse-solver-interface.html>.
- Johnson, G. R. and Cook, W. H. (1985). “Fracture characteristics of three metals subjected to various strains, strain rates, temperatures and pressures”. In: *Engineering Fracture Mechanics* 21.1, pp. 31–48.
- Komvopoulos, K. and Erpenbeck, S. A. (1991). “Finite Element Modeling of Orthogonal Metal Cutting”. In: *Journal of Engineering for Industry* 113.3, pp. 253–267.
- Kourounis, D., Fuchs, A., and Schenk, O. (2018). “Towards the Next Generation of Multiperiod Optimal Power Flow Solvers”. In: *IEEE Transactions on Power Systems* PP.99, pp. 1–10.
- Laursen, T. A. (2013). *Computational Contact and Impact Mechanics - Fundamentals of Modeling Interfacial Phenomena in Nonlinear Finite Element Analysis*. Berlin Heidelberg: Springer Science & Business Media.
- Lee, E. H. (1969). “Elastic-Plastic Deformation at Finite Strains”. In: *Journal of Applied Mechanics* 36.1, pp. 1–6.
- Lee, E. H. and Liu, D. T. (1967). “Finite-Strain Elastic—Plastic Theory with Application to Plane-Wave Analysis”. In: *Journal of Applied Physics* 38.1, pp. 19–27.
- Lemaitre, J. and Desmorat, R. (2006). *Engineering Damage Mechanics - Ductile, Creep, Fatigue and Brittle Failures*. Berlin Heidelberg: Springer Science & Business Media.
- Leyens, C. and Peters, M. (2006). *Titanium and Titanium Alloys - Fundamentals and Applications*. New York: John Wiley & Sons.
- Li, A., Pang, J., Zhao, J., Zang, J., and Wang, F. (2017). “FEM-simulation of machining induced surface plastic deformation and microstructural texture evolution of Ti-6Al-4V alloy”. In: *International Journal of Mechanical Sciences* 123, pp. 214–223.
- Li, K., Gao, X.-L., and Sutherland, J. (2002). “Finite element simulation of the orthogonal metal cutting process for qualitative understanding of the effects of crater wear on the chip formation process”. In: *Journal of Materials Processing Technology* 127.3, pp. 309–324.
- Lubliner, J. (2013). *Plasticity Theory*. Dover Books on Engineering. New York: Dover Publications.

- Lütjering, G. and Williams, J. C. (2013). *Titanium*. Berlin Heidelberg: Springer Science & Business Media.
- Mamalis, A., Horváth, M., Branis, A., and Manolakos, D. (2001). “Finite element simulation of chip formation in orthogonal metal cutting”. In: *Journal of Materials Processing Technology* 110, pp. 19–27.
- Miehe, C. (1996a). “Exponential Map Algorithm for Stress Updates in Anisotropic Multiplicative Elastoplasticity for Single Crystals”. In: *International Journal for Numerical Methods in Engineering* 39.19, pp. 3367–3390.
- Miehe, C. (1996b). “Multisurface thermoplasticity for single crystals at large strains in terms of eulerian vector updates”. In: *International Journal of Solids and Structures* 33.20, pp. 3103–3130.
- OpenMP[®] ARB (2020). *OpenMP[®] Specifications*. URL: <https://www.openmp.org/specifications/>.
- Özel, T. and Zeren, E. (2005). “Finite Element Method Simulation of Machining of AISI 1045 Steel With A Round Edge Cutting Tool”. In: *Proceedings of the Eighth CIRP International Workshop on Modeling of Machining Operations*, pp. 533–542.
- Peirce, D., Asaro, R., and Needleman, A. (1983). “Material rate dependence and localized deformation in crystalline solids”. In: *Acta Metallurgica* 31.12, pp. 1951–1976.
- Sabel, M. (2017). “A Particle Finite Element Method for Cutting of Solids”. Dissertation. Technische Universität Kaiserslautern.
- Shet, C. and Deng, X. (2000). “Finite element analysis of the orthogonal metal cutting process”. In: *Journal of Materials Processing Technology* 105, pp. 95–109.
- Shih, A. J. (1996). “Finite element analysis of orthogonal metal cutting mechanics”. In: *International Journal of Machine Tools and Manufacture* 36.2, pp. 255–273.
- Simo, J. and Hughes, T. J. R. (1998). *Computational Inelasticity*. Interdisciplinary Applied Mathematics. Springer New York.
- Steinmann, P. and Stein, E. (1996). “On the numerical treatment and analysis of finite deformation ductile single crystal plasticity”. In: *Computer Methods in Applied Mechanics and Engineering* 129.3, pp. 235–254.
- Sussman, T. and Bathe, K.-J. (1987). “A finite element formulation for nonlinear incompressible elastic and inelastic analysis”. In: *Computers & Structures* 26.1, pp. 357–409.
- Verbosio, F., Coninck, A. D., Kourounis, D., and Schenk, O. (2017). “Enhancing the scalability of selected inversion factorization algorithms in genomic prediction”. In: *Journal of Computational Science* 22.Supplement C, pp. 99–108.
- Woon, K., Rahman, M., Fang, F., Neo, K., and Liu, K. (2008). “Investigations of tool edge radius effect in micromachining: A FEM simulation approach”. In: *Journal of Materials Processing Technology* 195.1, pp. 204–211.

-
- Wriggers, P. (2006). *Computational Contact Mechanics*. Berlin Heidelberg: Springer Science & Business Media.
- Wriggers, P. (2008). *Nonlinear Finite Element Methods*. Berlin Heidelberg: Springer Science & Business Media.
- Zienkiewicz, O. C. and Taylor, R. L. (2013). *The Finite Element Method for Solid and Structural Mechanics*. Oxford: Butterworth-Heinemann.
- Zienkiewicz, O. C., Taylor, R. L., and Zhu, J. Z. (2005). *The Finite Element Method: Its Basis and Fundamentals*. Amsterdam: Elsevier.
- Zohdi, T. I. and Wriggers, P. (2008). *An Introduction to Computational Micromechanics*. Berlin, Heidelberg: Springer.

Lebenslauf

Name Robert Bischof
Geburtsort Saarbrücken
Nationalität Deutsch

August 1994 - Juli 1998 Grundschule Ommersheim

August 1998 - Juni 2007 Leibniz-Gymnasium Sankt Ingbert
Abschluss: Allgemeine Hochschulreife

Oktober 2007 - Februar 2015 Studium Maschinenbau und Verfahrenstechnik
Technische Universität Kaiserslautern

Diplomarbeit:
*Numerische Untersuchung von Filmkühlung
in einer "Energy Efficient Engine" - Kaskade*

Abschluss: Diplomingenieur Maschinenbau

März 2015 - August 2019 Wissenschaftlicher Mitarbeiter
Lehrstuhl für Technische Mechanik
Fachbereich Maschinenbau und Verfahrenstechnik
Technische Universität Kaiserslautern